


Precise Control of Entanglement in Multinuclear Spin Registers Coupled to Defects

Evangelia Takou^{1,2,*} Edwin Barnes^{1,2,†} and Sophia E. Economou^{1,2,‡}

¹*Department of Physics, Virginia Tech, Blacksburg, Virginia 24061, USA*

²*Virginia Tech Center for Quantum Information Science and Engineering, Blacksburg, Virginia 24061, USA*

 (Received 17 May 2022; revised 12 November 2022; accepted 12 December 2022; published 18 January 2023)

Quantum networks play an indispensable role in quantum information tasks such as secure communications, enhanced quantum sensing, and distributed computing. Among the most mature and promising platforms for quantum networking are nitrogen-vacancy (NV) centers in diamond and other color centers in solids. One of the challenges in using these systems for networking applications is to controllably manipulate entanglement between the electron and the nuclear spin register despite the always-on nature of the hyperfine interactions, which makes this an inherently many-body quantum system. Here, we develop a general formalism to quantify and control the generation of entanglement in an arbitrarily large nuclear spin register coupled to a color center electronic spin. We provide a reliable measure of nuclear spin selectivity, by exactly incorporating into our treatment the dynamics with unwanted nuclei. We also show how to realize direct multipartite gates through the use of dynamical decoupling sequences, drastically reducing the total gate time compared to protocols based on sequential entanglement with individual nuclear spins. We quantify the performance of such gate operations in the presence of unwanted residual entanglement links, capturing the dynamics of the entire nuclear spin register. Finally, using experimental parameters of a well-characterized 27 nuclear spin register device, we show how to prepare with high-fidelity entangled states for quantum error correction. While in this analysis we focus on a particular NV-diamond-based register, our framework is completely general and applicable to other defects in diamond and in SiC.

DOI: [10.1103/PhysRevX.13.011004](https://doi.org/10.1103/PhysRevX.13.011004)

Subject Areas: Quantum Physics, Quantum Information

I. INTRODUCTION

Controlling on-demand quantum nodes with high precision and scaling up to build large-scale quantum architectures is the ultimate goal of quantum information processing. Quantum networks are clusters of nodes interconnected via communication channels, which transfer information or distribute entanglement using photons [1]. Long-distance connections are established by breaking the transmission distance into smaller segments and creating intermediate entanglement links through quantum repeaters [2]. Quantum networks enable secure communication [3–6] between qubit devices and enhance quantum computing and sensing capabilities [7–9] by using entanglement as a resource. Spin registers in solid-state systems

comprise a leading platform for repeater implementation. Such registers are already realized using nitrogen-vacancy (NV) centers in diamond [10–12], with a recent milestone experiment [11] demonstrating a few-node network, SiV centers in diamond [13,14], and quantum dots [15]. Proposals for hybrid architectures complemented by transducers [16] or modular designs [17,18] have also been put forward. In defect platforms, the electronic spin serves as the communication qubit, because it features a spin-photon interface, while nearby nuclear spins can serve as long-lived quantum memories.

A challenge with exploiting the long coherence times of the nuclear spins is twofold: (i) The interactions between the nuclear spins and the electronic defect are always on (not switchable), and (ii) the majority of the nuclear spins are located at distant lattice sites, which leads to interactions that are weak compared to the dephasing rate of the defect spin. Fortunately, both these issues can be addressed simultaneously through the use of dynamical decoupling (DD) pulse sequences [19]. The parameters associated with these DD sequences (specifically, the interpulse spacing) are selected such that, ideally, all nuclear spins except for one are decoupled from the defect. This effectively creates a knob to select a target nuclear spin. By varying the

*etakou@vt.edu

†efbarnes@vt.edu

‡economou@vt.edu

Published by the American Physical Society under the terms of the Creative Commons Attribution 4.0 International license. Further distribution of this work must maintain attribution to the author(s) and the published article's title, journal citation, and DOI.

pulse spacing, different nuclear spins can be selected across the register. This approach has led to bold first steps toward distributing entanglement across a network of a few quantum nodes [11,20], realizing error-correction schemes [21–23], performing entanglement distillation [12], or implementing quantum repeater protocols [24].

Despite these seminal experimental demonstrations, critical challenges remain in exploiting nuclear spins as quantum memory registers for networks. A key issue is that, due to the many-body nature of this always-coupled system, the electron is never fully decoupled from the remaining nuclear spins, leading to residual electron-nuclear entanglement. This lowers the fidelity of the gates and can be detrimental in the operation of the network. An additional consideration is that, in these DD control protocols, the gates between the defect and each nuclear spin are implemented sequentially, which can lead to impractically long operations in the encoding and decoding steps of quantum error correction. While these issues can be, in part, addressed by adding controls to the system, e.g., by directly driving the nuclear spins through nuclear magnetic resonance [25], this complicates the experiment significantly, leading to a potentially impractical overhead that could limit scalability.

In this paper, we address these challenges by developing a formalism that allows us to capture the dynamics of the full system. This, in turn, enables us to both characterize the quality of the electron-nuclear gates and to design DD sequences that can directly create multipartite entangling gates within the defect-nuclear spin register. A key insight in our approach is that the form of the Hamiltonian allows an exact analysis of the whole system in terms of only bipartite dynamics. We use the notion of one-tangles, an entanglement measure that captures quantum correlations between a single spin and a spin ensemble. We present closed-form expressions for the one-tangles of individual nuclear spins in the register and of the defect electronic spin. Remarkably, these one-tangles depend only on two-qubit Makhlin invariants (parameters that quantify and classify the entangling power of two-qubit gates). This critical simplification allows us to systematically determine the DD sequences that maximize or minimize the one-tangles as desired for nuclear spin registers containing up to hundreds of nuclei. We use this approach to find sequences that create entanglement between the electron and a target subset of nuclei while simultaneously decoupling unwanted nuclei. We show that it is possible to perform controlled entangling operations involving three nuclear spins more than 4 times faster than sequential gate approaches while achieving significantly higher gate fidelities, which capture errors due to the presence of the entire nuclear register. We further reformulate the three-qubit bit-flip code in terms of the multispin gates and, using parameters from the well-characterized 27-qubit device by the Delft group, we show that the electron’s state can be retrieved with probability $> 99\%$. Our approach

provides a practical and scalable means for selecting nuclear spins as quantum memory qubits and for designing gates among them that can prepare entangled multipartite states for efficient encoding and decoding steps in quantum error correction protocols.

The paper is organized as follows. In Sec. II, we review and generalize existing results on π -pulse sequences used for controlling single nuclear spins. In Sec. III, we quantify entanglement in the case of a single nuclear spin coupled to the electron, and we present our formalism for the entanglement distribution in the entire nuclear spin register. Finally, in Sec. IV, we show how to perform multispin gates, quantify their gate fidelity in the presence of spectator nuclei, and show how to use these gates for quantum error correction codes.

II. CONTROLLING A SINGLE NUCLEAR SPIN

In this section, we describe how a single nuclear spin coupled to a single defect spin can be controlled via DD sequences applied to the latter. The application of periodic trains of pulses on the electron interleaved by free-evolution periods can either generate single-qubit gates on a nuclear spin or entangle it with the electronic spin. This is because dynamical decoupling sequences can modify the effective electron-nuclear hyperfine interaction, allowing one to couple a specific nucleus to the electron while decoupling others. Well-known examples of dynamical decoupling sequences that have been under investigation for many decades include the Carr-Purcell-Meiboom-Gill (CPMG) [26–29] and Uhrig (UDD) [30,31] sequences. In this section, we review and generalize existing results for single nuclear spin control via electronic spin driving. In subsequent sections, we treat the problem of controlling multiple nuclear spins at the same time.

A. Creating electron-nuclear spin entanglement

We begin with the task of creating electron-nuclear spin entanglement. It is shown in Ref. [19] that, by choosing the pulse spacing to satisfy a certain resonance condition that depends on the hyperfine couplings, it is possible to rotate a target nuclear spin in a way that depends on the electronic spin state. This is done using pulse sequences that are obtained by concatenating a basic “unit” multiple times. For example, the CPMG sequence can be expressed in terms of N units as $(t/4 - \pi - t/2 - \pi - t/4)^N$, where t is the duration of the unit and π represents a π pulse. The pulses are implemented experimentally via a microwave (MW) drive to directly induce transitions between electronic spin states. The idealized instantaneous π pulses, in reality, have finite amplitude and duration; they could be generated using a vector source [32], whose characteristics (e.g., frequency, duration, and amplitude) are predefined by an arbitrary waveform generator, and their shapes could, for example, be Hermite envelopes [25,33].

The Hamiltonian for a single nuclear spin ($I = 1/2$) is given by [34]

$$\begin{aligned} H &= \frac{\omega_L}{2} \mathbb{1} \otimes \sigma_z + \frac{A}{2} Z_e \otimes \sigma_z + \frac{B}{2} Z_e \otimes \sigma_x \\ &= \sigma_{00} \otimes H_0 + \sigma_{11} \otimes H_1, \end{aligned} \quad (1)$$

where σ_j are the Pauli matrices, ω_L is the Larmor frequency of the nuclear spin, and A and B are the parallel and perpendicular components of the hyperfine interaction, respectively. The electron spin operator Z_e is defined as $Z_e = s_0|0\rangle\langle 0| + s_1|1\rangle\langle 1|$, where $|0\rangle$ and $|1\rangle$ are the two levels of the electron spin multiplet used to define the qubit and s_j are the corresponding spin projection quantum numbers. Furthermore, we define H_j as $H_j = 1/2[(\omega_L + s_j A)\sigma_z + s_j B\sigma_x]$. From the above Hamiltonian, it follows that the electron-nuclear spin evolution operator after one unit of the pulse sequence is given by

$$U = \sigma_{00} \otimes R_{\mathbf{n}_0}(\phi_0) + \sigma_{11} \otimes R_{\mathbf{n}_1}(\phi_1), \quad (2)$$

where $\sigma_{jj} \equiv |j\rangle\langle j|$ are projectors onto two of the levels in the electron spin multiplet and $R_{\mathbf{n}_j}(\phi_j) = e^{-i\phi_j/2(\sigma \cdot \mathbf{n}_j)}$ denotes two different conditional nuclear spin evolution operators specified by rotation axes \mathbf{n}_j and angles ϕ_j . Both \mathbf{n}_j and ϕ_j , in general, depend on the electron's spin state and on the pulse sequence. The explicit form of $R_{\mathbf{n}_j}(\phi_j)$ in the case of CPMG is found in Appendix A 1.

To create entanglement, we need the two rotation operators $R_{\mathbf{n}_j}(\phi_j)$ to differ. It is, in fact, possible to choose the pulse time t such that the nuclear spin axes are antiparallel, i.e., $\mathbf{n}_0 \cdot \mathbf{n}_1 = -1$. At the same time, the coherence function P_x , which is the probability for an electron prepared in state $|+\rangle$ to return to this state at time t , reaches a minimum. The coherence function can be expressed as $P_x = 1/2(1 + M)$, where $M = \frac{1}{2}\text{ReTr}[R_{\mathbf{n}_0}(\phi_0)R_{\mathbf{n}_1}^\dagger(\phi_1)]$ (see also Ref. [19] and Appendix B). As shown in Ref. [19], for $\phi_0 = \phi_1 \equiv \phi$ (which holds for CPMG), M is given by $M = 1 - \sin^2(\phi/2)(1 - \mathbf{n}_0 \cdot \mathbf{n}_1)$. By calculating M analytically using the explicit expressions for the conditional evolution operators $R_{\mathbf{n}_j}(\phi_j)$ and by setting $\mathbf{n}_0 \cdot \mathbf{n}_1 = -1$, the resonance times can be obtained. For the CPMG, UDD₃, and UDD₄ sequences, we find that these resonances occur at times

$$t_k = \frac{4\pi(2k-1)}{\tilde{\omega}}, \quad (3)$$

where $\tilde{\omega} = \omega_0 + \omega_1$, $\omega_j = \sqrt{(\omega_L + s_j A)^2 + (s_j B)^2}$, and $k \in \mathbb{Z}^+$ is the order of the resonance. This expression for t_k , which is valid for $\omega_L \gg A, B$, combines and generalizes known results. For example, the resonance times of Eq. (3)

are shown in Refs. [19,35] for $s_0 = 0$ and $s_1 = -1$, while in Ref. [13] for $s_0 = -s_1 = 1/2$. For the UDD₄ sequence, whose basic unit is $q_1 t - \pi - q_2 t - \pi - q_3 t - \pi - q_4 t - \pi - q_5 t$ (see Appendix C for definitions of q_s), we find that there are additional resonances at times $t_k = 8\pi(2k-1)/\tilde{\omega}$, which is also reported in Ref. [35]. All resonance times are valid for any electronic spin projection and any type of nuclear spin with $I = 1/2$ (e.g., ¹³C in diamond or SiC or ²⁹Si in SiC).

An electron-nuclear spin entangling gate is achieved by iterating the sequence an appropriate number N to accumulate a desired rotation angle on the nuclear spin. We present the rotation angles for the three pulse sequences in Appendix C. Sequences with an odd number of pulses in the basic unit need to be repeated twice to ensure the electron returns to its initial state. For CPMG and UDD₃ (the latter has the unit $q_1 t - \pi - q_2 t - \pi - q_3 t - \pi - q_4 t$ that we repeat twice; see also Appendix C), we find that the rotation angles per iteration are equal, i.e., $\phi_0 = \phi_1$. One way to generate an entangling gate is to set the unit time equal to a resonance time and repeat the sequence such that it leads to a total angle of $\pi/2$ and, hence, implements a $\text{CR}_x(\pi/2)$ gate [19,21]. This is possible since the evolution operator after N repetitions of the basic unit retains the form of Eq. (2) with ϕ_j replaced by the total rotation angle $\phi_j(N)$, whereas the dot product $\mathbf{n}_0 \cdot \mathbf{n}_1$ is independent of N at resonance. However, this latter feature does not hold for any sequence. In principle, one can realize entangling operations beyond $\text{CR}_x(\pi/2)$, which we explore later on in Sec. IV.

The UDD₄ sequence yields a more complicated evolution of the nuclear spin, since it rotates by a different amount, depending on the electron's state (i.e., $\phi_0 \neq \phi_1$). This condition leads to a nontrivial feature based on which the dot product of its rotation axes depends on N . Thus, even if one fixes a resonance time for the basic UDD₄ unit, the nuclear rotation axes can switch from antiparallel to parallel for some N . This feature is shown in Figs. 1(c) and 1(d) near the resonance time $t_k = 4\pi(2k-1)/\tilde{\omega}$ and $t_k = 8\pi(2k-1)/\tilde{\omega}$, respectively, for the first four UDD₄ resonances. In Appendix D, we show that $\mathbf{n}_0 \cdot \mathbf{n}_1 = 1$ at values of N where the rotation angles ϕ_0 and ϕ_1 become equal; since the axes are parallel in these ranges, the nuclear spin undergoes an unconditional rotation, and no entanglement is generated.

The jumps in $\mathbf{n}_0 \cdot \mathbf{n}_1$ in the case of UDD₄ appear because we restrict the value of the rotation angles in $[0, \pi]$; if the angles are in $[-\pi, 0]$, we make them positive and reverse the corresponding signs of the rotation axes \mathbf{n}_j for consistency. Alternatively, if the rotation angles are not restricted in this way, the dot product remains fixed at $\mathbf{n}_0 \cdot \mathbf{n}_1 = -1$ for all N . However, for some N , it could happen that $\phi_0 = -\phi_1$ (modulo 2π), which means that such N cannot produce an entangling gate. It would then be misleading to claim there is a resonance whenever

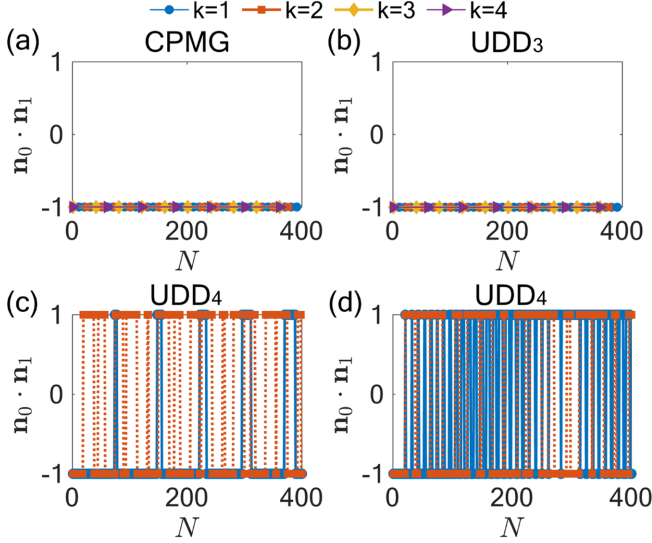


FIG. 1. Dot product of nuclear spin rotation axes for (a) CPMG, (b) UDD₃, and (c),(d) UDD₄ versus the number of iterations N of the basic pulse sequence unit at the first four ($k \in [1, 4]$) resonances of a target spin $[(A, B, \omega_L) = 2\pi \cdot (80, 25, 314)$ kHz] for an electronic spin with $S = 1/2$. For CPMG and UDD₃, $\mathbf{n}_0 \cdot \mathbf{n}_1$ is independent of N , since the rotation angles ϕ_0 and ϕ_1 per iteration are equal. For UDD₄, the dot product jumps between -1 and $+1$ due to the different rotation angles ϕ_j . In the ranges where $\mathbf{n}_0 \cdot \mathbf{n}_1 = 1$, it holds that $\phi_0 \approx \phi_1$, and the rotation of the nuclear spin is unconditional on the electron. In (c) we consider the resonance time $4\pi(2k-1)/\tilde{\omega}$ and in (d) the time $8\pi(2k-1)/\tilde{\omega}$. The times for (a) are $t_k = (3.1822, 9.5465, 15.9108, 22.2751)$ μs (b) $t_k = (3.1850, 9.5537, 15.9124, 22.2805)$ μs , (c) $t_k = (3.1857, 9.5481, 15.9169, 22.2737)$ μs , and (d) $t_k = (6.3661, 19.0883, 31.8190, 44.5509)$ μs . For the UDD sequences, we optimize the time around the resonance.

$\mathbf{n}_0 \cdot \mathbf{n}_1 = -1$ for UDD₄. Thus, we fix the convention $\phi_j \in [0, \pi]$ to ensure that we find the right N to produce conditional rotations on the nuclear spins. This convention is not necessary for CPMG and UDD₃, as it always holds that $\phi_0 = \phi_1$, and we can reliably identify N to create entangling gates. No matter which convention is used for the rotation angles of CPMG or UDD₃, the dot product shows no dependence on N [Figs. 1(a) and 1(b)].

It is important to note that, in addition to implementing gates, π -pulse sequences can also average out the interactions of the electron with unwanted spins, ensuring some degree of selectivity with a target spin. Higher-order resonances are proven to be more effective in targeting a desired nuclear spin [35,36]. In turn, this implies that long sequences are required to achieve enhanced selectivity. In some cases, the sequences average out even the interaction with a target nucleus, rendering such spins uncontrollable or introducing the need for more sophisticated approaches, such as decoherence protected subspaces [37] (which also require direct driving of nuclear registers). These issues are also discussed further later on when we talk about simultaneous control of multiple nuclei.

B. Implementing single-qubit gates on a nuclear spin

We can use similar ideas to determine how to implement single-qubit gates on a nuclear spin without entangling it with the electron. Let us illustrate this in the case of CPMG. The CPMG sequence yields a rather simple equation for the rotation axes dot product of a single nuclear spin, which reads

$$1 - \mathbf{n}_0 \cdot \mathbf{n}_1 = \frac{4 \sin^2(\theta_0 - \theta_1) \sin^2(\omega_0 t/8) \sin^2(\omega_1 t/8)}{\sin^2(\phi/2)}, \quad (4)$$

where $\cos \theta_j = (\omega_L + s_j A)/\omega_j$. This expression is exact for $s_j B \ll \omega_j$ or fairly in the limit $\cos \theta_j \rightarrow 1$. Equation (4) is a generalization of the inner product of Ref. [19], with the difference that it is presented there for an electron spin $S = 1$ (with the choice $s_0 = 0$ and $s_1 = -1$). The nuclear spin evolves independently of the electron when $\mathbf{n}_0 \cdot \mathbf{n}_1 = 1$ and $\phi_0 = \phi_1$. For the CPMG sequence, it always holds that $\phi_0 = \phi_1$. Thus, using Eq. (4) and by requiring that $\mathbf{n}_0 \cdot \mathbf{n}_1 = 1$, we find two conditions for the decoupled evolution:

$$\left(A + \frac{\omega_L}{s_j}\right)^2 + B^2 = \left(\frac{8\kappa\pi}{s_j t}\right)^2, \quad (5)$$

which are the equations of a circle with center $C = (-\omega_L/s_j, 0)$ and radius $R = 8\kappa\pi/s_j t$ [with $\kappa \in \mathbb{Z}$ and t being the time of one CPMG unit]. Note that for a $S = 1$ defect electron spin, and if $s_j = 0$, the decoupled evolution happens at times $t = 8\kappa\pi/\omega_L$ for all nuclei. Using Eq. (5), one can identify nuclei that do not affect the gate fidelity of target nuclear spins, as the former show no correlations with the electron. Notice that these conditions are independent of the number of repetitions of the sequence, as the dot product itself does not depend on N . In addition, since the evolution operator of the system is defined by the rotation each spin undergoes, this feature continues to hold in the total system. We use the condition for decoupled evolution in Sec. IV B to show that such spins have no effect on the gate operations with target nuclei. For now, we stress that Eq. (5) is valid for $(8\kappa\pi/s_j t)^2 > (A + \omega_L/s_j)^2$, while we also constrain the κ/t range such that $A, B \leq 2\pi \cdot 300$ kHz, i.e., such that the nuclei are weakly coupled with the electron. Some examples for an electron-spin $S = 1/2$ ($s_0 = -s_1 = 1/2$) and $S = 3/2$ ($s_0 = 3/2, s_1 = -1/2$) are shown in Figs. 2(a) and 2(b), respectively. One notices that the times t of the basic sequence exceed a few microseconds. In turn, this implies that the condition of the trivial evolution is strictly satisfied for $k \geq 2$ CPMG resonances of the spins with hyperfine (HF) parameters shown in Fig. 2. In Appendix E, we further show that trivial evolution can occur for shorter times of the basic unit, although the triviality is only approximate in this case.

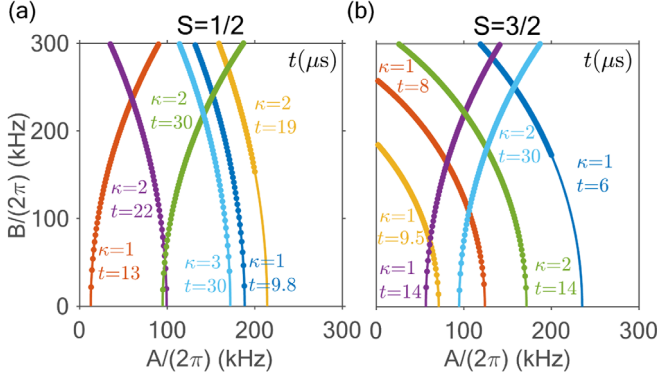


FIG. 2. Hyperfine parameters of nuclear spins that undergo a trivial evolution under the CPMG sequence. Each circle corresponds to a constant time of one CPMG unit and different value of κ [see the main text]. In (a), we select the electron's spin projections $s_0 = -s_1 = 1/2$ and in (b) $s_0 = 3/2$ and $s_1 = -1/2$. The Larmor frequency is considered to be $\omega_L = 2\pi \cdot 314$ kHz. For illustration purposes, we show mainly times $t \in \mathbb{Z}^+$, but t could also take any positive noninteger values.

III. QUANTIFYING ENTANGLEMENT IN THE ELECTRON-NUCLEAR SPIN SYSTEM

Controlling multiple nuclear spins is usually done by applying additional radio-frequency pulses that drive the nuclear spins directly to facilitate entangling gates, in terms of either speed or precision, or even to reduce crosstalk [25]. It is also possible to control multiple nuclear spins by driving only the defect electronic spin. The most straightforward way to do this is by implementing entangling gates sequentially using the techniques for addressing individual nuclear spins described in the previous section. However, the slowness of this approach can result in low entanglement and gate fidelities due to the electron's dephasing, as errors on the electron spread to the nuclei. This issue can, in principle, be addressed by applying dynamical decoupling on the electron or nuclei while new entanglement links are generated [11]; reaching long coherence times, however, requires a large number of pulses (e.g., for coherence > 1 s for an NV electronic spin, 10240 pulses are required [38]). Hence, as the number of target nuclear spins grows, the experimental overhead increases significantly.

In what follows, we show that these challenges can be largely sidestepped by creating multinuclear entanglement simultaneously rather than sequentially. To see how this works, we first discuss how to quantify multispin entanglement in these types of defect spin systems. We first consider measures of entangling power for a single nuclear spin coupled to the electron and then generalize this to multiple spins using the concept of one-tangles. In subsequent sections, we then show how to employ these measures to guide the design of multinuclear spin entangling gates.

A. Disjoined picture

The joint evolution of the electron and a single nuclear spin can be described via the Makhlin (or local)

invariants [39], typically denoted as G_1 and G_2 . These invariants classify all two-qubit operations into distinct entangling classes, such that gates sharing the same local invariants belong to the same entangling class. This property stems from the fact that local operations do not change the amount of entanglement between two parties. Entangling gates that give rise to maximum correlations are known as perfect entanglers; examples include the CNOT and CZ gates, which are locally equivalent. CNOT, CZ, and other two-qubit gates equivalent to them up to single-qubit gates have $G_1 = 0$ and $G_2 = 1$.

For any arbitrary π -pulse sequence, the electron-nuclear evolution operator after N repetitions of the sequence retains the form of Eq. (2), with ϕ_j replaced by the total rotation angle $\phi_j(N)$. This special form of the evolution operator allows us to find the analytical forms of G_1 and G_2 and, thus, to understand what type of entanglement any arbitrary π -pulse sequences can generate. In other words, knowing G_1 and G_2 allows us to classify the two-qubit gate of Eq. (2) into an entangling class and find under which conditions this gate becomes a perfect entangler. In our case, we find that G_1 and G_2 as a function of N read

$$G_1 = \left(\cos \frac{\phi_0(N)}{2} \cos \frac{\phi_1(N)}{2} + n_{01} \sin \frac{\phi_0(N)}{2} \sin \frac{\phi_1(N)}{2} \right)^2, \quad (6)$$

$$G_2 = 1 + n_{01} \sin \phi_0(N) \sin \phi_1(N) + 2 \left(\cos^2 \frac{\phi_0(N)}{2} \cos^2 \frac{\phi_1(N)}{2} + n_{01}^2 \sin^2 \frac{\phi_0(N)}{2} \sin^2 \frac{\phi_1(N)}{2} \right), \quad (7)$$

where $n_{01} \equiv \mathbf{n}_0 \cdot \mathbf{n}_1$ and with $G_1 \in [0, 1]$ and $G_2 \in [1, 3]$. Based on these ranges, one notices that π -pulse sequences can generate perfect entangling gates only in the CNOT-equivalent class, for which it holds that $(G_1, G_2) = (0, 1)$. Under the resonance condition ($n_{01} = -1$), the first Makhlin invariant simplifies to $G_1 = \cos^2[\phi_0(N) + \phi_1(N)/2]$, and requiring $G_1 = 0$ gives the number of sequence iterations needed to obtain a controlled gate. To estimate the number of repetitions N , we need only to know the rotation angles in one iteration. The minima of G_1 are located at $N = (2\kappa + 1)\pi/(\phi_0 + \phi_1)$. In general, G_1 can be zero for other N as well, as long as $\mathbf{n}_0 \cdot \mathbf{n}_1 \leq 0$. We provide the analytical expressions for N for this general case in Appendix G and use these conditions to identify nuclear spin candidates to realize simultaneous controlled gates in Sec. IV.

While Makhlin invariants are suitable for classifying two-qubit gates, a more general metric that omits details of the gate structure and focuses instead on the entanglement it can generate is the entangling power [40]. It is shown that

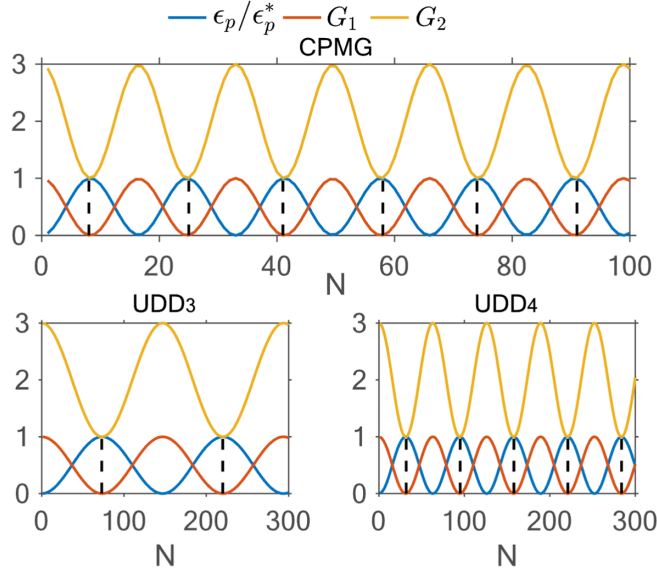


FIG. 3. Scaled entangling power (ϵ_p/ϵ_p^* , blue line) and Makhlin invariants (G_1 , red lines; G_2 , yellow lines) as a function of the number of repetitions of the CPMG (top) and UDD₃ or UDD₄ (bottom) units for a single nuclear spin. The dotted lines correspond to the analytically expected minima of G_1 (see the text). We consider the $k = 1$ resonance for each sequence. The times for the UDD _{n} sequences are optimized around the analytical resonance time $[(t_{\text{CPMG}}, t_{\text{UDD}_3}, t_{\text{UDD}_4}) = (3.1811, 3.1852, 3.1862) \mu\text{s}]$. For the nuclear spin, we set $(A, B, \omega_L) = 2\pi \cdot (60, 30, 314) \text{ kHz}$, and for the electron's spin projections $s_0 = -s_1 = 1/2$. $\epsilon_p^* = 2/9$ is the maximum value the entangling power can take.

the entangling power of a two-qubit operator can be expressed in terms of G_1 as [41]

$$\epsilon_p = \frac{2}{9}(1 - |G_1|). \quad (8)$$

It is clear that for $G_1 = 0$ the entangling power is maximized and saturates to $\epsilon_p^* = 2/9$ for the two-qubit case. In Fig. 3, we show the entangling power (scaled by $2/9$) and Makhlin invariants for the CPMG, UDD₃, and UDD₄ sequences. The vertical lines correspond to the minima of G_1 . We notice that the period of oscillations is smaller for CPMG, since the angle per iteration is greater compared to the UDD _{n} sequences (see Appendix H and Ref. [35]).

B. Assessing multispin entanglement via one-tangles

To understand the entanglement distribution in the total system (consisting of the electron and multiple nuclei), we need to extend the notion of the two-qubit entangling power. To this end, we employ the one-tangles [42,43], which measure the total amount of entanglement in a state by considering all possible bipartitions of the system. That is, by fictitiously dividing the total system into subsystems, one can quantify the degree of correlations between the subsystems (also known as the bipartition entanglement). We choose to use the one-tangle as the entanglement

metric, which means for each bipartition that we separate only one qubit (electron or nuclear spin) from the rest of the system.

One-tangles carry only the information of the entanglement capacity in the system and cannot distinguish states that belong to different families (e.g., W states versus Greenberger-Horne-Zeilinger states for the tripartite case) [44]. Such a metric is convenient, since we are interested in the general evolution of the system rather than generating particular entangled states.

Similar to the two-qubit entangling power, the one-tangles are defined through the linear entropy. For a pure state $|\psi\rangle$, the one-tangle reads

$$\tau_{g|g'}(|\psi\rangle) := 1 - \text{tr}[\rho_{g'}^2], \quad \rho_{g'} = \text{tr}_g[|\psi\rangle\langle\psi|], \quad (9)$$

where $g|g'$ denotes a bipartition of the system. Some authors include an overall multiplicative factor of 2 for the linear entropy; we choose not to follow this convention, as it simply redefines the bounds of the linear entropy and does not affect our following analysis.

Equation (9) in its current form is not particularly useful for quantifying the entanglement of multinuclear operations, since it depends on the initial state. We must, therefore, average over initial states. In particular, we use the bipartition entangling power, which is defined as the average of the one-tangle over all initial product states. This average can be computed by averaging over single-qubit unitaries U_i , applied to a fixed initial product state $|\psi_0\rangle$, that is, $|\Psi\rangle := |\psi_0\rangle^{\otimes n} = U_i^{\otimes i}|\psi_0\rangle^{\otimes i}$, giving rise to $\epsilon_{g|g'}(U) := \langle\tau_{g|g'}(U|\Psi)\rangle_{U_i}$. The index i ranges from $i = 1, \dots, n$, where n is the total number of qubit systems. In Ref. [44], it is shown that the entangling power (with one-tangles as the measure) for a bipartition $p|q$ of the system is given by

$$\epsilon_{p|q}(U) = 1 - \left(\prod_{i=1}^n \frac{d_i}{d_i + 1}\right) \sum_{x'|y'} \text{tr}\{(\text{tr}_{p|x'}[|U\rangle\langle U|])^2\}, \quad (10)$$

where $d_i = 2$ is the dimension of each qubit subsystem. The state $|U\rangle$ is defined in the context of the Choi-Jamiołkowski isomorphism [45,46], which maps any projector living in a d -dimensional Hilbert space (\mathcal{H}_d) into a state vector in an extended space ($\mathcal{H}_{d^2} \equiv \mathcal{H} \otimes \mathcal{H}'$), i.e., $|i\rangle\langle j'| \mapsto |ij'\rangle$. In our case, $d = 2^n$, where n is the number of qubits, including the electron and the nuclei. $x'|y'$ denotes a bipartition in the secondary system of the total extended space. The summation is performed over all 2^n bipartitions in \mathcal{H}' . For example, for the tripartite case, we have $x'|y' \in \{1'2'3'|, 1'2'|3', 1'3'|2', 2'3'|1', 1'|2'3', 2'|1'3', 3'|1'2', \cdot|1'2'3'\}$, where “ \cdot ” is the empty bipartition. Equation (10) is applicable for multipartite unitary gates, with q referring to a single qubit partitioned from the d -dimensional Hilbert space \mathcal{H}_d and p referring to the remaining $(d - 1)$ -dimensional subsystem. As an example,

for four qubits in total, $p|q$ can take the values $p|q \in \{123|4, 124|3, 134|2, 234|1\}$.

In the case of π -pulse sequences, the evolution operator has a special form given by

$$U = \sum_{j \in \{0,1\}} \sigma_{jj} \otimes_{l=1}^L R_{\mathbf{n}_j}^{(l)}(\phi_j^{(l)}), \quad (11)$$

where L is the total number of nuclear spins and, for conciseness, we refer to $\phi_j^{(l)}(N)$ as simply $\phi_j^{(l)}$. The evolution operator is, therefore, defined by the evolution of each nuclear spin in the disjointed picture (see Appendix A 1 for a proof). This feature allows us to obtain analytical expressions for the average of the one-tangles for any number of nuclear spins. However, we need to distinguish the case when either a single nuclear spin or the electron is partitioned from the rest of the system. For brevity, we refer to these types of average one-tangles as the one-tangle of a nuclear spin and the one-tangle of the electron, respectively.

We find that the one-tangle of a single nuclear spin, when partitioned from the remaining electron-nuclear register, is given by (see Appendix J)

$$\epsilon_{p|q}^{\text{nuclear}} = \epsilon_p^*(1 - G_1), \quad (12)$$

which holds for $n \geq 3$ qubits. For $n = 2$, the average of the one-tangle is the two-qubit entangling power of Eq. (8). G_1 is given by Eq. (6), and $\epsilon_p^* = 2/9$ is the maximum value the nuclear one-tangle can take. Note that, as is expected, the one-tangle of a nuclear spin does not depend on other quantities besides those that determine its evolution (due to the tensor product form of the total evolution operator U). In other words, partitioning a different nuclear spin from the register changes Eq. (12) through its G_1 , describing a different amount of entanglement between the partitioned spin and the remaining electron-nuclear register. Although Eq. (12) coincides with the two-qubit entangling power of Eq. (8) in the disjointed picture, the meaning of the two equations is different. If we ignore the presence of all nuclei but one, then Eq. (8) effectively tells us whether the two-qubit unitary generated by the sequence can prepare an electron-nuclear Bell state. Once we consider arbitrarily many spins, Eq. (12) does not strictly tell us how many Bell pairs we can create, as it instead describes correlations in the multispin register and, therefore, needs to respect the monogamy of entanglement.

In the case when the electron is partitioned from the system, the one-tangle reads (see Appendix J)

$$\epsilon_{p|q}^{\text{electron}} = \frac{1}{3} - \frac{1}{3^n} \prod_{i=1}^{n-1} (1 + 2G_1^{(i)}), \quad (13)$$

where $G_1^{(j)} \equiv G_1(\phi_0^{(j)}, \phi_1^{(j)}, n_{01}^{(j)})$ contains the information of the evolution of the j th nuclear spin. The one-tangle of the electron now includes contributions from the evolutions of each nuclear spin; due to the always-on nature of the HF interaction, the electron can be correlated with all nuclei. On the other hand, we see from Eq. (12) that a single nuclear spin can have explicit correlations only with the electron and evolves independently of all other nuclei (assuming no internuclear spin interactions).

Remarkably, the expressions for the one-tangles, Eqs. (12) and (13), allow us to study the entanglement distribution in an arbitrarily large nuclear spin register. Together with the knowledge of the evolution of each nuclear spin in the disjointed picture, we can simulate efficiently a large number of nuclei and obtain complete information about the dynamics of the system. The simplicity of Eqs. (12) and (13) is what allows us to obtain a detailed understanding of how entanglement gets distributed throughout the system for various pulse sequences, as we discuss in the remainder of the paper.

One thing we can immediately see from Eq. (12) is that the one-tangle of a nuclear spin is minimized when the function G_1 is maximized. This can happen when the nuclear spin undergoes a trivial evolution, namely, when $\mathbf{n}_0 \cdot \mathbf{n}_1 = 1$ ($\mathbf{n}_0 \cdot \mathbf{n}_1 = -1$) and $\phi_0 = \phi_1$ ($\phi_0 = -\phi_1$). The range of the function G_1 is shown in Figs. 4(a) and 4(b) for

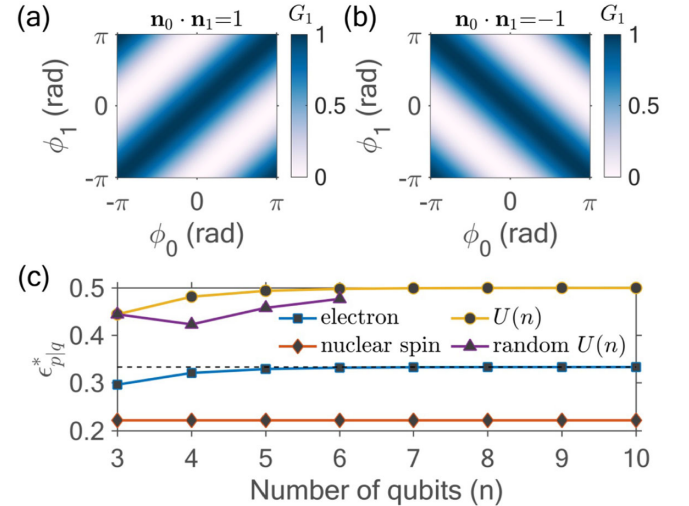


FIG. 4. Function G_1 versus the rotation angles ϕ_j for the case of $\mathbf{n}_0 \cdot \mathbf{n}_1 = 1$ (a) and $\mathbf{n}_0 \cdot \mathbf{n}_1 = -1$ (b). (c) Maximum one-tangles as a function of the number of qubits for the case when the electron (blue line) or a single nuclear spin (red line) is partitioned from the rest of the system. The yellow line is the theoretical maximum bound for a perfect $U(n)$ entangler, while the purple line is the numerical bound we find for randomly generated $U(n)$, obtained by retaining the maximal value over 100 random unitaries for $n = 4, 5$ and five random unitaries for $n = 6$. For $n = 3$, we construct a $U(n)$ from an absolutely maximally entangling (AME) state. Such $U(n)$ saturates the bound, if the AME($2n, d$) state exists (in this case, $d = 2$).

the cases of $\mathbf{n}_0 \cdot \mathbf{n}_1 = \pm 1$, respectively. Whenever $G_1 = 0$, the one-tangle of a nuclear spin is maximal, whereas when $G_1 = 1$, the nuclear spin decouples from the system. In Fig. 4(c), we show the maximum one-tangle when a single nuclear spin (red line) or the electron (blue line) is separated from the rest of the spins. As expected, the maximum nuclear one-tangle is independent of the number of total qubits in the system and saturates to the value $2/9$, which also holds for two-qubit operations. On the other hand, the electron's one-tangle shows an increase with the number of qubits until it becomes independent of n and saturates close to $1/3$.

In light of these results, it is interesting to ask whether it is possible to achieve maximal entangling power by applying π pulses to this central spin system. In Fig. 4(c), we also show the bound of the bipartition entanglement for an arbitrary n -qubit gate $U(n)$ (yellow line), which is calculated according to [44]

$$\epsilon_{p|q}^{\max} = 1 - \prod_i \frac{d_i}{d_i + 1} \sum_{x'|y'} \frac{1}{\min[d_{px'}, d_{qy'}]}, \quad (14)$$

where $d_{px'}$ and $d_{qy'}$ are the dimensions of the subsystems px' and qy' , respectively. Interestingly, this bound is never reached by π -pulse sequences. However, this upper bound is not always tight. A necessary requirement for the bound to be tight is that the CP maps associated with $U(n)$ are unital [40], which means that they map maximally mixed states onto maximally mixed states. This condition alone is not sufficient, since, as shown in Ref. [40], for the two-qubit case, the bound given by the linear entropy (which is $1/3$) is never saturated, and the well-known perfect entanglers, such as $CNOT$, can reach only the value of $2/9$. The saturation of the bound occurs when the matrix elements of $U(n)$ can be obtained from so-called absolutely maximally entangling states, known as $AME(2n, d)$, if these exist [44]. For $d = 2$ (i.e., qubit subsystems), $AME(n, d)$ states exist only for $n = 3, 5, 6$ [47]. In Fig. 4(c), we show that the bound is indeed saturated for $n = 3$ [for which $AME(2n, d)$ exists], if we construct such $U(n)$ based on Ref. [44], for an $AME(2n, d)$ state found in Ref. [48]. For $n = 4, 5, 6$, we generate random n -qubit unitaries $U(n)$ and calculate the maximum value of one-tangles; the results are depicted with a purple line. Although we do not sample a large number of $U(n)$, we see that the maximum bipartition entanglement of random unitaries exceeds the bound of the one-tangles corresponding to π -pulse sequences. Therefore, the multipartite controlled gates generated by π -pulse sequences applied to this central spin system do not saturate the one-tangle bound for $n \geq 3$, and, hence, the amount of entanglement they can create is limited.

We now illustrate the utility of Eqs. (12) and (13) by using them to design electron-nuclear entangling gates that avoid unwanted nuclei. We first consider the simplest example of two nuclei under the CPMG sequence, for an

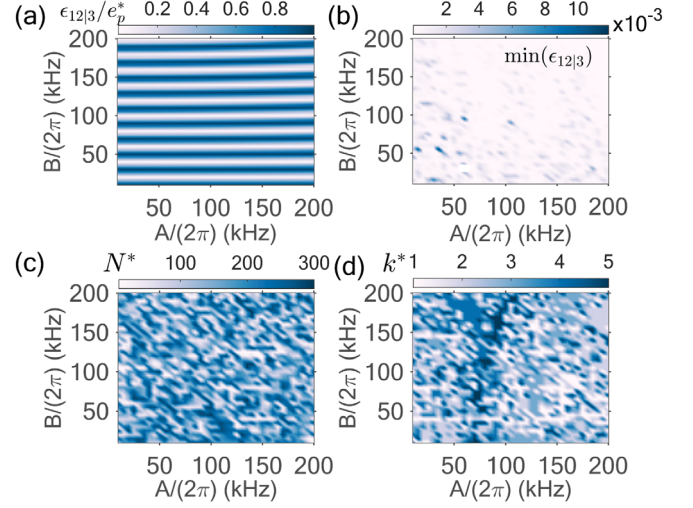


FIG. 5. Controlling a target nuclear spin with parameters $(A, B, \omega_L) = 2\pi \cdot (60, 30, 314)$ kHz, in the presence of an unwanted spin with HF parameters $\in 2\pi \cdot [10, 200]$ kHz. (a) One-tangle of the unwanted spin scaled by the maximum bound of $\epsilon_p^* = 2/9$. The time of one sequence unit is the first resonance of the target spin, and the number of iterations is $N = 25$, which maximize its one-tangle. (b) Minimization of the unwanted spin's one-tangle using the first five ($k = 1, \dots, 5$) resonances of the target spin and up to 300 pulses on the electron. Optimal sequence iterations (c) and optimal resonance (d) to minimize the unwanted spin's one-tangle while keeping the one-tangle for the target spin maximal. In all plots, we consider an electron spin $S = 1/2$ and the CPMG sequence.

electron spin $S = 1/2$. We fix the HF parameters of the target spin to be $(A, B) = 2\pi \cdot (60, 30)$ kHz and allow the HF parameters of the second spin to vary in the range $2\pi \cdot [10, 200]$ kHz. The nuclear spin Larmor frequency is set to be $\omega_L = 2\pi \cdot 314$ kHz; for ^{13}C atoms, this corresponds to a magnetic field of $B \approx 293.46$ G. Depending on the defect electronic spin, the B field should be chosen such that it ensures the MW qubit transitions are far from anticrossings, and, hence, leakage outside of the electronic qubit subspace is suppressed [32].

In Fig. 5(a), we select the first resonance of the target spin and $N = 25$ sequence iterations, which maximize its one-tangle, and show the one-tangle of the unwanted spin (scaled by the maximum value of $2/9$). In the ranges where the one-tangle of the unwanted spin is minimal, we successfully decouple it from the rest of the spins. We verify that these ranges correspond to nuclear spins whose HF parameters approximately satisfy the condition for trivial evolution; we further depict this behavior for an $S = 1$ electron system in Appendix E.

Based on Fig. 5(a), we would conclude that certain unwanted nuclei cannot be decoupled, as they show non-zero entanglement with the rest of the system. If one wishes to target a specific spin with high selectivity, then different resonance times and sequence iterations need to be considered. Note that this effect would be completely missed in

prior formulations of this problem, and the issue of insufficient decoupling would appear only in numerics, where the simulations would have to be repeated for all the different physically relevant hyperfine couplings. In Fig. 5(b), we show the minimal value of the unwanted spin's one-tangle (excluding the case of same HF parameters for the unwanted and target nuclei), which is optimized over the first five resonances of the target spin and up to 300 repetitions of the sequence. We search only over iterations that generate maximal entanglement between the target nucleus and electron, which we obtain from the minima of G_1 . The optimal iterations and resonances are shown in Figs. 5(c) and 5(d), respectively. The optimization yields minimum one-tangles on the order of approximately 10^{-3} for the unwanted spin, providing isolation for the electron-target nuclear spin system. We conclude that using the analytical expressions of the one-tangles to minimize unwanted one-tangles via optimization of the parameters of the π -pulse sequence provides a faithful metric of selectivity with a single target spin.

Lastly, it is interesting to note that Fig. 5(a) reveals that the unwanted spin's one-tangle can be maximal (depending on its HF parameters) at the same time t and repetitions N we choose for the target spin. This feature is further studied in Sec. IV and paves the path to identifying nuclei that synchronously undergo controlled gates.

IV. SYNCHRONOUS CONTROLLED GATES ON MULTIPLE NUCLEI

A. Maximization of multiple one-tangles

As we saw in Sec. III B, one-tangles corresponding to different nuclei can be maximized or minimized simultaneously and for the same number of repetitions of the sequence unit. This suggests that, instead of generating entanglement with single spins sequentially, one can simultaneously entangle multiple nuclei with the electron. In this section, we confirm that this is indeed the case.

To see how such direct generation of multispin entanglement is possible, we devise a simple strategy of identifying nuclei whose one-tangles become simultaneously maximal. To demonstrate our method, we select nuclei randomly from the HF range $2\pi \cdot [10, 200]$ kHz. There are two relevant parameters we need to decide how to fix: the time t of one unit of the sequence and the repetitions N . We fix t by setting it equal to a chosen resonance of the first randomly selected nucleus. For this nucleus, we find the iterations that maximize its one-tangle, based on the minima of G_1 , and store these into the set $\tilde{N}^{(1)}$. Since the time we choose does not, in principle, coincide with a resonance of other randomly selected nuclei (as the HF parameters differ), it holds, in general, that $\mathbf{n}_0 \cdot \mathbf{n}_1 \neq -1$ for these nuclei, meaning that we need a reliable way of estimating iterations that maximize their one-tangles. As long as $\mathbf{n}_0 \cdot \mathbf{n}_1 \leq 0$ for a single nuclear spin, the one-tangle can be maximal for some N . We

explain how we find the maxima (analytically for CPMG and UDD₃ and numerically for UDD₄) in Appendix G. Based on the maxima, we assign to each nucleus a set $\tilde{N}^{(j)}$, similar to what we did for the first nucleus. Then, we search for a common intersection, i.e., one number of iterations of the sequence that belongs to multiple sets $[\cap_{j=1}^{n-1} \tilde{N}^{(j)}]$. The first set we fix is that of the first randomly chosen spin, and then we test its intersection with the remaining sets. Nuclear spins whose sets have zero intersection with this initial fixed set are removed. In the end, we obtain a particular value of iterations (N^*) and nuclear spin candidates that can participate in a multipartite gate.

In the simulations that follow, we assume an electron spin $S = 1/2$ that could correspond to SiV⁻ or SnV⁻ defect in diamond [49–52]. We further set the nuclear Larmor frequencies to be $\omega_L = 2\pi \cdot 314$ kHz. The HF range $2\pi \cdot [10, 200]$ kHz we choose for the nuclei, for instance, corresponds to the median of the HF distribution for an isotopic concentration of approximately 10^{-3} in SiC [36]. Such nuclei are weakly coupled, since the HF parameters are smaller than $1/T_2^*$, which is typically a few megahertz [53,54] for NV centers, or, in general, for $A, B \ll 1$ MHz [55] (approximately 1 MHz is also the electron linewidth for the neutral divacancy in SiC [36]). For HF strengths $> 2\pi \cdot 6$ kHz, the nuclei are within a distance of $R < 15$ Å from the vacancy site, while for strengths on the order of $2\pi \cdot 1$ kHz, they are within $R \sim 25$ Å [56]. More precise ranges of HF values and distances from the vacancy are shown in Table I. The HF values for our following simulations, and estimations of the nuclear positions relative to the vacancy, are listed in Appendix K 1. To ensure that the spins selected via random generation are distinct, we give a bound on how different the HF values

TABLE I. Range of hyperfine parameters and corresponding distances from the vacancy site for ¹³C atoms and ²⁹Si atoms in diamond or SiC. Explicit values (A, B) are shown in parentheses; otherwise, we provide approximate ranges.

HF range ($\frac{A}{2\pi}, \frac{B}{2\pi}$) (MHz)	Distance from vacancy site (Å)	Atoms
100–200 [57]	1.61 (first neighbor)	¹³ C (NV diamond)
About 10–20 [57] (19.4,13.9) [58]	3.86 (third neighbor)	¹³ C (NV diamond, C _g [58])
About 4 [59]	3 (sites G and H)	¹³ C (NV diamond)
About 2 [60]	5	¹³ C (NV diamond)
HF range ($\frac{A}{2\pi}, \frac{B}{2\pi}$) (kHz)	Distance from vacancy site (Å)	Atoms
60–120 [61]	6.8	¹³ C (NV diamond)
20–50 [61]	8–9	¹³ C (NV diamond)
2–20 [61]	11.5	¹³ C (NV diamond)
(10,29) [62]	11.6	²⁹ Si (SiC)
(0.65,11.45) [36]	12.4	²⁹ Si (SiC)

should be; e.g., for CPMG, we require that at least one of the HF values differs by at least $2\pi \cdot 25$ kHz from the rest. This bound is set to a reasonable value so that we generate enough nuclei within the HF range but with distinct enough HF values. In the following, we study two different resonances for CPMG, UDD₃, or UDD₄, and, for each resonance, we perform a distinct random generation of nuclei.

Considering the first resonance ($k = 1$ of one of the target spins) and using the CPMG sequence, we show ten nuclear spin one-tangles [Fig. 6(a)] that are maximized for a unit time $t = 3.1874 \mu\text{s}$. In Fig. 6(b), we show the dot product of the rotation axes of each of the ten nuclei. It is apparent that the axes of each spin are nearly antiparallel, since, for $k = 1$, the individual resonance times have only a

small deviation from $t = 3.1874 \mu\text{s}$. Consequently, the only way for the one-tangles to be maximized is that the nuclei rotate with $\phi_0(N^*) = \phi_1(N^*) \approx \pi/2$ [see Eq. (6)], and, hence, the realized gate is close to a multipartite $\text{CR}_x(\pi/2)$. It is interesting to notice that, based on Table II, nuclear spins 6 and 7, 2 and 5, and 4 and 8, as well as spins 1 and 9, have similar A values. In Ref. [21], it is reported that two weakly coupled nuclear spins (one of them is a spectator unwanted nucleus) show similar A values, and, thus, the controlled gate on one of them also rotates the other one (potentially leading to unwanted residual entanglement), but this effect is not quantified in their quantum error correction scheme.

In Figs. 6(c) and 6(d), we again show nuclear spin one-tangles and rotation axis dot products but now for the

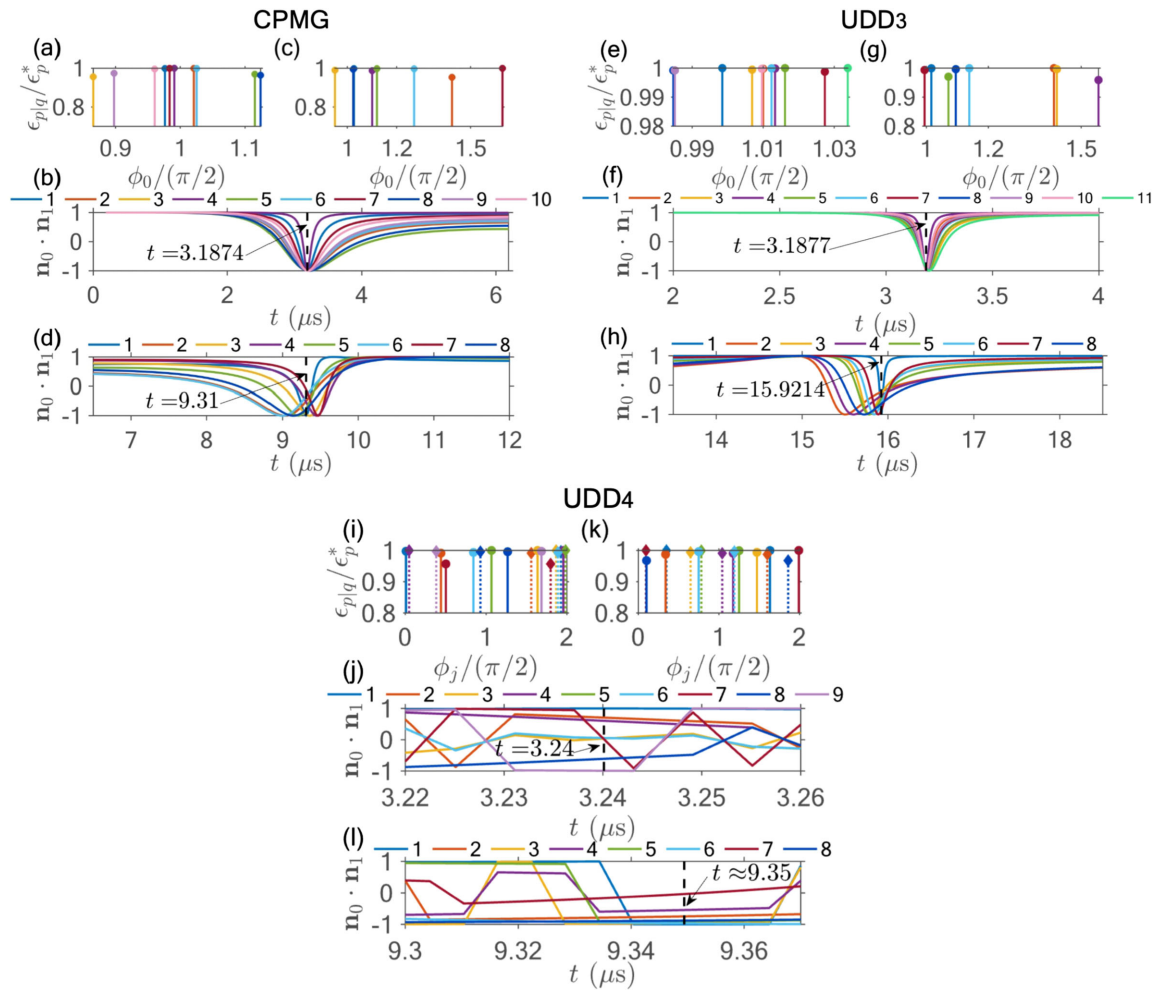


FIG. 6. Nuclear one-tangles (scaled by the maximum value $\epsilon_p^* = 2/9$) versus accumulated rotation angle for CPMG (a) $[(N^*, k) = (56, 1)]$ and (c) $[(N^*, k) = (8, 2)]$, UDD₃ (e) $[(N^*, k) = (487, 1)]$ and (g) $[(N^*, k) = (93, 3)]$, and UDD₄ (i) $[(N^*, k) = (252, 1)]$ and (k) $[(N^*, k) = (41, 2)]$. The different lines correspond to nuclear spins that we label with an integer index j . The dot product of nuclear rotation axes close to $k = 1$ CPMG resonance (b), $k = 2$ CPMG resonance (d), $k = 1$ UDD₃ resonance (f), $k = 3$ UDD₃ resonance (h), $k = 1$ UDD₄ resonance (j), and $k = 2$ UDD₄ resonance (l). The vertical lines in the dot product panels denote the common time of the basic unit used to evaluate the corresponding one-tangles and is the resonance of nuclear spin “1.” In (i) and (k), the lines with circles correspond to ϕ_0 and the lines with diamonds to ϕ_1 . The nuclear spins for each set (N^*, k) of each sequence are different and are provided in Tables II (CPMG), III (UDD₃), and IV (UDD₄) in Appendix K.

$k = 2$ resonance. As the order of the resonance increases, the individual resonance times show a larger dispersion, leading to nuclear rotation axes that deviate from being antiparallel. For multiple nuclei to be (close to) maximally entangled with the electron, they would then have to compensate for this feature by rotating by an angle ϕ_0 that differs from $\pi/2$ [Fig. 6(c)].

We can perform a similar analysis for the UDD₃ sequence for which again the rotation angle of each nucleus is independent of the electron's state, i.e., $\phi_0 = \phi_1$. The basic UDD₃ unit now contains an odd number of pulses and, thus, needs to be repeated twice. For this reason, the UDD₃ angle per iteration is smaller than those of CPMG or UDD₄ (see Appendix H and Ref. [35]), implying higher precision on the accumulated angle but slower multipartite gates. This behavior is verified in Fig. 6(e), where we plot the one-tangles of 11 nuclear spins versus their accumulated rotation angle, which is very close to $\pi/2$. As the first resonance is very sharp [see Fig. 6(f)], the nuclear rotation axes are very close to antiparallel. This gives rise to very high entanglement but a long sequence with $N^* = 487$ repetitions. However, one can impose restrictions on the total time and still find very high one-tangles for the $k = 1$ UDD₃ resonance.

On the other hand, for $k = 3$ [Fig. 6(h)], the resonance is broader, and, hence, the rotation angles of the target nuclei deviate, in general, from $\pi/2$ [Fig. 6(g)], similar to what we observed for CPMG. The $k = 1$ UDD₃ resonance leads to higher entanglement, since the unit time is smaller than for $k = 3$, implying greater precision in the accumulated rotation angle per iteration. Of course, one reason for the difference between the two resonances is the random selection of HF values, which is distinct in the two cases. In addition, the chosen number of sequence repetitions might not be optimal for $k = 3$. It is not surprising that particular resonances and iterations can lead to better nuclear spin control, as the rotation angle depends on both the sequence time and N . Since N takes discrete values, this implies that features of over- or underrotation result in imperfect entanglement.

Lastly, we consider the UDD₄ sequence. In this case, the rotation angle of each spin depends on the electron's state, and we cannot estimate analytically the maxima of one-tangles; instead, we identify them via numerical search. In Fig. 6(i), we show the one-tangles versus the rotation angles (ϕ_j) for nine nuclei selected from the randomly distributed ensemble, for $k = 1$ [lines with circles (diamonds) show ϕ_0 (ϕ_1)]. The dot product of the nuclear axes is shown in Fig. 6(j). Even though the dot product shows nontrivial jumps (due to $\phi_0 \neq \phi_1$), one can still obtain appreciable entanglement with multiple nuclei. The one-tangles in Fig. 6(k) and the dot products in Fig. 6(l) correspond to the $k = 2$ resonance. The entangling operations for UDD₄ are, in general, faster than for UDD₃, since the former induces a larger nuclear spin rotation.

An interesting feature that emerges from $\phi_0 \neq \phi_1$ is that the nuclei undergo a more complicated evolution, and entanglement generation can occur for multiple sets of rotation angles and axes. For example, we see that in both Figs. 6(i) and 6(k) it can happen that $[\phi_0(N^*), \phi_1(N^*)] \approx (0, \pi)$ (or vice versa), realizing a CR(π) operation with that particular nuclear spin [see Table IV in Appendix K 1]. This is not surprising, since, based on Eq. (6) for $\mathbf{n}_0 \cdot \mathbf{n}_1 = 0$ [see spin "7" in Fig. 6(l)], $G_1 = 0$ if either $\phi_0(N)$ or $\phi_1(N)$ is $(2\kappa + 1)\pi$.

B. Effect of unwanted spins on gate fidelity

Using the language of one-tangles, we showed that it is possible to realize direct multipartite gates, providing a speedup compared to sequential entanglement-generation schemes. However, the gate fidelity could still be affected by unwanted nuclei, especially if these become entangled with the electron. We now examine this issue.

To keep the discussion general, let us consider L nuclear spins in total, with K of them corresponding to the target nuclei that show maximal one-tangles. The $L - K$ unwanted nuclei affect the target gate, since, in general, they have a nonzero degree of entanglement with the electron. This means that projecting the evolution operator onto the target subspace would result in a nonunitary gate. In Appendix A 2, we show how this can be avoided by using the Kraus operator representation of the partial trace channel, based on which we can work directly with the total evolution operator and do not need to specify an initial state for the system. The operator-sum representation [63] allows us to derive an analytical expression for the gate fidelity of the target subspace. As a target gate U_0 , we consider the evolution operator of the K target spins in the absence of the unwanted spins, i.e.,

$$U_0 = \sum_{j \in \{0,1\}} \sigma_{jj} \otimes_{k=1}^K R_{\mathbf{n}_j^{(k)}}(\phi_j^{(k)}). \quad (15)$$

Using the analytical expressions for the Kraus operators, we find that the target subspace gate fidelity reads

$$F = \frac{1}{2^{K+1} + 1} \left(1 + 2^{K-1} \sum_{k=0}^{2^{L-K}-1} \left| \sum_{j \in \{0,1\}} c_j^{(k)} p_j^{(k)} \right|^2 \right), \quad (16)$$

where $c_j^{(i)}$ and $p_j^{(i)}$ are given in Appendix A 2. The summation is performed over the 2^{L-K} Kraus operators of the unwanted subspace. The expression of the gate fidelity depends solely on the parameters describing the unwanted spins' evolution, since we assume that U_0 is the evolution that would occur in the absence of any unwanted spins. The gate fidelity is clearly maximized when $\sum_{k=0}^{2^{L-K}-1} \left| \sum_{j \in \{0,1\}} c_j^{(k)} p_j^{(k)} \right|^2 = 2^2$. This happens when the unwanted spins evolve trivially (i.e., independently

of the electron's spin state), which is an immediate consequence of the minimization of unwanted nuclear spin one-tangles.

To understand the impact of an unwanted spin bath on the target evolution, we consider as our target nuclear spins three different groups from Sec. IV A: (i) those we identified at the $k = 2$ CPMG resonance, (ii) those at the $k = 3$ UDD₃ resonance, and (iii) those at the $k = 2$ UDD₄ resonance. That is, we use the eight target nuclear spins we found for each of the three sequences in Fig. 6 whose HF parameters are given in Tables II (CPMG, $k = 2$), III (UDD₃, $k = 3$), and IV (UDD₄, $k = 2$) in Appendix K. For each case, we construct an ensemble of unwanted nuclear spins with randomly distributed HF parameters and identify those with one-tangles in the range $[0, 0.76]$. As the target gate operation, we consider the evolution of the target spins of Eq. (15) in the absence of unwanted nuclei. The gate error arises once we introduce unwanted nuclei, let them interact with the electron, and then trace them out to obtain the effective evolution in the target subspace. In reality, we never assume an initial state or trace out nuclei, since we can use Eq. (16) to find the gate error by using only the information of the unwanted spins' evolution.

As a concrete example, we gradually build up a bath of at most six unwanted, spectator nuclei one at a time, in each case examining the impact on the gate error. We are interested in studying the effect of both the number of unwanted nuclei and the size of their one-tangles on the gate fidelity. To do this, we start with an ensemble of 3×10^5 sets of randomly distributed HF parameters (A and B), with each set differing by at least 3 kHz from the rest in at least one of the HF components (A or B). This ensemble is such that the corresponding one-tangles span the range $[0, 0.76]$. We then assign each set of HF parameters into one of 31 bins depending on the value of the corresponding one-tangle. In most cases, the size of each one-tangle bin is chosen to be about 2–3 times the order of magnitude of the one-tangles in that bin (e.g., for one-tangles on the order of 10^{-3} , we define the following three bins: $[2, 4] \times 10^{-3}$, $[4, 6] \times 10^{-3}$, and $[6, 8] \times 10^{-3}$), although we choose the bin sizes to saturate at about 0.02 for larger one-tangles, as otherwise the gate infidelity quickly approaches one. The nuclear spin bath is formed by selecting one of these bins and introducing l unwanted nuclei, where each nucleus assumes a distinct set of HF parameters randomly selected from that bin. We vary l from 1 to 6 (i.e., the total bath size is at most six spins). This construction allows us to systematically investigate the impact of both the bath size and one-tangle size simultaneously.

In Fig. 7(a), we depict the infidelity $1 - F$ corresponding to the CPMG sequence as a function of which one-tangle bin is used to form the unwanted nuclear spin bath. For each bin, we gradually increase the number of unwanted nuclei that contribute to the infidelity, starting from 1 and

increasing up to 6. Because of the random distribution of HF parameters, it might be the case that there are fewer than six spins in some of these intervals (especially for low values of the one-tangle), in which case we show the gate error as we trace out a smaller number of spins. As expected, the gate error grows as we increase the size of the nuclear spin environment or as its entanglement with the target subsystem becomes substantial (as indicated by the magnitude of the one-tangle). However, some nuclei can evolve trivially under the CPMG sequence, in particular, those whose HF parameters obey the conditions for trivial evolution shown in Sec. II B. In Fig. 7(b), we show the gate error versus the one-tangles of unwanted spins that satisfy the condition for trivial evolution. All one-tangles are trivially zero, leading to a vanishing gate error.

In Figs. 7(c) and 7(d), we show the infidelity of the multipartite gate under the UDD₃ or UDD₄ evolution. We notice that for UDD₄ the one-tangles are distributed at higher values. This is a direct consequence of the more complicated dynamics that the nuclei undergo for this sequence. Recall that multiple conditions allow nuclei to entangle with the electron due to the fact that their individual rotation angles ϕ_0 and ϕ_1 are different.

It is interesting to note that, for some values of one-tangles, the gate error shows jumps and becomes very large. It is not surprising that this is possible even at relatively small values of one-tangles (approximately 10^{-2}) [see Fig. 7(c)]. The reason for this behavior is that the unwanted spins could cause the evolution to deviate from the ideal isolated evolution of Eq. (15). However, the resulting gate may have a larger overlap with other target gates. Here, we choose not to optimize over the resulting gate, as we want to show the overall tendency of the target subspace gate error as the entanglement of unwanted spins with the remaining system increases. In Appendix A 2, we provide a modified gate fidelity formula if one wishes to optimize over single-qubit gates acting on the target nuclei.

Although we do not optimize over the sequence parameters and target spin HF parameters, we see that a CPMG sequence with only $N^* = 8$ repetitions and a total time of $T \approx 74.5 \mu\text{s}$ is still capable of entangling eight different nuclear spins with the electron and preserving the multipartite gate operation, in general, on par with UDD₄. However, both UDD sequences are longer in this scenario and require a larger number of sequence iterations than CPMG ($T = 1.48 \text{ ms}$ and $N^* = 93$ for UDD₃, while $T \approx 0.38 \text{ ms}$ and $N^* = 41$ for UDD₄). Even though we do not compare directly the sequences (as their parameters differ), we see that resorting to long sequences does not necessarily imply enhanced protection of the target evolution. Moreover, in an experimental setup, it is preferable to use a smaller number of sequence iterations to limit potential pulse errors. Experimentally and numerically, it is shown that CPMG outperforms UDD₆ [28] in decoupling capabilities, which is in agreement with a soft cutoff

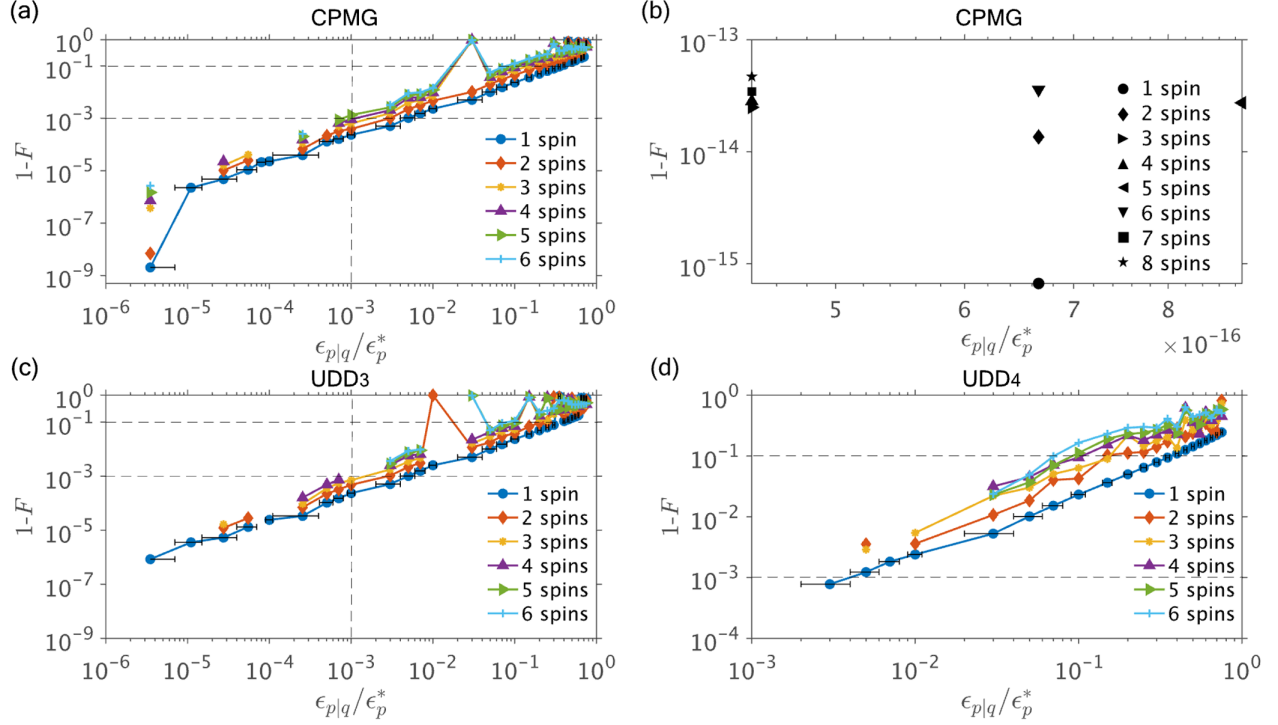


FIG. 7. Gate error $1 - F$ as a function of one-tangles (scaled by the maximum value $\epsilon_p^* = 2/9$) of unwanted nuclear spins for (a),(b) the CPMG, (c) the UDD₃, and (d) the UDD₄ sequences. The labels in all graphs show up to how many spins are “traced out” from the total system. The unwanted spins have one-tangles in the range $[0, 0.76]$. The error bars of the blue points show the intervals of one-tangles to which we assign unwanted spins and are the same for all differently colored lines. For one-tangle bins where we cannot find up to six distinct sets of HF parameters, we include data only up to a smaller number of unwanted spins for which distinct sets can be found. In (b), we use the condition for the trivial evolution to identify unwanted nuclei which do not introduce any gate error. The dashed lines in the plots serve as a guide to the eye.

Lorentzian noise spectrum. Further comparison of the gate performance for CPMG, UDD₃, and UDD₄ can be found in Appendix K 2, where we average over eight different ensembles of randomly generated unwanted nuclei for each sequence.

C. Multipartite gates in a 27 nuclear spin register

Up to this point, we have studied the qualitative behavior of multipartite gates for randomly distributed nuclear spins. In this section, we consider an ensemble of 27 ¹³C atoms near an NV center ($S = 1$) in diamond, using HF parameters experimentally determined via 3D spectroscopy by the Taminiau group [32,64]. Our goal is to gain an understanding of what multispin entangling gates can be achieved in this system with high fidelity and gate speed. We focus on multipartite gates generated by CPMG sequences applied to the NV spin. We set the magnetic field to $B = 403$ G [32], which translates into a Larmor frequency of $\omega_L \approx 2\pi \cdot 432$ kHz for the ¹³C nuclei. We further select the electron’s spin projections to be $s_0 = 0$ and $s_1 = -1$.

To identify target nuclear spins, we could use our analytical expressions to find the number of iterations that maximize multiple one-tangles. Instead, we perform a more systematic search over 135 distinct driving sequences, each

characterized by the choice of CPMG unit time and the number of iterations. Each sequence is tuned close to one of the first five resonances of one of the 27 nuclei. Thus, each of the 135 sequences can be labeled by nucleus j and resonance k , where $j \in [1, 27]$ and $k \in [1, 5]$. For each such resonance, we vary the CPMG unit time over a window of ± 0.25 μ s around the resonance time. We further perform a search over the number of iterations by constraining the total time of the gate to be ≤ 1.5 ms. In this way, we restrict the gate time within T_2^* of the nuclei, which ranges from 3 to 17 ms [32]. For each of the 135 sequences, we select the unit time and number of iterations that ensure the following criteria are met: (i) one-tangles of target nuclei > 0.8 , (ii) one-tangles of unwanted nuclei < 0.14 , and (iii) mean value of unwanted one-tangles < 0.1 . After we find the potential sets of (t, N^*) which fulfill all the above requirements, we choose a set that can simultaneously entangle two or more nuclear spins with the electron. If no such set exists, we ignore that case. In the end, we calculate the gate fidelity of the target subspace for each of the groups of (t, N^*) in the presence of the remaining unwanted spectator nuclei. This procedure allows us to systematically identify how many other nuclei can be efficiently and reliably entangled with a given nuclear spin.

The computation of nuclear spin one-tangles requires only the information of the independent evolution of each nucleus. Hence, this allows us to simulate many nuclear spins without computational difficulty. The gate fidelity, on the other hand, involves 2^{L-K} Kraus operators ($L = 27$ and K is the number of target nuclei), which translates into $2 \times 2^{L-K}$ additions [see Eq. (16)]. As an example, a single run for $K = 7$ target spins and, thus, 20 unwanted spins (approximately 2×10^6 additions) calculates the gate fidelity within about 8 s, but for $K = 2$ (approximately 67×10^6 additions) it takes about 4.5 min (computational times are without parallel computing). However, it is still advantageous that we can do such computations without explicitly defining the Kraus operators.

We display our results for all 135 driving sequences in Fig. 8. Each sequence is labeled by a case number equal to $j + (k - 1) \cdot 27$, where $j \in [1, 27]$ labels the primary nucleus being targeted and $k \in [1, 5]$ labels one of its first five resonances. In Fig. 8(a), we show the mean of target one-tangles, while in Fig. 8(b), we show the mean of the unwanted one-tangles. The first 27 cases are shown with blue lines ($k = 1$), the next 27 with red lines ($k = 2$), and so on. As expected, higher-order resonances, in principle, give rise to lower residual entanglement with unwanted spins [35]. In Fig. 8(c), we show the number of target nuclei

whose one-tangle mean is the one in Fig. 8(a). In general, as the order of the resonance k increases, nuclei tend to decouple more efficiently, since the resonant times show larger dispersion, and, hence, the number of target nuclei decreases. In Figs. 8(d) and 8(e), we show the number of iterations and total gate time. Higher-order resonances require fewer sequence repetitions, since the accumulated nuclear rotation angle per iteration is larger. Finally, in Fig. 8(f), we show the gate error of the entangling operation. The first resonance yields the highest error, since the spectator nuclei have larger residual entanglement with the target spins. The optimization tries to balance the trade-off between maximum achievable entanglement (i.e., target one-tangles > 0.8) and minimum gate error. Requiring lower values of individual unwanted one-tangles could reduce the gate error more.

We should further comment that the HF parameters of the 27 nuclear spins are smaller than the randomly generated ones in Sec. IVA (see Appendixes K 1 and K 3). It is then a natural consequence that the gate times for the multipartite gates presented in this section are longer. Experimentally, one could identify better candidates for target nuclei to maximize the entanglement in the nuclear spin register while satisfying time constraints. Using target nuclear spins with a bit larger HF parameters could reduce the total gate time.

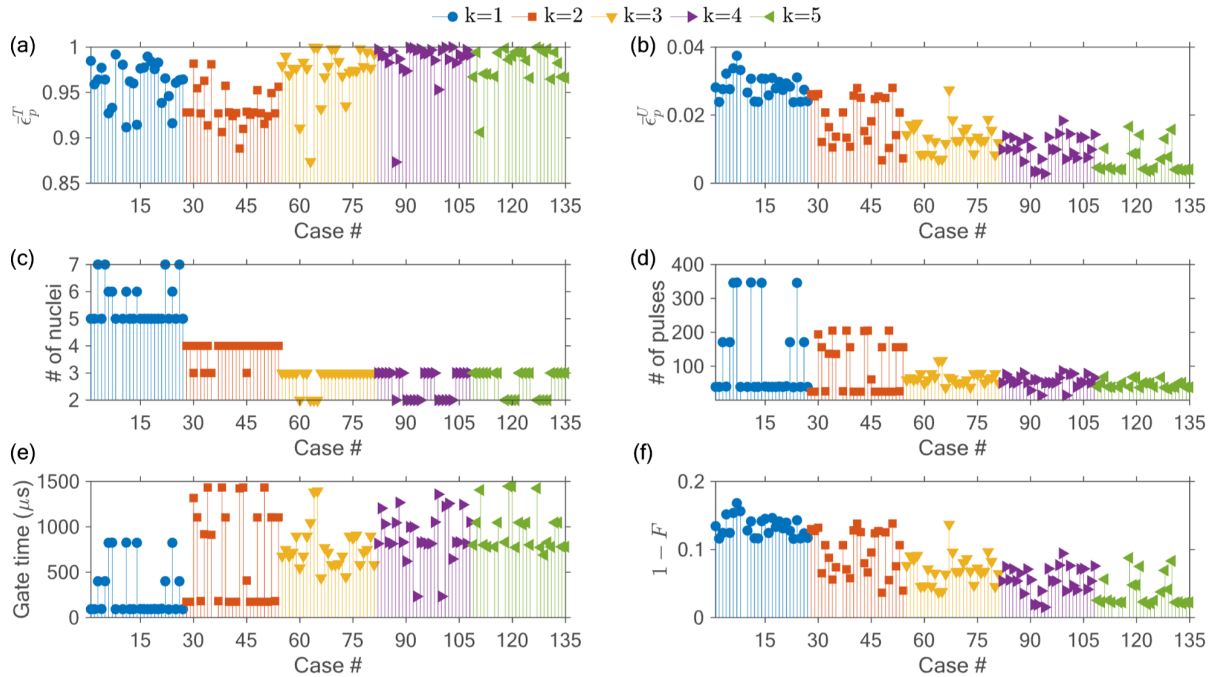


FIG. 8. Performance of 135 distinct multipartite gates in a 27 nuclear spin register using the CPMG sequence. Each gate is labeled by a case number, which is equal to $j + (k - 1) \cdot 27$, where $j \in [1, 27]$ labels nuclei and $k \in [1, 5]$ labels resonances. Each gate is generated by a different driving sequence determined by the CPMG unit time and number of iterations, with the former tuned close to the k th resonance of nucleus j . (a) Mean value of target nuclei one-tangles for each gate; each target one-tangle contributing to the mean is scaled by the maximum value of $2/9$. (b) Mean value of unwanted nuclei one-tangles; each unwanted one-tangle contributing to the mean is scaled by the maximum value of $2/9$. (c) Number of target spins participating in each multipartite gate. (d) Number of iterations and (e) gate time of each multipartite gate. (f) Gate error due to residual entanglement with unwanted nuclear spins.

In addition, over- or underrotation errors that cause the one-tangles of the target nuclei to deviate from their maximum values could potentially be remedied by direct driving of a few nuclear spins or by using hybrid sequence protocols as in Ref. [35]. However, our results indicate that multipartite entangling operations can be reliably implemented with gate fidelities above 0.95 for $k > 1$ even without such measures.

D. Speedup of controlled gates for QEC

Practical applications, such as quantum error correction (QEC), require gate durations to be much smaller than T_2^* of the spins which participate in the protocol to ensure reliable performance. Many QEC schemes require repeating a sequence of operations and/or measurements multiple times, and, thus, it is crucial to perform the gate operations fast; for example, one QEC cycle of Ref. [22] lasts for approximately 2.99 ms. More specifically, for the three nuclei that participate in this QEC scheme [22], the durations of each sequential electron-nuclear entangling gate are 980, 400, and 1086 μs , respectively. The accumulation of errors due to decoherence during long gates could be partially alleviated by applying refocusing pulses to extend coherence times [25]. However, such techniques add to the experimental overhead, making it desirable to use them only sparingly or not at all if possible; such methods can be avoided if we can accelerate the entangling gates by involving multiple nuclei in the operation simultaneously. The question we address now is how fast and reliably can we perform such a single-shot operation in comparison with the sequential entanglement generation scheme.

To demonstrate the advantages offered by the synchronous controlled gates, we select as an example case 23 for $k = 3$ of the previous section (see Table VIII of Appendix K 3). For this realization, we entangle simultaneously nuclei $\{C4, C5, C15\}$ with the electron, with total gate time $T = 582.22 \mu\text{s}$, individual one-tangles $e_{p|q}^{\text{nuclear}} = \{0.999\,94, 0.996\,62, 0.997\,56\}$ (scaled by $2/9$), and a gate error due to residual entanglement with the remaining 24 unwanted nuclei of $1 - F = 0.067977$.

To compare the performance of this direct multispin operation against sequential entanglement protocols, we perform another simulation where we entangle each C_j nucleus [$j \in \{4, 5, 15\}$] one at a time with the electron starting with C4. We impose constraints on the sequential gates that are similar to those on the single-shot operation in order to compare the two schemes fairly (see Appendix K 4 for further discussion). For a more direct gate fidelity comparison (comparable decoupling efficiency and selectivity) between the two schemes, we restrict the duration of each sequential entangling gate to be within 1.5 ms as we did for the multispin scheme.

For each C_j nucleus, we identify sequence parameters that yield optimal $\text{CR}_x(\pi/2)$ gates while satisfying the various constraints we impose. In particular, we search over the first ten resonances, $k \in [1, 10]$, for each spin and

number of CPMG iterations, choosing the values that maximize the target one-tangle while minimizing the rest within the chosen time constraints. For C4, we find that the optimal gate time is $T \approx 0.93$ ms with an error due to residual entanglement of $1 - F = 0.1133$. By performing only this single entangling gate, we already exceed the gate time of approximately 0.58 ms of the multipartite operation. For C5, we find that a $\text{CR}_x(\pi/2)$ gate can be performed at the shortest gate time of approximately 68 μs , which leads to a gate error of $1 - F = 0.1045$. The results for C15 are rather surprising; although we search over ten different resonances, the best $\text{CR}_x(\pi/2)$ gate we can achieve is long (approximately 1.344 ms), and the error ($1 - F = 0.1421$) is larger than that of the other two entangling gates.

Overall, we see that the sequential gates for the $\{C4, C5, C15\}$ set lead to significant gate error, since these fail to decouple each nucleus from the remaining spin bath effectively. The total gate time of the sequential entangling operations is approximately 2.342 ms, already 4 times larger than the gate time of the multipartite gate on $\{C4, C5, C15\}$. Furthermore, the sets we identify as target spins for the multispin gates in Sec. IV C contain nuclei, which, when we attempt to address them individually, lead to electron-nuclear entangling gates that suffer from crosstalk arising from the other nuclear spins of the set. Indeed, this is verified by the gate error sources we identify (see Table VIII in Appendix K 3); for example, the infidelity of the C4 entangling gate is due to nonzero residual entanglement of the electron with the C15 nucleus. Similar observations hold for the errors of the other two sequential gates. Thus, our formalism not only provides a faithful metric of nuclear spin selectivity, but identifies crosstalk issues and optimal nuclear spin candidates for performing entangling gates within time constraints.

In Fig. 9, we compare the multispin protocol with the sequential entanglement generation scheme. In the latter case, the gates are very close to $\text{CR}_x(\pm\pi/2)$ [see Figs. 9(f)–9(h) and Table XI in Appendix K 4]. The gates acting on the nuclei in the multipartite case, in principle, have both nonzero x - and z -axis components [see Figs. 9(b)–9(d) and Table XI in Appendix K 4]. Although the gates of the two approaches are different, they are equivalent up to local rotations.

E. Three-qubit bit-flip code

Continuing with the 27 nuclear spin register from above, let us now consider a three-qubit measurement-free QEC protocol that does not require stabilizer measurements or ancillary qubits and can correct a single bit- or phase-flip error [65]. Our goal is to protect the initial state of the electron. Using two nuclei which we assume are initialized into the $|1\rangle$ state, we show how to use the CR_{xz} multispin operations to recover the electron's state from a single bit-flip error. We also compare the performance of this

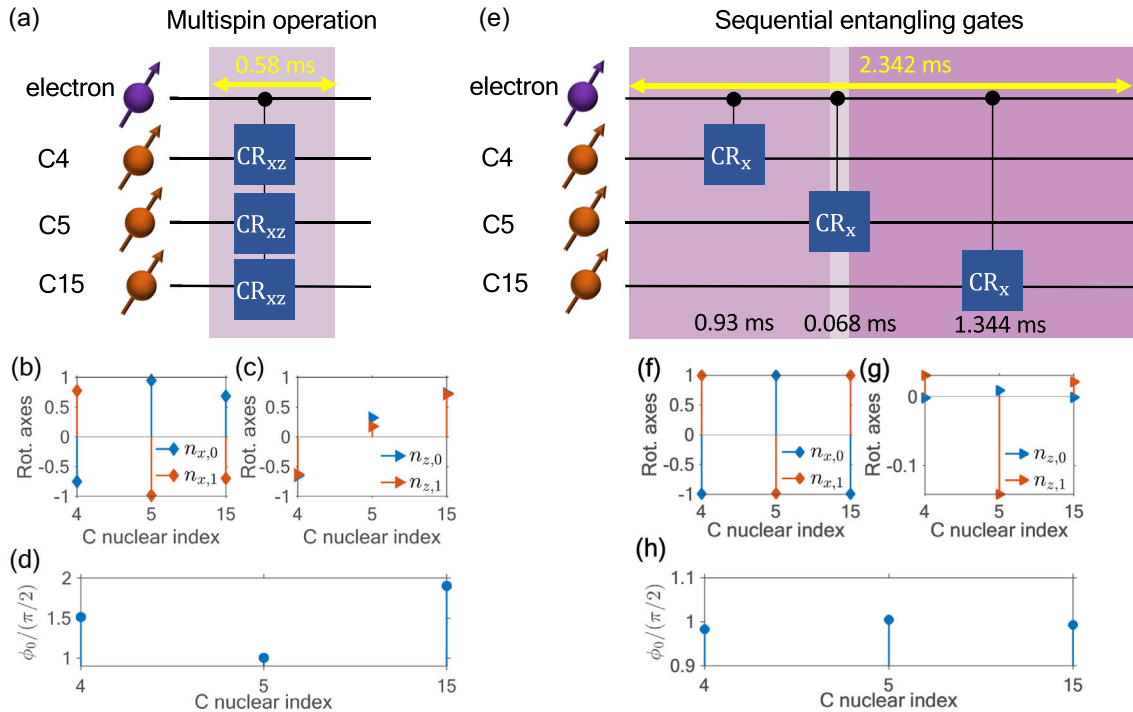


FIG. 9. Comparison of synchronous multispin gate scheme with the sequential entanglement protocol. Circuit diagram for (a) multispin entangling gate operation and (e) sequential entangling protocol. The x -axis components (b),(f) and the z -axis components (c),(g) of the ^{13}C nuclear spin rotations are shown. The subscripts “0” and “1” on the axis components refer to the nuclear rotations R_{n_j} . (d),(h) The rotation angle of each nucleus. (b)–(d) correspond to the multispin operation, while (f)–(h) correspond to the sequential entangling protocol. The exact parameters of the rotation axes and rotation angles are given in Table XI in Appendix K 4. Lighter shading in (a) and (e) indicates shorter gate durations.

approach with the sequential entangling gate protocol. In the following analysis, we restrict our full numerical simulations of the QEC protocol to include only the three spins comprising the code (the electron and the two nuclei that are part of the protocol), since we cannot simulate the full density matrix of 28 spins. However, our analysis still incorporates the effects of the full nuclear spin bath, since each gate of the protocol is designed by minimizing the one-tangles of the bath spins, as described in the previous section. We use our results from the previous section to guide both our choice of which two nuclei should participate in the QEC protocol as well as the control parameters.

The QEC protocol consists of three parts: (i) the encoding of the electron’s physical state into a logical state, (ii) the decoding, and (iii) the correction. The latter is performed by decomposing the three-qubit Toffoli gate (controlled on the nuclei) using single- and two-qubit gates [65]. The entire QEC circuit of the sequential protocol can be found in Appendix K 5 and Ref. [65]. Such a measurement-free QEC protocol is realized experimentally in Ref. [21], where very high theoretical fidelities (in excess of 99%) of electron-nuclear entangling gates are reported. However, in Ref. [21], it is mentioned that these estimates do not account for the presence of unwanted nuclei, which leads to extra loss of electron coherence. Here, we show

explicitly that the presence of the unwanted spin bath can have a significant impact on the implementation of target operations, especially when it undergoes substantial entanglement with the electron.

To explain the principles of the multispin three-qubit QEC protocol, suppose that we wish to recover an arbitrary state of the electron from an X error that happens after the encoding. We implement the encoding and decoding using the CR_{xz} gate. The QEC circuit needs to be “aware” of the absence of bit-flip errors, so that it leaves the electron’s state intact. This means that the encoding and decoding gates need to combine to flip the initial $|11\rangle$ state of the nuclei into $|00\rangle$, such that the subsequent Toffoli gate is not activated, if no bit-flip error happens. Because of the more complicated dynamics induced by the multispin gates, this requirement is not satisfied by the encoding or decoding CR_{xz} gates alone. We resolve this issue by introducing unconditional $R_y(-\pi)$ gates on the nuclei in between the two encoding or decoding CR_{xz} gates; this ensures that the encoding or decoding and $R_y(-\pi)$ gates compose together so as to flip the nuclei and deactivate the subsequent Toffoli gate (see Appendix K 5 for a proof).

The correction circuit is composed of unconditional nuclear and electron rotations, as well as $CR_x(\pi/2)$ gates. For simplicity, we treat the additional $R_y(-\pi)$ rotations that

we require as part of the encoding and the gates of the correction circuit as ideal. We do not find the optimal parameters to perform the correction gates, since we would numerically optimize and implement them in the same way for both the sequential and the multispin schemes. The $R_y(-\pi)$ rotations can be implemented by direct driving of the nuclei or composed through unconditional R_x and R_z gates obtained via dynamical decoupling sequences [65], through appropriate tuning of the inter-pulse spacing of the sequence.

Besides leaving the electron's state intact when no error occurs, the QEC circuit also needs to recover its state after a bit-flip error. A bit flip on the electron (occurring after the encoding) makes the rotation that each nucleus undergoes during the encoding differ from the one it undergoes during the decoding. The success of our protocol lies in the fact that now the CR_{xz} and $R_y(-\pi)$ gates combine to rotate the nuclei approximately about the z axis. This means that the nuclei return close to the $|11\rangle$ state, activating the subsequent Toffoli gate that corrects the bit-flip error. The evolution of the nuclei up to the decoding involves also a nonvanishing x -axis rotation. Consequently, at the end of the decoding, the nuclei are not fully disentangled from the electron. However, the x rotation is quadratically suppressed by the nuclear Larmor frequency (see Appendix K 5), meaning that the recovery operation brings the electron close to its initial state, but, as we quantify shortly, the electron's final state is slightly mixed.

To illustrate the performance of the multispin QEC scheme, we start with the recovery of the electron state $|y\rangle$ from a bit-flip error. We consider case 22 and $k = 4$ of the multispin gates in Fig. 8, for which we entangle the electron with nuclei C10 and C12. The gate error due to residual entanglement with unwanted spins is $1 - F \approx 0.04$, and the gate time is $T \approx 645.6 \mu\text{s}$. In Fig. 10(a), we show the coefficients of the three-qubit state at each step of the circuit, prior to the encoding and up to the correction step. We find that the probability of recovering the electron's state is 99.63%. The electron's reduced density matrix [Fig. 10(b)] after tracing out the two nuclei verifies that it is close to the desired $|y\rangle\langle y|$ state; the purity is found to be 99.26%. In Fig. 10(c), we show the error probability, defined as $1 - |\langle \psi_{\text{el},0} | \psi_{\text{final}} \rangle|^2$ ($|\psi_{\text{el},0}\rangle$ is the electron's initial state and $|\psi_{\text{final}}\rangle$ the final three-qubit state) for arbitrary initial states $|\psi_{\text{el},0}\rangle = \cos(\gamma/2)|0\rangle + e^{i\delta}\sin(\gamma/2)|1\rangle$. We find that, in all cases, we recover the electron's state with an error on the order of approximately 10^{-3} .

We perform a similar analysis for the recovery of the $|\pi/3\rangle = \cos(\pi/6)|0\rangle + \sin(\pi/6)|1\rangle$ state, now for case 13 and $k = 4$ in Fig. 8. For this realization, we again entangle the electron with nuclei C10 and C12; the gate duration is $T \approx 827 \mu\text{s}$, and the gate error due to residual entanglement is $1 - F \approx 0.0152$. In Fig. 10(d), we show the coefficients of the three-qubit state, and, in Fig. 10(e), the electron's

reduced density matrix, whose purity is 99%. We find that the recovery probability is 99.5%. In Fig. 10(f), we show the error probability for arbitrary initial states of the electron. In Figs. 10(g) and 10(h), we show the evolution of each nuclear spin up to the decoding step. The blue arrows indicate the initial state of the nuclei, which is the $|1\rangle$ state. The green (red) curves show the path each nucleus traces on the Bloch sphere if the electron starts from the $|0\rangle$ ($|1\rangle$) state and undergoes a bit flip. The final green and red arrows indicate that the nuclei return approximately to the $|11\rangle$ state, such that the Toffoli gate then corrects the electron's bit flip. In the case when no bit flip occurs, both nuclei traverse a great arc on the Bloch sphere and end up exactly in the $|0\rangle$ state at the end of the decoding [see Appendix K 5].

We now compare our direct multispin protocol with the sequential three-qubit QEC code. For a fair comparison, we impose constraints on the sequential entangling gates that are similar to those of the multispin operation. By searching over the first ten resonances of C12 or C10, we find a list of acceptable $CR_x(\pi/2)$ gates [see Table XII in Appendix K 6]. For C12, the $CR_x(\pi/2)$ gate can be implemented with error $1 - F = 0.0238$ due to unwanted residual entanglement and a duration of $449.4277 \mu\text{s}$. This gate is faster than the two cases of multispin operations mentioned previously [although faster multispin gates were found in Fig. 8], with an error lower than case 22 and $k = 4$ but higher than case 13 and $k = 4$. Note that, in Fig. 8, the multispin gates are restricted to $k \leq 5$, but, to implement the $CR_x(\pi/2)$ gate reliably, we expand the search over $k \geq 5$, as higher-order resonances are needed for improved selectivity for the sequential scheme. Addressing the C10 nucleus is much more challenging than addressing C12. In the time constraint of 1.5 ms, the lowest infidelity is approximately 0.384; imposing a new constraint of 5 ms, we find that the $CR_x(\pi/2)$ gate can be implemented for a duration of about 3 ms with an infidelity of approximately 0.106.

The sequential scheme can, in principle, succeed with a recovery probability of 100%, assuming all gates are error-free, since the disentanglement in the decoding step can be perfect (see Appendix K 5). Nevertheless, errors due to unresolved residual entanglement reduce the probability of recovering the electron's initial state. That is, tracing out unwanted spins and the nuclei of the protocol yields, in general, a mixed density matrix for the electron. Thus, in cases when crosstalk errors cannot be resolved by the sequential scheme, the recovery probability is expected to be smaller for the sequential protocol compared to the multispin scheme, and the electron's reduced density matrix more mixed at the end of the correction.

For both protocols, it is necessary to implement the correction $CR_x(\pi/2)$ gates reliably. The advantage of the multispin QEC scheme lies in the fact that it can reduce the encoding and decoding durations by utilizing the

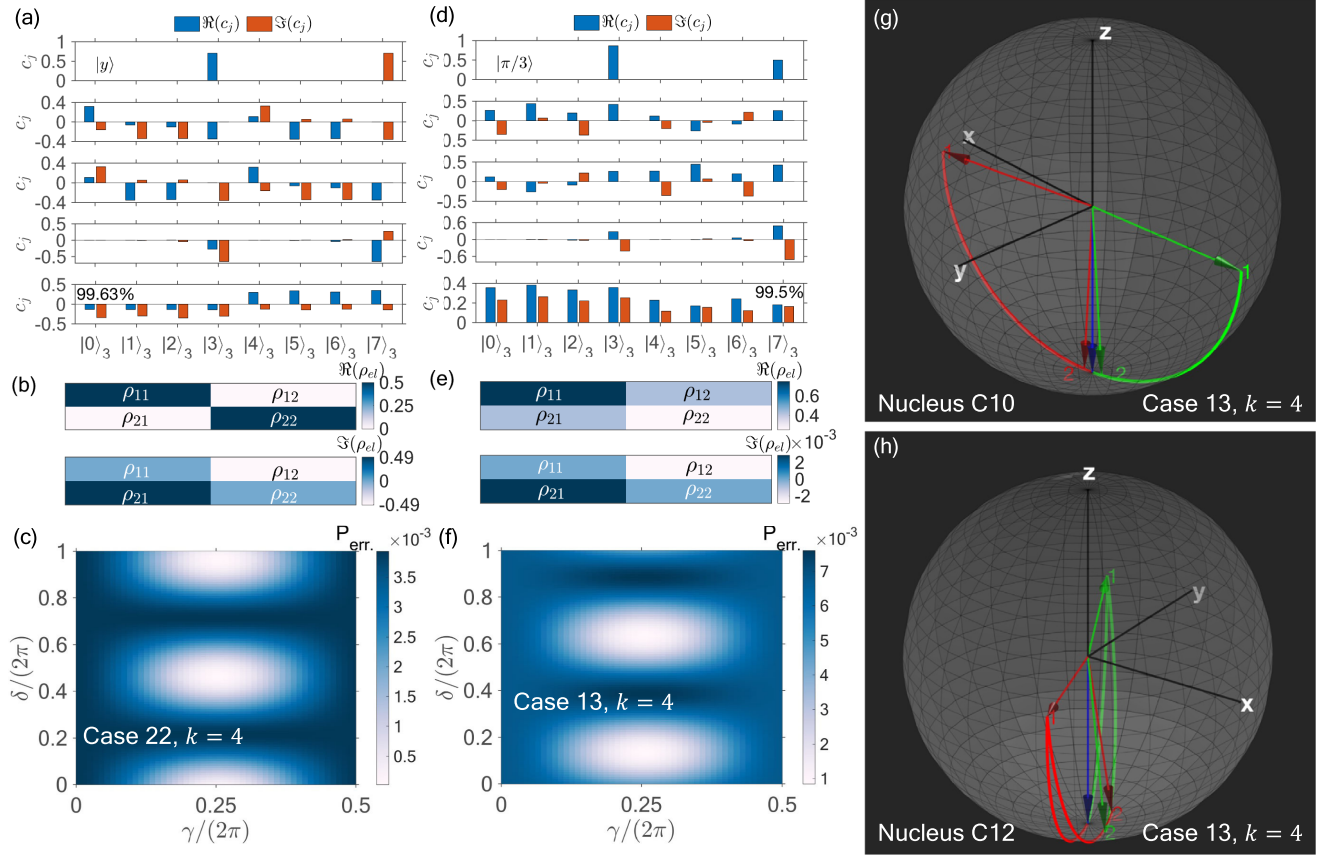


FIG. 10. Three-qubit bit-flip code using the CR_{xz} multispin operations. The electron's state is encoded into three physical qubits, two of which correspond to the ^{13}C atoms C10 and C12. (a) Recovery of the electron state $|y\rangle$ [case 22, $k = 4$ in Fig. 8]. (d) Recovery of the electron state $|\pi/3\rangle = \cos(\pi/6)|0\rangle + \sin(\pi/6)|1\rangle$ [case 13, $k = 4$ in Fig. 8]. From top to bottom, (a),(d) show the coefficients of the initial, encoded, error, decoded, and corrected state. Blue (red) bars are the real (imaginary) parts of the coefficients. The probability to measure the electron in $|y\rangle$ in (a) is 99.63% while to measure it in $|\pi/3\rangle$ in (d) is 99.5%. Real and imaginary components (b),(e) of the final reduced density matrix of the electron verify the recovery of the initial state. Error probability $1 - |\langle\psi_{el,0}|\psi_{\text{final}}\rangle|^2$ of measuring the incorrect state of the electron at the end of the QEC code for case 22 and $k = 4$ (c) and for case 13 and $k = 4$ (f). $|\psi_{el,0}\rangle$ is defined as $\cos(\gamma/2)|0\rangle + e^{i\delta}\sin(\gamma/2)|1\rangle$. Evolution of ^{13}C atoms C10 (g) and C12 (h) up to the decoding step, when the electron undergoes a bit flip. The initial state is $|1\rangle$ for each nucleus (blue arrow). The nuclei follow the green curve evolution if the electron is initially in $|0\rangle$ or the red curve evolution if it is initially in $|1\rangle$. After an error happens on the electron and we perform the decoding, the nuclei approximately return to $|11\rangle$ such that the subsequent Toffoli gate corrects the bit-flip error.

CR_{xz} operations, while to ensure reliable $\text{CR}_x(\pi/2)$ correction gates, we can allow more relaxed time constraints for the Toffoli implementation. In this way, we save time during the first two parts of the QEC scheme. On the other hand, the entire sequential QEC scheme relies on the successful performance of the $\text{CR}_x(\pi/2)$ gates, which are implemented using the same optimal sequence parameters for all parts of the circuit. Thus, in the sequential QEC scheme, one might have to trade off gate fidelity with speed of operations, and the total duration of the gates can quickly exceed the coherence times.

Interestingly, both protocols can be combined to provide optimal performance of the QEC codes. For example, reliable and fast $\text{CR}_x(\pi/2)$ encoding or decoding gates could be combined with CR_{xz} encoding or decoding gates

to address subsets of nuclei that cannot be resolved individually within given time constraints. Considering that the number of spinful nuclei in experimental conditions could be hundreds, it is highly likely that particular $\text{CR}_x(\pi/2)$ gates fail to provide both speed of operation and selectivity of a single spin. This is verified, for example, in Ref. [25], wherein certain electron-nuclear Bell-state fidelities are as low as 63% due to unresolved crosstalk arising from nearby nuclei, combined with loss of coherence due to long two-qubit operations. Inability to address nuclei individually means that they would have to be excluded from any protocol (i.e., decoupled such that they do not induce errors) but could become a valuable resource using the multispin gates. The CR_{xz} encoding or decoding gates would be accompanied by $R_y(-\pi)$

unconditional rotations on these nuclear spin subsets, which, as we mentioned previously, are required for the multispin QEC scheme.

Our analysis shows that the multispin entangling gates can drastically reduce the entanglement generation time and mitigate dephasing issues. In a measurement-free QEC scheme, the entanglement generation speedup could be crucial for protecting the logical state; leaving it unprotected for a shorter duration reduces the probability of errors occurring during the decoding step. Additionally, the synchronous controlled gates can outperform the sequential entanglement schemes, especially when we cannot resolve crosstalk issues. An interesting future direction would be to examine further the utility of CR_{xz} gates for QEC protocols and potentially adjust the correction circuit to account for the imperfect disentanglement at the end of the decoding.

V. CONCLUSIONS

Nuclear spins are an essential component of spin-based solid-state platforms for quantum networks. Harnessing their full potential to create large-scale quantum networks requires a detailed understanding of and precise control over the entanglement distribution in the system. We showed how to quantify the entanglement in a multinuclear spin register coupled to a single electron qubit and presented a faithful metric for nuclear spin selectivity. We studied the properties of CPMG, UDD₃, and UDD₄ sequences and extended their resonance conditions to arbitrary electron systems for applicability to any defect qubit in diamond or SiC. We further showed how to implement synchronous controlled gates on multiple nuclei by driving the electron appropriately. Such multipartite gates provide a speedup over the conventional way of generating sequential entanglement links, especially for large nuclear spin registers, where the total sequence time can exceed the dephasing time. We quantify the performance of multipartite gates implemented by CPMG, UDD₃, or UDD₄ sequences in the presence of unwanted nuclear spins, revealing that the gate fidelity tends to decrease as the residual entanglement with the unwanted bath becomes significant. Using experimental parameters for 27 ¹³C atoms in close proximity to an NV center in diamond, we have further verified that such multipartite gates can be performed reliably and with high fidelity and can facilitate implementations of quantum error correction codes.

ACKNOWLEDGMENTS

The authors thank Vlad Shkolnikov, Arian Vezvaei, and Filippos Tzimkas Dakis for useful discussions. E. B. acknowledges support from National Science Foundation (NSF) Grant No. 1847078. S. E. E. acknowledges support from NSF Grant No. 1838976.

APPENDIX A: MATHEMATICAL DESCRIPTION OF MULTISPIN NUCLEAR REGISTER

1. Evolution operator of multiple spins

We mention in the main text that π -pulse sequences generate an evolution operator which is a sum of terms, each of which includes an electron spin projector tensored with a product of single-qubit gates acting on the nuclei. Here, we show this explicitly. Let us consider for simplicity two nuclear spins, with HF parameters A_l and B_l [$l \in \{1, 2\}$]. Neglecting internuclear spin interactions, the secular Hamiltonian is given by

$$\begin{aligned} H &= \frac{\omega_L}{2} (\mathbb{1} \otimes \sigma_z \otimes \mathbb{1} + \mathbb{1} \otimes \mathbb{1} \otimes \sigma_z) + \frac{A_1}{2} Z_e \otimes \sigma_z \otimes \mathbb{1} \\ &\quad + \frac{B_1}{2} Z_e \otimes \sigma_x \otimes \mathbb{1} + \frac{A_2}{2} Z_e \otimes \mathbb{1} \otimes \sigma_z + \frac{B_2}{2} Z_e \otimes \mathbb{1} \otimes \sigma_x \\ &= \sum_{j \in \{0,1\}} \sigma_{jj} \otimes \left[\frac{\omega_L + s_j A_1}{2} \sigma_z \otimes \mathbb{1} + \frac{s_j B_1}{2} \sigma_x \otimes \mathbb{1} \right. \\ &\quad \left. + \frac{\omega_L + s_j A_2}{2} \mathbb{1} \otimes \sigma_z + \frac{s_j B_2}{2} \mathbb{1} \otimes \sigma_x \right] \\ &= \sum_{j \in \{0,1\}} \sigma_{jj} \otimes (H_j^{(1)} \otimes \mathbb{1} + \mathbb{1} \otimes H_j^{(2)}), \end{aligned} \quad (\text{A1})$$

where we define $H_j^{(l)}$:

$$H_j^{(l)} = \frac{\omega_L + s_j A_l}{2} \sigma_z^{(l)} + \frac{s_j B_l}{2} \sigma_x^{(l)}, \quad (\text{A2})$$

with $\sigma_x^{(l)}$ and $\sigma_z^{(l)}$ being the Pauli matrices which act on the l th spin (and the identity acts on the other spin). As a concrete example, let us focus on the CPMG sequence ($t/4 - \pi - t/2 - \pi - t/4$). Its evolution operator over one unit of the sequence (which consists of two pulses) has the form

$$U = \sigma_{00} \otimes e^{-i\tilde{h}_0} e^{-2i\tilde{h}_1} e^{-i\tilde{h}_0} + \sigma_{11} \otimes e^{-i\tilde{h}_1} e^{-2i\tilde{h}_0} e^{-i\tilde{h}_1}, \quad (\text{A3})$$

where

$$\tilde{h}_j = \frac{t}{4} (H_j^{(1)} \otimes \mathbb{1} + \mathbb{1} \otimes H_j^{(2)}). \quad (\text{A4})$$

Notice that $[H_j^{(1)} \otimes \mathbb{1}, \mathbb{1} \otimes H_j^{(2)}] = 0$, and, thus, we can write down the total evolution operator as

$$U = \sum_{j \in \{0,1\}} \sigma_{jj} \otimes R_{n_j}^{(1)}(\phi_j^{(1)}) \otimes R_{n_j}^{(2)}(\phi_j^{(2)}), \quad (\text{A5})$$

where $R_{n_0}^{(1)}(\phi_0^{(1)}) = e^{-iH_0^{(1)}t/4} e^{-iH_1^{(1)}t/2} e^{-iH_0^{(1)}t/4}$ [$R_{n_1}^{(1)}(\phi_1^{(1)}) = e^{-iH_1^{(1)}t/4} e^{-iH_0^{(1)}t/2} e^{-iH_1^{(1)}t/4}$], and similarly for $R_{n_j}^{(2)}(\phi_j^{(2)})$. Therefore, if more nuclear spins are considered, their

Hamiltonians commute, and, thus, one obtains a tensor product of single-qubit rotations acting on the nuclei.

2. Kraus operators and gate fidelity

In the main text, we mention that the unwanted nuclei affect the gate fidelity of target nuclei when the former have nonzero entanglement with the target subspace. Here, we provide the steps to obtain the formula for the gate fidelity of the target subspace.

One way to describe the evolution of the target subspace in the presence of unwanted spins is by tracing out the latter. This procedure can be performed on the density matrix level, but this requires that we specify an initial state for the system. To avoid this limitation, we can instead describe the same partial-trace channel using the operator-sum representation [63]. The elements of the partial-trace channel are Kraus operators, defined via a chosen complete basis for the environment (i.e., the unwanted spins). Since one can choose any complete basis, the Kraus operators are not unique. Using the operator-sum representation then, one can naturally extend the fidelity of a general quantum operation into the form [66]

$$F = \frac{1}{m(m+1)} \sum_k \text{tr}[(U_0^\dagger E_k)^\dagger U_0^\dagger E_k] + |\text{tr}[U_0^\dagger E_k]|^2, \quad (\text{A6})$$

where $m = 2^{K+1}$ is the dimension of the target subspace (consisting of the electron and K target spins), whereas E_k are the Kraus operators of the quantum channel described by $\mathcal{E}(\rho) = \sum_k E_k \rho E_k^\dagger$, and they satisfy the completeness relation $\sum_k E_k^\dagger E_k = \mathbb{1}$.

We assume L nuclear spins in total, with K target ones and, hence, $L - K$ unwanted. The environment is, thus, spanned by 2^{L-K} basis states. We further assume that we have permuted the total evolution operator U such that the target spins appear first in the tensor product with the electron's projector and the unwanted spins appear in the last positions, i.e.,

$$U = \sum_{j \in \{0,1\}} \sigma_{jj} \otimes_{k=1}^K R_{\mathbf{n}_j^{(k)}}(\phi_j^{(k)}) \otimes_{l=1}^{L-K} R_{\mathbf{n}_j^{(k+l)}}(\phi_j^{(k+l)}). \quad (\text{A7})$$

Without loss of generality, we consider the initial state of the environment to be $|e_0\rangle \equiv |0\rangle^{\otimes(L-K)}$, which when extended to the total space becomes $|e_0\rangle = \mathbb{1}_{K+1 \times K+1} \otimes |0\rangle^{\otimes(L-K)}$. Here, $\mathbb{1}_{K+1 \times K+1}$ is the identity gate acting on the space of target spins and the electron. We further define the complete computational basis $\{|e_i\rangle\}_{i=0}^{2^{L-K}-1}$, where all $|e_i\rangle$ states correspond to all possible bit strings of zeros and ones. The states $|e_i\rangle$ are again extended into the total space as $|\tilde{e}_i\rangle = \mathbb{1}_{K+1 \times K+1} \otimes |e_i\rangle$. With these definitions we are now

ready to introduce the expression for the i th Kraus operator of the partial-trace quantum channel:

$$\begin{aligned} E_i &= \langle \tilde{e}_i | U | e_0 \rangle \\ &= \sum_{j \in \{0,1\}} \sigma_{jj} \otimes_{k=1}^K R_{\mathbf{n}_j^{(k)}}(\phi_j^{(k)}) \\ &\quad \times \{ \langle e_i | [\otimes_{l=1}^{L-K} R_{\mathbf{n}_j^{(k+l)}}(\phi_j^{(k+l)})] | 0 \rangle^{\otimes(L-K)} \}. \end{aligned} \quad (\text{A8})$$

If for the state $|e_i\rangle$ the m th nuclear spin of the environment is in state $|0\rangle$, then we have

$$\langle 0 | R_{\mathbf{n}_j^{(m)}}(\phi_j^{(m)}) | 0 \rangle = \cos \frac{\phi_j^{(m)}}{2} - i n_{z,j}^{(m)} \sin \frac{\phi_j^{(m)}}{2}, \quad (\text{A9})$$

and whenever the m th ket is $|1\rangle$ we have

$$\langle 1 | R_{\mathbf{n}_j^{(m)}}(\phi_j^{(m)}) | 0 \rangle = -i (n_{x,j}^{(m)} + i n_{y,j}^{(m)}) \sin \frac{\phi_j^{(m)}}{2}. \quad (\text{A10})$$

Suppose that, out of the $L - K$ spins in the environment, M of them are in $|0\rangle$ and the other $L - K - M$ are in state $|1\rangle$. Substituting Eqs. (A9) and (A10) into Eq. (A8), we obtain the final form of the i th Kraus operator:

$$E_i = \sum_j c_j^{(i)} p_j^{(i)} \sigma_{jj} \otimes_{k=1}^K R_{\mathbf{n}_j^{(k)}}(\phi_j^{(k)}), \quad (\text{A11})$$

where we define $c_j^{(i)} \equiv \prod_{m=M}^{m_M} [\cos(\phi_j^{(m)}/2) - i n_{z,j}^{(m)} \times \sin(\phi_j^{(m)}/2)]$ and $p_j^{(i)} \equiv \prod_{s=s_1}^{s_{L-K-M}} [-i(n_{x,j}^{(s)} + i n_{y,j}^{(s)}) \times \sin(\phi_j^{(s)}/2)]$ while $\{n_x, n_y, n_z\}$ correspond to the rotation axis components of each nuclear spin. In the case when $M = L - K$ (i.e., $|e_i\rangle = |0\rangle^{\otimes(L-K)}$), it holds that $p_j^{(i)} = 1$, and, in the case when $M = 0$ (i.e., $|e_i\rangle = |1\rangle^{\otimes(L-K)}$), it holds that $c_j^{(i)} = 1$.

The last element we need to evaluate the expression of the gate fidelity for the target subspace is the target gate operation U_0 . We take as our target gate the evolution operator of the K target spins in the absence of the unwanted spins, i.e.,

$$U_0 = \sum_{j \in \{0,1\}} \sigma_{jj} \otimes_{k=1}^K R_{\mathbf{n}_j^{(k)}}(\phi_j^{(k)}). \quad (\text{A12})$$

By substituting Eqs. (A12) and (A11) into Eq. (A6), we find that the expression of the gate fidelity reads

$$\begin{aligned}
F &= \frac{1}{m(m+1)} \left(\text{tr} \left[\sum_{k=1}^{2^{L-K}} E_k^\dagger E_k \right] + \sum_{k=1}^{2^{L-K}} |\text{tr}[U_0^\dagger E_k]|^2 \right) \\
&= \frac{1}{m(m+1)} \left(m + \sum_k \left| \text{tr} \left[\sum_j c_j^{(k)} p_j^{(k)} \sigma_{jj} \otimes \mathbb{1}_{2^k \times 2^k} \right] \right|^2 \right) \\
&= \frac{1}{m(m+1)} \left(m + \sum_k \left| \text{tr} \left[\sum_j c_j^{(k)} p_j^{(k)} \sigma_{jj} \right] \text{tr}[\mathbb{1}_{2^k \times 2^k}] \right|^2 \right) \\
&= \frac{1}{2^{K+1}(2^{K+1}+1)} \left(2^{K+1} + 2^{2K} \sum_k \left| \sum_{j \in \{0,1\}} c_j^{(k)} p_j^{(k)} \right|^2 \right) \\
&= \frac{1}{2^{K+1}+1} \left(1 + 2^{K-1} \sum_k \left| \sum_{j \in \{0,1\}} c_j^{(k)} p_j^{(k)} \right|^2 \right), \quad (\text{A13})
\end{aligned}$$

where we use the fact that U_0 is a $2^{K+1} \times 2^{K+1}$ target gate and the Kraus operators E_k are projectors with dimension $2^{K+1} \times 2^{K+1}$, as well as the trace property of the Kronecker product $\text{tr}[A \otimes B] = \text{tr}[A]\text{tr}[B]$.

In Sec. IV B, we mention that one can optimize the gate fidelity over the target gate. For a generic target gate, it is difficult to find a closed-form expression of the gate fidelity. For this reason, we assume a target gate of the form

$$U_0 = \sum_{\rho \in \{0,1\}} \sigma_{\rho\rho} \otimes_{k=1}^K R_{\mathbf{n}'_\rho}(\phi_{\rho'}^{(k)}), \quad (\text{A14})$$

where now one would have to optimize over the single-qubit rotations that act on the target nuclear spins. Again, the first step is to calculate $U_0^\dagger E_i$ which gives

$$\begin{aligned}
U_0^\dagger E_i &= \sum_\rho \sum_j p_j^{(i)} c_j^{(i)} \sigma_{\rho\rho} \sigma_{jj} \otimes_{k=1}^K R_{\mathbf{n}'_\rho}(\phi_{\rho'}^{(k)}) R_{\mathbf{n}'_j}(\phi_j^{(k)}) \\
&= \sum_j p_j^{(i)} c_j^{(i)} \sigma_{jj} \otimes_{k=1}^K \left\{ \left[\cos \frac{\phi_j^{(k)}}{2} + i\boldsymbol{\sigma} \cdot \mathbf{n}'_j^{(k)} \sin \frac{\phi_j^{(k)}}{2} \right] \left[\cos \frac{\phi_j^{(k)}}{2} - i\boldsymbol{\sigma} \cdot \mathbf{n}_j^{(k)} \sin \frac{\phi_j^{(k)}}{2} \right] \right\} \\
&= \sum_j p_j^{(i)} c_j^{(i)} \sigma_{jj} \otimes_{k=1}^K \left\{ \cos \frac{\phi_j^{(k)}}{2} \cos \frac{\phi_j^{(k)}}{2} + (\boldsymbol{\sigma} \cdot \mathbf{n}'_j^{(k)}) (\boldsymbol{\sigma} \cdot \mathbf{n}_j^{(k)}) \sin \frac{\phi_j^{(k)}}{2} \sin \frac{\phi_j^{(k)}}{2} \right. \\
&\quad \left. - i\boldsymbol{\sigma} \cdot \left[\mathbf{n}_j^{(k)} \sin \frac{\phi_j^{(k)}}{2} \cos \frac{\phi_j^{(k)}}{2} - \mathbf{n}'_j^{(k)} \sin \frac{\phi_j^{(k)}}{2} \cos \frac{\phi_j^{(k)}}{2} \right] \right\} \\
&= \sum_j p_j^{(i)} c_j^{(i)} \sigma_{jj} \otimes_{k=1}^K C_j^{(k)}. \quad (\text{A15})
\end{aligned}$$

Evaluating the trace gives

$$\begin{aligned}
\text{tr}[U_0^\dagger E_i] &= \sum_j \text{tr}[p_j^{(i)} c_j^{(i)} \sigma_{jj}] \prod_{k=1}^K \text{tr}[C_j^{(k)}] = \sum_j p_j^{(i)} c_j^{(i)} \prod_{k=1}^K 2 \left(\cos \frac{\phi_j^{(k)}}{2} \cos \frac{\phi_j^{(k)}}{2} + \mathbf{n}_j^{(k)} \cdot \mathbf{n}'_j^{(k)} \sin \frac{\phi_j^{(k)}}{2} \sin \frac{\phi_j^{(k)}}{2} \right) \\
&= 2^K \sum_j p_j^{(i)} c_j^{(i)} f_j, \quad (\text{A16})
\end{aligned}$$

where we define $f_j = \prod_{k=1}^K (\cos(\phi_j^{(k)}/2) \cos(\phi_j^{(k)}/2) + \mathbf{n}_j^{(k)} \cdot \mathbf{n}'_j^{(k)} \sin(\phi_j^{(k)}/2) \sin(\phi_j^{(k)}/2))$. Finally, the fidelity expression reads

$$\begin{aligned}
F &= \frac{1}{2^{K+1}(2^{K+1}+1)} \left(2^{K+1} + 2^{2K} \sum_{i=1}^{2^{L-K}} \left| \sum_j p_j^{(i)} c_j^{(i)} f_j \right|^2 \right) \\
&= \frac{1}{2^{K+1}} \left(1 + 2^{K-1} \sum_{i=1}^{2^{L-K}} \left| \sum_j p_j^{(i)} c_j^{(i)} f_j \right|^2 \right). \quad (\text{A17})
\end{aligned}$$

Clearly, for $\phi_j^{(k)} = \phi_j^{(k)}$ and $\mathbf{n}'_j^{(k)} = \mathbf{n}_j^{(k)}$, $f_j = 1$ and we recover Eq. (A13). To find if there is a higher overlap with the target gate of Eq. (A14), one would have to optimize

over the set $\{\phi_j^{(k)}, \mathbf{n}'_j^{(k)}\}$, which corresponds to the parameters of the single-qubit rotations that act on the target subspace. Such a computation could be potentially performed via gradient-based optimization methods, supplemented by the Jacobian. If a target gate with better overlap is found, then the one-tangles can be reevaluated using the optimized set $\{\phi_j^{(k)}, \mathbf{n}'_j^{(k)}\}$ to obtain the entanglement distribution of the target subsystem.

APPENDIX B: RESONANCE TIMES

For completeness, we present the formula for the coherence function P_x ; this function is used to derive the resonance times. The expressions we present below can

also be found in Ref. [19]. In DD protocols, the electron is initialized in the $|+\rangle$ state; assuming a single nuclear spin, the initial density matrix is given by

$$\rho_0 = |+\rangle\langle +| \otimes |\psi_n\rangle\langle \psi_n|, \quad (\text{B1})$$

where the tensor product is implied between kets and bras. The probability to find the electron in the $|+\rangle$ state after some time t is $P_x = \langle +|\rho(t)|+\rangle$, where $\rho(t) = U\rho_0U^\dagger$ is the time-evolved density matrix of the system. Furthermore, $U = \sigma_{00} \otimes U_0 + \sigma_{11} \otimes U_1$, with $U_j \equiv R_{\mathbf{n}_j}(\phi_j)$. Calculating first $U\rho_0U^\dagger$, we find

$$\begin{aligned} U\rho_0U^\dagger &= \frac{1}{2}(U_0|0\rangle\langle 0| + U_1|1\rangle\langle 1|) \otimes |\psi_n\rangle\langle \psi_n| \\ &= \frac{1}{2}(U_0|0\rangle\langle 0| + U_1|1\rangle\langle 1|) \otimes |\psi_n\rangle\langle \psi_n| \\ &\quad + \frac{1}{2}(U_0|1\rangle\langle 0| + U_1|0\rangle\langle 1|) \otimes |\psi_n\rangle\langle \psi_n|. \end{aligned} \quad (\text{B2})$$

Evaluating $\langle +|U\rho_0U^\dagger|+\rangle$, we obtain

$$\langle +|U\rho_0U^\dagger|+\rangle = \frac{1}{4} \sum_{i,j} U_i |\psi_n\rangle\langle \psi_n| U_j^\dagger. \quad (\text{B3})$$

The probability to find the electron in the $|+\rangle$ state (irrespective of the nuclear spin state) is the trace of Eq. (B3) with respect to the nuclear spin state:

$$\begin{aligned} P_x &= \frac{1}{4} \sum_{i,j} \langle \psi_n| U_i U_j^\dagger |\psi_n\rangle = \frac{1}{2} (1 + \text{Re}\langle \psi_n| U_0^\dagger U_1 |\psi_n\rangle) \\ &= \frac{1}{2} (1 + M). \end{aligned} \quad (\text{B4})$$

Since $U_0^\dagger U_1$ is unitary, it can be written as

$$\begin{pmatrix} a & -b^* \\ b & a^* \end{pmatrix}.$$

(ii) $4-\pi$ sequence:

$$\phi_0 = 2\cos^{-1} \left[g(\omega_0, \omega_1) - 2\sin^2\tilde{\theta} \sin \frac{q_2\omega_1}{2} \sin \frac{q_3\omega_0}{2} \sin \frac{q_4\omega_1}{2} \sin \frac{(q_1 + q_5)\omega_0}{2} \right]. \quad (\text{C2})$$

(iii) $3-\pi$ sequence ($6-\pi$ time-symmetric):

$$\begin{aligned} \phi_0 &= 2\cos^{-1} \left[g(\omega_0, \omega_1) + 4\cos\tilde{\theta}\sin^2\tilde{\theta} \sin(q_1\omega_0) \sin(q_1\omega_1) \sin^2 \frac{q_2\omega_0}{2} \sin^2 \frac{q_2\omega_1}{2} \right. \\ &\quad - 2\sin^2\tilde{\theta} \cos(q_1\omega_1) \sin(q_1\omega_0) \sin(q_2\omega_0) \sin^2 \frac{q_2\omega_1}{2} \\ &\quad \left. - 2\sin^2\tilde{\theta} \sin(q_1\omega_1) \sin(q_2\omega_1) \sin \frac{q_2\omega_0}{2} \sin \left(q_1\omega_0 + \frac{q_2\omega_0}{2} \right) \right], \end{aligned} \quad (\text{C3})$$

Hence, for $\psi_n = [c_1 c_2]^T$ we get

$$\begin{aligned} \text{Re}(a|c_1|^2 - b^*c_1^*c_2 + bc_1c_2^* + a^*|c_2|^2) \\ = \text{Re}(a)(|c_1|^2 + |c_2|^2) + \text{Re}[2i\text{Im}(bc_1c_2^*)] = \text{Re}(a), \end{aligned} \quad (\text{B5})$$

and, therefore, $M = \frac{1}{2}\text{ReTr}(U_0^\dagger U_1) = \frac{1}{2}\text{ReTr}(U_0 U_1^\dagger)$. Finally, by setting $U_j = R_{\mathbf{n}_j}(\phi_j)$, M becomes

$$\begin{aligned} M &= \frac{1}{2}\text{ReTr} \left[\prod_j \left(\cos \frac{\phi_j}{2} + i(-1)^j \sin \frac{\phi_j}{2} \boldsymbol{\sigma} \cdot \mathbf{n}_j \right) \right] \\ &= \cos \frac{\phi_0}{2} \cos \frac{\phi_1}{2} + \mathbf{n}_0 \cdot \mathbf{n}_1 \sin \frac{\phi_0}{2} \sin \frac{\phi_1}{2}. \end{aligned} \quad (\text{B6})$$

In the case of $\phi_0 = \phi_1 \equiv \phi$, M can be rewritten as

$$M = 1 - \sin^2 \frac{\phi}{2} (1 - \mathbf{n}_0 \cdot \mathbf{n}_1). \quad (\text{B7})$$

Using the explicit expression for U_j , one can derive the resonance condition by setting $\mathbf{n}_0 \cdot \mathbf{n}_1 = -1$ in Eq. (B7) for sequences that produce the same nuclear spin rotation angle. For sequences that produce different nuclear spin rotation angles (e.g., UDD₄), one would have to use Eq. (B6).

APPENDIX C: NUCLEAR SPIN ROTATION ANGLES

Here, we provide the expressions for the nuclear spin rotation angles corresponding to $2-\pi$, $3-\pi$, and $4-\pi$ sequences (meaning two, three, or four π pulses in a single sequence unit). The analytical formulas are summarized below.

(i) $2-\pi$ sequence:

$$\phi_0 = 2\cos^{-1}[g(\omega_0, \omega_1)]. \quad (\text{C1})$$

where we define $g(\omega_0, \omega_1)$ as

$$g(\omega_0, \omega_1) = \cos \frac{\sum_{j,\text{odd}} q_j \omega_0}{2} \cos \frac{\sum_{j,\text{even}} q_j \omega_1}{2} - \cos \tilde{\theta} \sin \frac{\sum_{j,\text{odd}} q_j \omega_0}{2} \sin \frac{\sum_{j,\text{even}} q_j \omega_1}{2} \quad (\text{C4})$$

and $\omega_j = t\sqrt{(\omega_L + s_j A)^2 + (s_j B)^2}$; note this is different from the definition in the main text, where we define ω_j as $\omega_j = \sqrt{(\omega_L + s_j A)^2 + (s_j B)^2}$. The ϕ_1 angles are found from ϕ_0 with the replacements $\omega_1 \mapsto \omega_0, \omega_0 \mapsto \omega_1$, and $\tilde{\theta} \mapsto -\tilde{\theta}$. Here, we define $\tilde{\theta} = \theta_0 - \theta_1$, where $\cos \theta_j = (\omega_L + s_j A) / \sqrt{(\omega_L + s_j A)^2 + (s_j B)^2}$.

For example, for the CPMG sequence we have $q_1 t - q_2 t - q_3 t$ with $q_3 = q_1 = q_2/2$. This means that the odd summation in g in Eq. (C4) is $q_1 + q_3$ and the even is q_2 . As we mention in the main text, for the CPMG sequence the rotation angles ϕ_0 and ϕ_1 are equal, but this is not the case for a $2 - \pi$ sequence with arbitrary q_j that do not satisfy $q_1 = q_3 = q_2/2$.

For the UDD_n sequences, the spacings are given by

$$q_s = \sin^2 \left(\frac{\pi s}{2n+2} \right) - \sin^2 \left(\frac{\pi(s-1)}{2n+2} \right), \quad (\text{C5})$$

where s goes from 1 to $n+1$, since there are $n+1$ free evolution periods. The UDD_4 [$q_1 t - q_2 t - q_3 t - q_4 t - q_5 t$ with spacings given by Eq. (C5)] sequence produces rotation angles ϕ_0 and ϕ_1 that are not equal. The UDD sequences (as the CPMG) are symmetric; i.e., in the UDD_4 case, it holds that $q_5 = q_1$, and $q_2 = q_4$.

Regarding the UDD_3 sequence (or any odd- π sequence), it needs to be repeated twice to form the basic unit. Specifically, the initial block with spacings $q_1 t - q_2 t - q_3 t - q_4 t$ becomes a new unit with spacings $q_1 t/2 - q_2 t/2 - q_3 t/2 - (q_4 + q_1)t/2 - q_2 t/2 - q_3 t/2 - q_4 t/2$, where we divide by a factor of 2 to make sure that the sum of all q_j is equal to one and, hence, the time of one unit is t . Again, for UDD_3 it holds that it is symmetric with $q_4 = q_1$ and $q_3 = q_2$. Conversely to the UDD_4 sequence, UDD_3 produces rotation angles that are equal (i.e., $\phi_0 = \phi_1$).

APPENDIX D: UDD_4 JUMPS IN THE DOT PRODUCT

As we mention in Sec. II, the dot product of nuclear spin rotation axes in the case of UDD_4 shows a nontrivial behavior and depends on the number of iterations. We find that these jumps happen near values of N for which $\Delta\phi = |\phi_0 - \phi_1| = 0$. Using the expression for G_1 and substituting $\Delta\phi = 0$ and $\mathbf{n}_0 \cdot \mathbf{n}_1 = 1$, we find that the jumps occur around $N = \text{round}[2\kappa\pi/(\phi_0 + \phi_1)]$, where ϕ_j are the rotation angles in one iteration. We show this behavior in Fig. 11, which captures all the jumps; in these

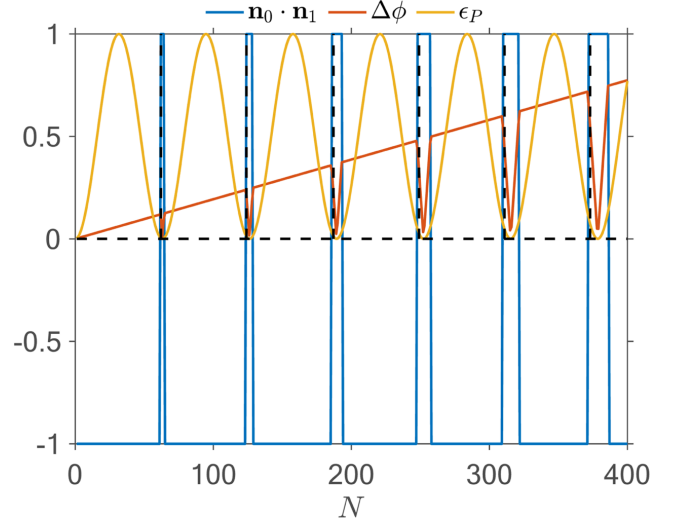


FIG. 11. Jumps in the dot product of nuclear spin rotation axes for UDD_4 as a function of N occur in the ranges when $\Delta\phi \rightarrow 0$; $\Delta\phi$ is defined as $|\phi_0 - \phi_1|$. In these ranges, the entangling power ϵ_P is zero. For this simulation, we set $(\omega_L, A, B) = 2\pi \cdot (314, 60, 30)$ kHz, unit time of $t = 3.1861 \mu\text{s}$, and we consider a spin $S = 1/2$ electron system.

ranges, the nuclear spin evolves trivially, i.e., independent of the electron's state.

APPENDIX E: MINIMIZATION OF ONE-TANGLE FOR $S=1$ DEFECT ELECTRON SPIN

In this section, we consider a target nuclear spin with hyperfine (HF) parameters $(A, B) = 2\pi \cdot (60, 30)$ kHz and Larmor frequency $\omega_L = 2\pi \cdot 314$ kHz as in Sec. III B. However, in this case, we assume a defect electron system $S = 1$, and we define the qubit using the spin projections $s_0 = 0$ and $s_1 = -1$. As in Sec. III B, we choose the CPMG sequence. First, we consider the $k = 1$ resonance of the target spin; i.e., we set the basic unit time to be $t = 3.5102 \mu\text{s}$ and set the number of iterations to be $N = 20$, which gives rise to maximum one-tangle of the target spin. In Fig. 12(a), we plot the one-tangle of an unwanted nuclear spin whose HF parameters could lie in the range $\in 2\pi \cdot [10, 200]$ kHz. We further indicate with circles the HF parameters of an unwanted spin, which satisfies approximately the condition for trivial evolution, presented in Sec. II B. To display these points, we set a bound for the unwanted one-tangle to be $\epsilon_{12|3} < 0.02$ and a tolerance for satisfying the trivial evolution of 1.3×10^{-2} . We see that indeed the minimal one-tangles correspond to nuclei that approximately evolve trivially.

In Fig. 12(b), we minimize the unwanted one-tangle by searching over the first five resonances of the target spin and iterations of the basic unit that preserve maximum entanglement between the target register and the electron. The optimal repetitions of the basic CPMG unit, as well as

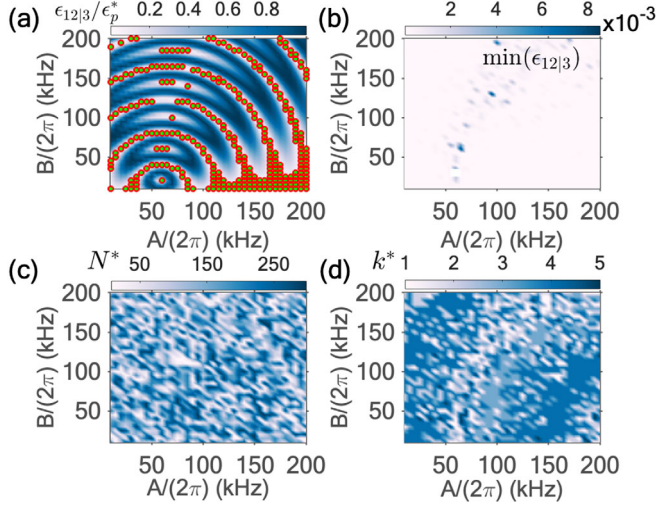


FIG. 12. Controlling a target spin with parameters $(A, B, \omega_L) = 2\pi \cdot (60, 30, 314)$ kHz in the presence of an unwanted spin with varying HF parameters $\in 2\pi \cdot [10, 200]$ kHz. (a) One-tangle of the unwanted spin, scaled by the maximum bound of $\epsilon_p^* = 2/9$. The time of the unit is the first resonance time of the target spin, and the number of iterations is $N = 20$, which maximize its one-tangle. (b) Minimization of the one-tangle of the unwanted spin using the first five ($k = 1, \dots, 5$) resonances of the target spin and up to 300 pulses on the electron. Optimal number of repetitions (c) and optimal resonance (d) to minimize the unwanted spin's one-tangle while keeping the one-tangle of the target spin maximal. In all plots, we consider the CPMG sequence and an electron spin $S = 1$ ($s_0 = 0$ and $s_1 = -1$).

the optimal resonances, are shown in Figs. 12(c) and 12(d), respectively.

APPENDIX F: SELECTIVITY AS A FUNCTION OF $|\Delta A|$

Here, we consider the problem of addressing a single nuclear spin with parameters $(A, B, \omega_L) = 2\pi \cdot (60, 30, 314)$ kHz, in the presence of an unwanted spin (with the same Larmor frequency), when the A HF parameter of the latter differs from the target one by $|\Delta A|$. For the unwanted spin, we let its A HF value be in the range $2\pi \cdot [10, 200]$ kHz, and we sample it with steps of 0.25 kHz. For the B value of the unwanted spin, we fix some constant value as we mention shortly. To illustrate the procedure of isolating the target spin, we use as an example the CPMG sequence. To entangle the electron with the target nuclear spin, we search over its first 12 resonances ($k \in [1, 12]$). We find the number of iterations that maximize the target one-tangle by using the minima of G_1 . For each value of $|\Delta A|$, we keep the optimal unit time and iteration of the unit that give rise to minimal unwanted one-tangle and respect the gate time restriction of 2 ms.

We consider two cases. In the first one, we assume an electron with spin $S = 1$, and we select the spin projections $s_0 = 0$ and $s_1 = -1$. In the second case, we consider

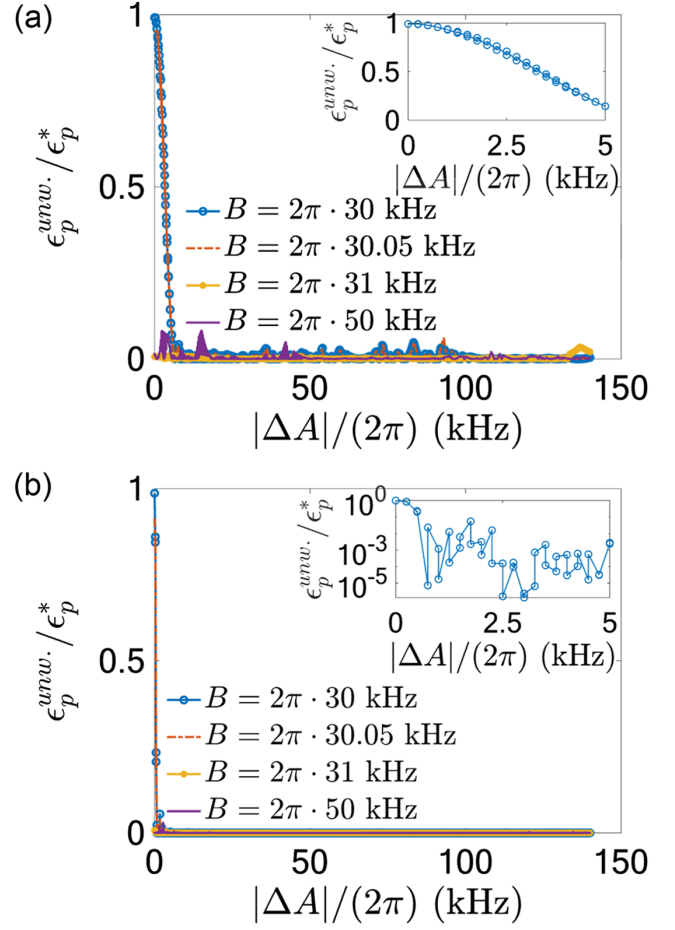


FIG. 13. (a) Unwanted one-tangle (scaled by the maximum value $\epsilon_p^* = 2/9$) for a nuclear spin whose A HF parameter differs by $|\Delta A|$ from the target spin. For the target spin, we consider $(A, B) = 2\pi \cdot (60, 30)$ kHz. The electron is considered to be $S = 1/2$ with electron spin projections $s_0 = 1/2 = -s_1$. The different colors correspond to different B values for the unwanted spin. The inset shows the unwanted one-tangle in the range $|\Delta A|/(2\pi) \in [0, 5]$ kHz, for the case where the unwanted spin has the same B value with the target one. (b) Similar as (a), but for an electron spin $S = 1$, with $s_0 = 0$ and $s_1 = -1$. In both plots, the nuclear Larmor frequency is set to $\omega_L = 2\pi \cdot 314$ kHz.

an electron spin $S = 1/2$ and define the projections $s_0 = 1/2 = -s_1$. The unwanted one-tangle as a function of $|\Delta A|$ is shown in Fig. 13(a) for $S = 1$ and in Fig. 13(b) for $S = 1/2$. The different lines correspond to various B values for the unwanted spin. The blue line corresponds to the case when the unwanted and target spins have the same B value. This case is also illustrated in the insets in Fig. 13. We note that, when the B values of the two spins are the same, there is a more gradual reduction of the unwanted one-tangle as a function of $|\Delta A|$ for $S = 1/2$ than for $S = 1$. This is due to the fact that for $A, B \ll \omega_L$ the resonance time becomes inversely proportional to $\tilde{\omega} \approx 2\omega_L + A(s_0 + s_1) + (s_0^2 + s_1^2)B^2/(2\omega_L)$, and so the linear dependence in A vanishes for $S = 1/2$. Although the dependence of the resonance time on B is quadratic, we

note that even a difference of 1 kHz between the B values of target and unwanted spins suffices to ensure selectivity of the former [see the yellow line in Fig. 13(b)].

APPENDIX G: MINIMA OF G_1 FOR $\mathbf{n}_0 \cdot \mathbf{n}_1 \leq 0$

In this section, we provide the number of iterations that maximize the one-tangle of a nuclear spin, as long as $\mathbf{n}_0 \cdot \mathbf{n}_1 \leq 0$. Let us first consider the CPMG or UDD₃ sequences. For these sequences, it holds that $\phi_0 = \phi_1$ and G_1 of Eq. (6) simplifies into

$$G_1(N) = \{\cos^2[\phi_0(N)/2] + \mathbf{n}_0 \cdot \mathbf{n}_1 \sin^2[\phi_0(N)/2]\}^2. \quad (\text{G1})$$

Requiring that $G_1(N) = 0$, we find

$$\begin{aligned} \cos^2 \frac{N\phi_0}{2} + \mathbf{n}_0 \cdot \mathbf{n}_1 \sin^2 \frac{N\phi_0}{2} = 0 &\Rightarrow \\ \frac{-1}{\mathbf{n}_0 \cdot \mathbf{n}_1} = \tan^2 \frac{N\phi_0}{2} &\Rightarrow \\ N = \text{round} \left[\frac{1}{\phi_0} \left(2\kappa\pi - 2\tan^{-1} \sqrt{\frac{-1}{\mathbf{n}_0 \cdot \mathbf{n}_1}} \right) \right], \\ N = \text{round} \left[\frac{1}{\phi_0} \left((2\kappa - 1)\pi + 2\tan^{-1} \sqrt{\frac{-1}{\mathbf{n}_0 \cdot \mathbf{n}_1}} \right) \right], \end{aligned} \quad (\text{G2})$$

where ϕ_0 is the rotation angle in one unit. The two expressions hold as long as $\mathbf{n}_0 \cdot \mathbf{n}_1 < 0$ and $\phi_0(N) \neq (2\kappa + 1)\pi$. For $\mathbf{n}_0 \cdot \mathbf{n}_1 \approx 0$, $G_1 = 0$ when $\phi_0(N) = (2\kappa + 1)\pi$, and, hence, $N = \text{round}[(2\kappa + 1)\pi/\phi_0]$. For $\mathbf{n}_0 \cdot \mathbf{n}_1 > 0$, G_1 cannot go to zero. Regarding the UDD₄ sequence for which it holds that $\phi_0 \neq \phi_1$, we cannot estimate analytically the repetitions N ; some values are captured by the above expressions with the replacement $\phi_0 \mapsto \phi_0 + \phi_1$, but due to the complicated oscillations of G_1 these modified expressions for N do not hold in all cases.

APPENDIX H: COMPARISON OF CPMG, UDD₃, AND UDD₄ ROTATION ANGLES

To understand geometrically the rotation angle induced by each sequence, we use the Rodrigues formula [67] for the composition of rotations. Two rotations of the form $R_1(\alpha)R_m(\beta)$ give rise to the total rotation $R_n(\gamma)$ for which the rotation angle is given by

$$\cos \frac{\gamma}{2} = \cos \frac{\alpha}{2} \cos \frac{\beta}{2} - \sin \frac{\alpha}{2} \sin \frac{\beta}{2} (\mathbf{l} \cdot \mathbf{m}), \quad (\text{H1})$$

while the rotation axis is given by

$$\sin \frac{\gamma}{2} \mathbf{n} = \sin \frac{\alpha}{2} \cos \frac{\beta}{2} \mathbf{l} + \cos \frac{\alpha}{2} \sin \frac{\beta}{2} \mathbf{m} + \sin \frac{\alpha}{2} \sin \frac{\beta}{2} (\mathbf{l} \times \mathbf{m}). \quad (\text{H2})$$

We apply this composition law repeatedly to find the induced nuclear spin rotation after each free-evolution period of the sequence passes. For the CPMG sequence, there are two compositions and three free-evolution periods; UDD₄ has four compositions and five free-evolution periods; and UDD₃ has six compositions and seven free-evolution periods. UDD₃ has more free-evolution periods than UDD₄ because we repeat the basic unit twice to yield a new sequence unit. In this way, we ensure that the electron returns to its initial state, since the new basic block of the sequence has an even number of π pulses.

Without loss of generality, we consider an electron spin $S = 1$, with $s_0 = 0$ and $s_1 = -1$, and assume that the electron starts from the $|0\rangle$ state (similar analysis holds when the electron starts in $|1\rangle$) and is flipped repeatedly according to the number of π pulses in the CPMG or UDD units.

In Fig. 14, we show the rotation axes of a single nuclear spin $[(\omega_L, A, B) = 2\pi \cdot (314, 120, 90)$ kHz and $t = 3.7889$ μ s] after each composition. In each free-evolution period, the nuclear spin rotates alternately about axis “A” and “B.” For example, in Fig. 14(a), the nuclear spin first rotates about “A,” then about “B,” and again about “A.” The composition of “A” and “B” gives rise to the new axis

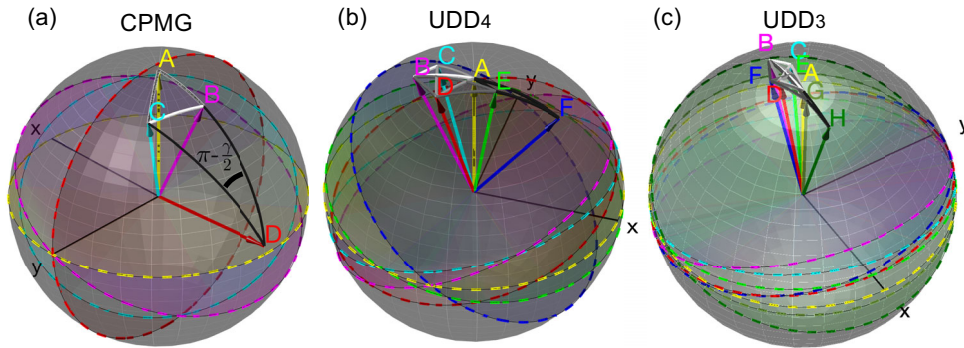


FIG. 14. Comparison of CPMG (a) with UDD₄ (b) and UDD₃ (c) rotation angles. We compose the rotations of the free-evolution periods for one unit of the sequence using the Rodrigues formula. The last composition gives rise to the black spherical triangles. In (a), we show $\triangle CDB$, which gives the total rotation angle γ . We find that geometrically the rotation angle of CPMG is larger.

“C,” and the composition of “C” with “A” leads to the final axis “D.” The angle enclosed by the arcs CD and BD gives the total rotation angle γ in one CPMG unit. Similar analysis holds for Figs. 14(b) and 14(c), where rotations follow the composition $[A][B][A][B][A]$ and $[A][B][A][B][A][B][A]$, respectively. We notice that it holds that $\pi - (\gamma/2)^{\text{CPMG}} > \pi - (\gamma/2)^{\text{UDD}_4} > \pi - (\gamma/2)^{\text{UDD}_3}$, and so one would conclude that $\gamma^{\text{CPMG}} < \gamma^{\text{UDD}_4} < \gamma^{\text{UDD}_3}$. However, these rotation angles are close to 2π , and, hence, we need to consider as actual rotation $\tilde{\gamma} = 2\pi - \gamma$. Therefore, we find that it holds that

$$\tilde{\gamma}^{\text{CPMG}} > \tilde{\gamma}^{\text{UDD}_4} > \tilde{\gamma}^{\text{UDD}_3}. \quad (\text{H3})$$

Thus, UDD_3 produces the finest rotation angle of all three sequences, which can offer greater precision, but CPMG is the fastest of all.

APPENDIX I: ADDITIONAL RESONANCE TIMES FOR UDD_n FOR EVEN n

In the main text, we mention that for UDD_3 and CPMG we find only the resonance times $t_k = 4\pi(2k-1)/\tilde{\omega}$, where $\tilde{\omega} = \omega_0 + \omega_1$, with $\omega_j = \sqrt{(\omega_L + s_j A)^2 + (s_j B)^2}$. For UDD_4 , we find the additional resonance times $t_k = 8\pi(2k-1)/\tilde{\omega}$. The odd UDD_n sequences are time symmetric with respect to the middle pulse (before repeating them twice), whereas the even UDD_n sequences are time symmetric with respect to the middle free-evolution period. This implies that the odd UDD_n sequences are expected to produce the same rotation angles on the nuclear spin, i.e., $\phi_0 = \phi_1$. One way to see this is to consider as an example the evolution operator of UDD_3 in one unit:

$$U = \sigma_{00} \otimes e^{-iH_0(q_1 t/2)} e^{-iH_1(q_2 t/2)} e^{-iH_0(q_2 t/2)} e^{-iH_1 q_1 t} e^{-iH_0(q_2 t/2)} e^{-iH_1(q_2 t/2)} e^{-iH_0(q_1 t/2)} \\ + \sigma_{11} \otimes e^{-iH_1(q_1 t/2)} e^{-iH_0(q_2 t/2)} e^{-iH_1(q_2 t/2)} e^{-iH_0 q_1 t} e^{-iH_1(q_2 t/2)} e^{-iH_0(q_2 t/2)} e^{-iH_1(q_1 t/2)}. \quad (\text{I1})$$

Thus, we see that the rotation angle ϕ_0 is

$$2\phi_0 = \text{Tr}[e^{-iH_0(q_1 t/2)} e^{-iH_1(q_2 t/2)} e^{-iH_0(q_2 t/2)} e^{-iH_1 q_1 t} e^{-iH_0(q_2 t/2)} e^{-iH_1(q_2 t/2)} e^{-iH_0(q_1 t/2)}] \\ = \text{Tr}[e^{-iH_1(q_2 t/2)} e^{-iH_0(q_2 t/2)} e^{-iH_1 q_1 t} e^{-iH_0(q_2 t/2)} e^{-iH_1(q_2 t/2)} e^{-iH_0 q_1 t}], \quad (\text{I2})$$

where in the second line we use the cyclic permutation property of the trace. Similarly, for the rotation angle ϕ_1 we obtain

$$2\phi_1 = \text{Tr}[e^{-iH_1(q_1 t/2)} e^{-iH_0(q_2 t/2)} e^{-iH_1(q_2 t/2)} e^{-iH_0 q_1 t} e^{-iH_1(q_2 t/2)} e^{-iH_0(q_2 t/2)} e^{-iH_1(q_1 t/2)}] \\ = \text{Tr}[e^{-iH_0(q_2 t/2)} e^{-iH_1(q_2 t/2)} e^{-iH_0 q_1 t} e^{-iH_1(q_2 t/2)} e^{-iH_0(q_2 t/2)} e^{-iH_1 q_1 t}] \\ = \text{Tr}[e^{-iH_1(q_2 t/2)} e^{-iH_0 q_1 t} e^{-iH_1(q_2 t/2)} e^{-iH_0(q_2 t/2)} e^{-iH_1 q_1 t} e^{-iH_0(q_2 t/2)}] \\ = \text{Tr}[e^{-iH_0 q_1 t} e^{-iH_1(q_2 t/2)} e^{-iH_0(q_2 t/2)} e^{-iH_1 q_1 t} e^{-iH_0(q_2 t/2)} e^{-iH_1(q_2 t/2)}] \\ = \text{Tr}[e^{-iH_1(q_2 t/2)} e^{-iH_0(q_2 t/2)} e^{-iH_1 q_1 t} e^{-iH_0(q_2 t/2)} e^{-iH_1(q_2 t/2)} e^{-iH_0 q_1 t}] = 2\phi_0, \quad (\text{I3})$$

where we repeatedly use the cyclic permutation property of the trace. Similarly, it can be proven that, for odd UDD_n sequences with $n > 3$, it also holds that $\phi_0 = \phi_1$. For this reason, the odd UDD_n sequences do not produce additional resonance times besides $t_k = 4\pi(2k-1)/\tilde{\omega}$.

On the other hand, the UDD_n sequences with even $n \geq 4$ produce rotation angles $\phi_0 \neq \phi_1$, which gives an extra degree of freedom based on which electron-nuclear entanglement can be generated for unit times besides the main one at $t_k = 4\pi(2k-1)/\tilde{\omega}$. Besides the times $t_k = 4\pi(2k-1)/\tilde{\omega}$ and $t_k = 8\pi(2k-1)/\tilde{\omega}$ we mention in the main text for UDD_4 , we find as an example that there exist additional resonances at times

$$t_k = 10\pi \frac{2k-1}{\tilde{\omega}}, \\ t_k = 16\pi \frac{2k-1}{\tilde{\omega}}, \\ t_k = 18\pi \frac{2k-1}{\tilde{\omega}}, \\ t_k = 22\pi \frac{2k-1}{\tilde{\omega}}. \quad (\text{I4})$$

Figure 15(a) shows the dot product of the nuclear rotation axes as a function of time of one UDD_4 unit. For this plot, we consider an electron with spin $S = 1/2$

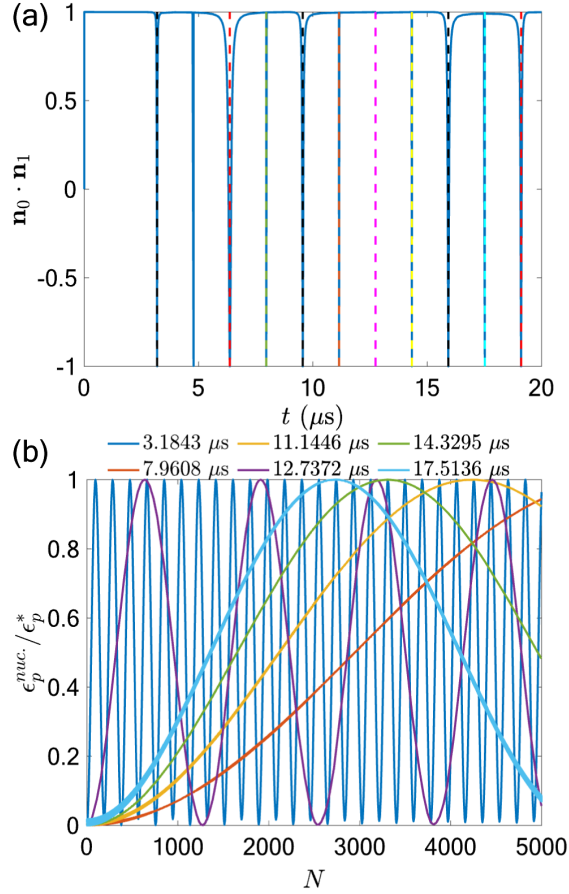


FIG. 15. (a) Dot product of nuclear axes as a function of the time of one UDD_4 sequence unit. (b) Nuclear one-tangle scaled by $\epsilon_p^* = 2/9$, for various resonance times, as a function of the iterations of one unit. All times besides the first one at $3.1843 \mu\text{s}$ correspond to the additional times we list in Eq. (I4). For these resonance times, a very large number of iterations is required to reach the first maximum of the nuclear one-tangle. The curves which look as though they have larger linewidth are, in fact, highly oscillatory as a function of N .

(i.e., spin projections $s_0 = -s_1 = 1/2$) and a nuclear spin with parameters $(A, B, \omega_L) = 2\pi \cdot (70, 10, 314)$ kHz. The black vertical lines correspond to the resonance times $t_k = 4\pi(2k-1)/\tilde{\omega}$, whereas the red vertical lines to the times $t_k = 8\pi(2k-1)/\tilde{\omega}$. Additionally, the green line corresponds to the time $t_k = 10\pi(2k-1)/\tilde{\omega}$, the magenta line to $t_k = 16\pi(2k-1)/\tilde{\omega}$, the yellow line to $t_k = 18\pi(2k-1)/\tilde{\omega}$, and the cyan line to $t_k = 22\pi(2k-1)/\tilde{\omega}$. These resonances are extremely sharp and appear when we sample the time with very fine steps. For example, to demonstrate these lines, we consider 10^6 evenly spaced time values in the range $[0, 20] \mu\text{s}$. If we generate a much smaller number of evenly spaced time values (around 10^3), we mainly observe the resonances indicated by the black and red lines, since these resonances are more broad.

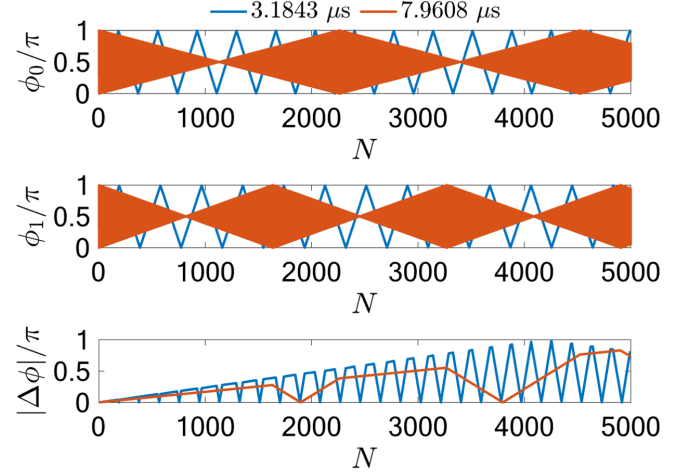


FIG. 16. Nuclear rotation angles ϕ_0 (top) and ϕ_1 (middle) as a function of iterations of a UDD_4 unit at the resonance time $3.1843 \mu\text{s}$ or at $7.9608 \mu\text{s}$. The red lines show the fast oscillation of the rotation angles. The bottom plot shows the difference of the rotation angles as a function of N .

Figure 15(b) shows the nuclear one-tangle as a function of the number of iterations N , of one UDD_4 unit, and for various resonance times associated with the differently colored lines. The first time of $3.1843 \mu\text{s}$ is obtained from $t_k = 4\pi(2k-1)/\tilde{\omega}$, for $k=1$. All other indicated times in the plot correspond to the additional resonance times we list in Eq. (I4). For the time of $3.1843 \mu\text{s}$, entanglement builds up much faster compared to the remaining cases. This is because the additional resonance times are “weaker,” in the sense that the rotation angles per iteration are highly oscillatory, resulting potentially in the averaging out of interactions. This behavior is demonstrated in Fig. 16, where we plot with red lines the rotation angles ϕ_0 and ϕ_1 , as well as their difference $|\Delta\phi|$ as a function of N , for a unit time equal to $t = 7.9608 \mu\text{s}$. To the contrary, for the resonance at $t = 3.1843 \mu\text{s}$, we do not observe such rapid oscillations for the rotation angles, which is potentially the reason why entanglement builds up faster for this case based on Fig. 15(b). Therefore, we conclude that, for any practical application, the weaker resonance times cannot be used to create entanglement fast enough, meaning that dephasing deteriorates the electron-nuclear Bell state before it is even created. Furthermore, since those resonances are extremely sharp and require very precise tuning of the interpulse spacings, it is highly unlikely that one would observe experimentally such resonances.

APPENDIX J: DERIVATION OF ONE-TANGLES FOR THE ELECTRON AND A NUCLEAR SPIN

In this section, we prove that the expression of the nuclear spin one-tangle essentially reduces to the formula of the two-qubit entangling power. We start from the general expression for an arbitrary number n of qubits (with $n-1$ nuclear spins):

$$\begin{aligned}
\epsilon_{p|q}^{\text{nuclear}} &= 1 - \prod_i \frac{d_i}{d_i + 1} \left\{ 1 + \frac{1}{2^n} + \frac{n}{2^{n-1}} + \sum_{k=1}^{n-1} \frac{2^{k-1}}{2^{n-1}} \binom{n-2}{k-1} (1 + G_1) + \sum_{k=1, n>3}^{n-3} \frac{2^k}{2^{n-1}} \left[\binom{n-2}{k} + \binom{n-1}{k+1} \right] \right\} \\
&= 1 - \frac{2^n}{3^n} \left\{ 1 + \frac{1}{2^n} + \frac{n}{2^{n-1}} + \frac{1}{2^{n-1}} \frac{1}{3^{-n+2}} (1 + G_1) + \Theta(n-3) \frac{1}{2^n 3^2} [5 \cdot 3^n - 3^2(1 + 2n + 2^n)] \right\} \\
&= 1 - \frac{2}{9} (1 + G_1) - \frac{2^n}{3^n} \left\{ \frac{1 + 2n + 2^n}{2^n} + \Theta(n-3) \frac{1}{2^n} [5 \cdot 3^{n-2} - (1 + 2n + 2^n)] \right\} \\
&= 1 - \frac{2}{9} (1 + G_1) - \frac{1}{3^n} \{ 1 + 2n + 2^n + \Theta(n-3) [5 \cdot 3^{n-2} - (1 + 2n + 2^n)] \}, \tag{J1}
\end{aligned}$$

where $\Theta(n-3)$ is the step function. Clearly, for $n=3$ the last term vanishes, and we recover $2/9(1-G_1)$. For $n > 3$, we have

$$\epsilon_{p|q}^{\text{nuclear}} = \frac{7}{9} - \frac{2}{9} G_1 - \frac{5 \cdot 3^{n-2}}{3^n} = \frac{7-5}{9} - \frac{2}{9} G_1 = \frac{2}{9} (1 - G_1), \tag{J2}$$

which concludes our proof.

For the electron, we start from the expression

$$\begin{aligned}
\epsilon_{p|q}^{\text{electron}} &= 1 - \frac{2^n}{3^n} \left\{ \frac{1}{2} + \frac{1}{2^n} + \frac{n}{2^{n-1}} + \sum_{k=1}^{n-3} \frac{2^k}{2^{n-1}} \binom{n-1}{k+1} + \left[\frac{1}{2^{n-1}} \sum_{j=1}^{n-1} (1 + G_1^{(j)}) + \frac{1}{2^{n-2}} \sum_{\substack{j_1, j_2 \\ j_2 > j_1}} (1 + G_1^{(j_1)} G_1^{(j_2)}) + \dots \right. \right. \\
&\quad \left. \left. + \frac{1}{2^{n-(n-2)}} \sum_{j_1, \dots, j_{n-2}} \left(1 + \prod_{i=1}^{n-2} G_1^{(j_i)} \right) + \frac{1}{2^{n-(n-1)}} \left(1 + \prod_{i=1}^{n-1} G_1^{(j_i)} \right) \right] \right\}, \tag{J3}
\end{aligned}$$

which can be simplified into

$$\begin{aligned}
\epsilon_{p|q}^{\text{electron}} &= 1 - \frac{1}{3^n} \left\{ 2^{n-1} + 1 + 2n + \Theta(n-3)(1 - 2n - 2^{n-1} + 3^{n-1}) + \left(\sum_{k=1}^{n-1} 2^k \sum_{\substack{j_1, \dots, j_k \\ j_{m+1} > j_m}} 1 \right) + F(G_1) \right\} \\
&= 1 - \frac{1}{3^n} \left\{ 2^{n-1} + 1 + 2n + \Theta(n-3)(1 - 2n - 2^{n-1} + 3^{n-1}) + \sum_{k=1}^{n-1} 2^k \binom{n-1}{k} + F(G_1) \right\} \\
&= 1 - \frac{1}{3^n} \left\{ 2^{n-1} + 1 + 2n + \Theta(n-3)(1 - 2n - 2^{n-1} + 3^{n-1}) + \frac{1}{3}(-3 + 3^n) + F(G_1) \right\}, \tag{J4}
\end{aligned}$$

where we define $F(G_1)$ as

$$F(G_1) = \sum_{k=1}^{n-1} 2^k \sum_{j_1, \dots, j_k} \prod_{i=1}^k G_1^{(j_i)}. \tag{J5}$$

We note that $F(G_1)$ can be rewritten as

$$\begin{aligned}
F(G_1) &= 2 \left\{ \left(G_1^{(1)} + \dots + G_1^{(n-1)} \right) + 2 \left(G_1^{(1)} G_1^{(2)} + G_1^{(1)} G_1^{(3)} + \dots + G_1^{(1)} G_1^{(n-1)} + \dots + G_1^{(n-2)} G_1^{(n-1)} \right) \right. \\
&\quad \left. + 2^2 \left(G_1^{(1)} G_1^{(2)} G_1^{(3)} + G_1^{(1)} G_1^{(2)} G_1^{(4)} + \dots + G_1^{(1)} G_1^{(2)} G_1^{(n-1)} + \dots \right) + \dots \right\}, \tag{J6}
\end{aligned}$$

which actually reduces to

$$-1 + (1 + 2G_1^{(1)}) \dots (1 + 2G_1^{(n-1)}) = -1 + \prod_{i=1}^{n-1} (1 + 2G_1^{(i)}). \tag{J7}$$

Finally, the electron's one-tangle reads

$$\epsilon_{p|q}^{\text{electron}} = 1 - \frac{1}{3^n} \left\{ -1 + 2n + 2^{n-1} + 3^{n-1} + \Theta(n-3)(1 - 2n - 2^{n-1} + 3^{n-1}) + \prod_{i=1}^{n-1} (1 + 2G_1^{(i)}) \right\}. \quad (\text{J8})$$

For $n > 3$, it becomes

$$\begin{aligned} \epsilon_{p|q}^{\text{electron}} &= 1 - \frac{1}{3^n} \left\{ 2 \cdot 3^{n-1} + \prod_{i=1}^{n-1} (1 + 2G_1^{(i)}) \right\} \\ &= \frac{1}{3} - \frac{1}{3^n} \prod_{i=1}^{n-1} (1 + 2G_1^{(i)}), \end{aligned} \quad (\text{J9})$$

whereas for $n = 3$ the term multiplying the $\Theta(n-3)$ function vanishes and we obtain

$$\begin{aligned} \epsilon_{p|q}^{\text{electron}} &= 1 - \frac{18}{9 \cdot 3} - \frac{1}{3^n} \prod_{i=1}^{n-1} (1 + 2G_1^{(i)}) \\ &= \frac{1}{3} - \frac{1}{3^n} \prod_{i=1}^{n-1} (1 + 2G_1^{(i)}). \end{aligned} \quad (\text{J10})$$

APPENDIX K: PARAMETERS OF THE MULTIPARTITE GATES

1. Random generation of nuclei

In Tables II–IV, we list the HF parameters of the randomly generate nuclei (labeled by number) we use in Sec. IV A. We present their one-tangles, rotation angles, dot product of rotation axes, and positions compared to the vacancy site. To estimate the distances and polar angles of nuclei, we use the approach found in Supplemental Material of Refs. [36,68] and in Ref. [61]. Since we are studying weakly coupled spins far away from the electron, the interaction is well approximated by the dipole-dipole interaction, and the Fermi contact interaction is negligible. The hyperfine vector can be broken into parallel and perpendicular components which are related to the polar angle θ and the distance R by

$$B = 3A_0 \cos \theta \sin \theta, \quad (\text{K1})$$

$$A = A_0(3 \cos^2 \theta - 1), \quad (\text{K2})$$

TABLE II. Parameters for the $k = 1$ CPMG resonances in Figs. 6(a) and 6(b) and the $k = 2$ CPMG in Figs. 6(c) and 6(d).

$k = 1$							
No.	$\frac{A}{2\pi}$ (kHz)	$\frac{B}{2\pi}$ (kHz)	$\epsilon_{p q}/\epsilon_p^*$	$\phi_0/(\pi/2)$	$\mathbf{n}_0 \cdot \mathbf{n}_1$	$R^{13\text{C}}$ (Å)	$\theta^{13\text{C}}$ (deg)
1	195.78	49.619	0.9986	0.97615	-1	5.798	9.4595
2	27.783	136.51	0.99906	1.0206	-0.99667	6.0056	48.7804
3	124.53	128.31	0.95585	0.86597	-0.99715	5.8549	29.8479
4	100.03	22.072	0.99978	0.99104	-0.99812	7.2761	8.2809
5	26.926	181.33	0.96884	1.1155	-0.99328	5.4466	50.4027
6	65.726	128.15	0.99849	1.0257	-0.99718	6.1206	40.0504
7	63.767	74.919	0.99849	1.0257	-0.99718	7.1056	32.1510
8	106.88	164.74	0.96352	1.1244	-0.99462	5.5762	36.6319
9	193.4	122.07	0.97393	0.89743	-0.99748	5.4859	21.2539
10	144.18	93.415	0.99612	0.96065	-0.99893	6.0305	21.6910
$k = 2$							
No.	$\frac{A}{2\pi}$ (kHz)	$\frac{B}{2\pi}$ (kHz)	$\epsilon_{p q}/\epsilon_p^*$	$\phi_0/(\pi/2)$	$\mathbf{n}_0 \cdot \mathbf{n}_1$	$R^{13\text{C}}$ Å	$\theta^{13\text{C}}$ (deg)
1	188.85	131.4	0.99822	1.0268	-1	5.4598	22.9024
2	56.381	179.7	0.95301	1.4246	-0.50348	5.4953	45.5628
3	88.294	109.64	0.98979	0.94983	-0.95158	6.2905	33.1012
4	56.527	78.511	0.98742	1.1009	-0.5337	7.0931	34.9707
5	134.8	150.66	0.99807	1.1201	-0.75814	5.6010	31.2819
6	82.906	187.71	0.99703	1.2709	-0.33844	5.4062	41.9618
7	121.1	73.468	0.99934	1.6293	-0.11789	6.4427	20.6001
8	10.288	157.82	0.99436	1.024	-0.78257	5.6665	52.8493

TABLE III. Parameters for the $k = 1$ UDD₃ resonance in Figs. 6(e) and 6(f) and the $k = 3$ UDD₃ resonance in Figs. 6(g) and 6(h).

$k = 1$							
No.	$\frac{A}{2\pi}$ (kHz)	$\frac{B}{2\pi}$ (kHz)	$\epsilon_{p q}/\epsilon_p^*$	$\phi_0/(\pi/2)$	$\mathbf{n}_0 \cdot \mathbf{n}_1$	$R^{13\text{C}}$ (Å)	$\theta^{13\text{C}}$ (deg)
1	156.64	77.034	1	0.998 88	-1	6.0380	17.3233
2	140.3	86.029	0.999 78	1.0098	-0.9988	6.1266	20.7752
3	198.87	166.64	0.999 37	1.0055	-0.933 07	5.2130	26.1614
4	66.029	49.357	0.999 92	1.0119	-0.980 71	7.6696	24.1452
5	70.082	148.45	1	1.0151	-0.9537	5.8393	41.1360
6	123.25	121.93	0.999 91	1.013	-0.978 65	5.9252	29.1248
7	26.135	112.96	0.9988	1.0269	-0.985 38	6.4041	47.9618
8	41.644	103.96	0.999 22	0.984 95	-0.991 14	6.5907	43.0975
9	159.78	104.28	0.999 25	0.985 41	-0.991 01	5.8221	21.8136
10	61.719	76.878	0.999 75	1.01	-1	7.0826	33.1540
11	45.081	191.59	0.999 99	1.0355	-0.900 59	5.3707	47.8464
$k = 3$							
No.	$\frac{A}{2\pi}$ (kHz)	$\frac{B}{2\pi}$ (kHz)	$\epsilon_{p q}/\epsilon_p^*$	$\phi_0/(\pi/2)$	$\mathbf{n}_0 \cdot \mathbf{n}_1$	$R^{13\text{C}}$ (Å)	$\theta^{13\text{C}}$ (deg)
1	168.78	12.804	0.999 37	1.016	-1	6.1687	2.8916
2	82.989	158.3	0.999 68	1.4125	-0.224 76	5.7008	39.7526
3	63.816	88.135	0.996 38	1.4196	-0.314 99	6.8222	34.8782
4	136.9	149.52	0.959 87	1.5528	-0.361 49	5.6013	30.8775
5	141.46	99.44	0.969 69	1.0693	-0.489 89	6.0031	23.0786
6	142.11	76.191	0.999 61	1.1399	-0.609 42	6.1886	18.6298
7	186.1	56.749	0.993 09	0.99304	-0.854 08	5.8622	11.2690
8	199.65	138.43	0.996 34	1.0949	-0.636 09	5.3621	22.8424

TABLE IV. Parameters for the $k = 1$ UDD₄ resonance in Figs. 6(i) and 6(j) and the $k = 2$ UDD₄ resonance in Figs. 6(k) and 6(l).

$k = 1$								
No.	$\frac{A}{2\pi}$ (kHz)	$\frac{B}{2\pi}$ (kHz)	$\epsilon_{p q}/\epsilon_p^*$	$\phi_0/(\pi/2)$	$\phi_1/(\pi/2)$	$\mathbf{n}_0 \cdot \mathbf{n}_1$	$R^{13\text{C}}$ (Å)	$\theta^{13\text{C}}$ (deg)
1	185.97	180.32	0.997 26	0.0082	1.9251	-1	5.1871	28.7667
2	66.715	101.62	0.992 31	0.444 77	1.5634	-0.707 96	6.5463	36.4471
3	74.691	53.908	0.999 97	1.6433	1.8615	-0.037 267	7.3993	23.5345
4	142.18	92.353	0.999 95	1.96	0.051 616	-0.605 99	6.0567	21.7336
5	129.3	56.393	0.999 98	1.0714	1.9898	-0.013 046	6.4964	15.6109
6	176.75	56.919	0.993 06	0.847 82	1.8841	0.019 231	5.9511	11.8573
7	53.599	136.86	0.955 39	0.504 12	1.8016	-0.930 27	6.0146	43.3476
8	22.803	92.34	0.995 26	1.2626	0.925 51	-0.611 59	6.8526	47.5050
9	36.541	194.7	0.997 41	1.6852	0.382 14	-0.993 22	5.3311	49.2472
$k = 2$								
No.	$\frac{A}{2\pi}$ (kHz)	$\frac{B}{2\pi}$ (kHz)	$\epsilon_{p q}/\epsilon_p^*$	$\phi_0/(\pi/2)$	$\phi_1/(\pi/2)$	$\mathbf{n}_0 \cdot \mathbf{n}_1$	$R^{13\text{C}}$ (Å)	$\theta^{13\text{C}}$ (deg)
1	57.301	157.25	0.999 83	1.6338	0.349 39	-1	5.7448	44.115
2	83.42	41.407	0.987 32	0.339 54	1.5977	-0.747 18	7.4432	17.4606
3	91.972	183.32	0.994 33	1.4705	0.645 75	-0.964 29	5.4352	40.3454
4	167.87	70.649	0.991 08	1.1752	1.0431	-0.545 09	5.9694	15.1266
5	150.76	190.51	0.999 43	1.2509	0.783 26	-0.894 64	5.2403	33.3981
6	81.29	135.96	0.996 09	0.748 27	1.1903	-0.968 08	5.9687	37.8747
7	165.25	99.13	0.999 98	1.9905	0.092 461	-0.035 242	5.8161	20.4161
8	179.08	30.338	0.967 42	0.099 24	1.8562	0.880 88	6.0179	6.403 45

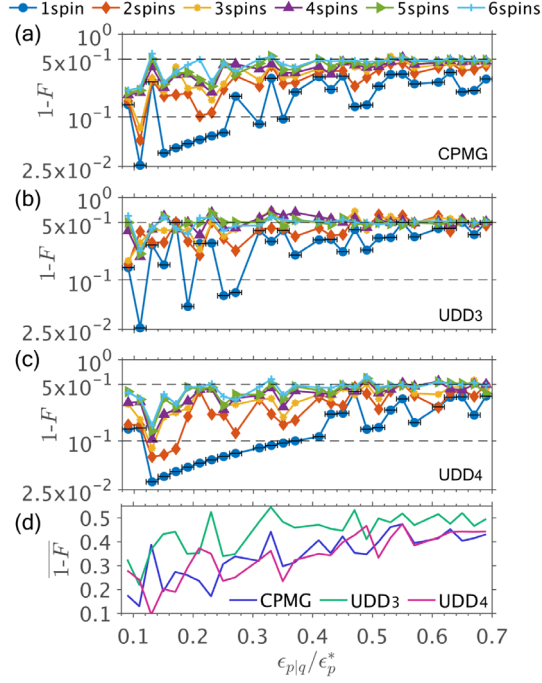


FIG. 17. Gate error $1 - F$ as a function of one-tangles (scaled by the maximum value $\epsilon_p^* = 2/9$) of unwanted nuclei for (a) CPMG, (b) UDD₃, and (c) UDD₄. The labels in all graphs show up to how many spins are “traced out” from the total system. The unwanted spins have one-tangles in the range $[0.1, 0.7]$. The error bars of the blue points show the intervals where we assign unwanted spins and are the same for all differently colored lines. The gate error shown in (a)–(c) is the average over eight different ensembles of unwanted nuclei for each bath size. In (d), we take the gate error from (a)–(c), respectively, and further average over the six different unwanted spin baths for each one-tangle range (see the text).

with $A_0 = \mu_0 \gamma_n \gamma_e \hbar / (4\pi R^3)$. We solve these equations for R and θ , assuming ^{13}C atoms, and present the values in the tables.

2. Gate error comparison for the three sequences

Here, we provide a more thorough calculation of the gate error of multipartite gates under the CPMG, UDD₃, or UDD₄ evolution. Following a similar approach as in Sec. IV B, we generate ensembles of 5×10^5 unwanted nuclear spins with randomly distributed HF parameters and identify those with one-tangles in the range $[0.1, 0.7]$. We keep the same number of repetitions and gate time we considered for each sequence in Sec. IV B. However, in this case, we repeat the random generation eight times to produce eight different ensembles of 5×10^5 unwanted nuclei. For each of these eight different ensembles, we repeat the same procedure as in Sec. IV B; we gradually increase the size of the unwanted spin bath (which contains up to six spins) and calculate the gate error it induces on the target subspace. At the end, we take the average of the error (over the eight ensembles) for each case of unwanted spin

TABLE V. Hyperfine parameters of the ^{13}C atoms we consider in Sec. IV C.

C atoms	$\frac{A}{2\pi}$ (kHz)	$\frac{B}{2\pi}$ (kHz)	C atoms	$\frac{A}{2\pi}$ (kHz)	$\frac{B}{2\pi}$ (kHz)
C1	-20.72	12	C14	-19.815	5.3
C2	-23.22	13	C15	-13.971	9
C3	-31.25	8	C16	-4.66	7
C4	-14.07	13	C17	-5.62	5
C5	-11.346	59.21	C18	-36.308	26.62
C6	-48.58	9	C19	24.399	24.81
C7	-8.32	3	C20	2.690	11
C8	-9.79	5	C21	1.212	13
C9	213.154	3	C22	7.683	4
C10	17.643	8.6	C23	-3.177	2
C11	14.548	10	C24	-4.225	0
C12	20.569	41.51	C25	-3.873	0
C13	8.029	21.0	C26	-3.618	0
C27	-4.039	0			

bath size (from one up to six spins). Notice that the eight ensembles are distinct for each sequence.

In Fig. 17, we show the gate error averaged over the eight different realizations of unwanted spin ensembles for CPMG (a), UDD₃ (b), and UDD₄ (c). We notice that CPMG performs, in general, on par with UDD₄, while UDD₃ fails to protect the target subspace as effectively as the other two sequences. Although in this scenario UDD₃ has the longest total gate time of all three sequences (as we mention in the main text), we see that choosing a longer sequence does not always ensure improved performance. To provide a comparison of the gate error, we further evaluate the average gate error in each range of one-tangles. That is, we average the gate error for each fixed interval of one-tangles as $\overline{1 - F} = 1/6(1 - F^{1\text{spin}} + 1 - F^{2\text{spins}} + \dots + 1 - F^{6\text{spins}})$. The results are shown in Fig. 17(d), where we see that UDD₃ underperforms the other two sequences.

3. Parameters for 27 nuclear spins

The HF parameters for the 27 nuclear spins [32] we consider in Sec. IV C are listed in Table V. In addition, in Tables VI–IX, we list the target spins in Fig. 8 for each of the 27 different realizations of each resonance k , their one-tangles, and the gate error.

4. Parameters for comparison of multispin operations with sequential entanglement generation

Here, we provide the parameters we consider in Sec. IV D. To obtain the optimal sequential $\text{CR}_x(\pi/2)$ gates with C4, C5, and C15, we set the time constraint of 1.5 ms for each sequential gate. We further require that the unwanted one-tangles of the remaining 26 unwanted spins are below 0.14–0.4 (we cannot satisfy the unwanted one-tangle bound of 0.14 for all cases of addressing each C_j nucleus). The unwanted one-tangles for the optimal choices we find are

TABLE VI. Target spins, one-tangles, and gate error for each case number for the $k = 1$ resonance in Fig. 8.

Case, resonance	Target spins	$\epsilon_{p q}^T/\epsilon_p^*$	Gate error
(1,1)	{C5, C10, C11, C12, C19}	{0.999 92, 0.984 16, 0.947 79, 0.994 07, 0.997 94}	0.134 41
(2,1)	{C5, C10, C11, C12, C19}	{0.999 71, 0.950 59, 0.862 47, 0.982 84, 0.999 01}	0.1162
(3,1)	{C5, C11, C12, C13, C19, C21, C22}	{0.8453, 0.994 63, 0.969 33, 0.985 94, 0.981 29, 0.975 88, 0.996 83}	0.124 47
(4,1)	{C5, C10, C11, C12, C19}	{0.997 23, 0.999 45, 0.991 04, 0.943 26, 0.955 14}	0.151 66
(5,1)	{C5, C11, C12, C13, C19, C21, C22}	{0.845 56, 0.994 68, 0.969 25, 0.985 91, 0.981 34, 0.975 84, 0.996 77}	0.1245
(6,1)	{C5, C10, C11, C12, C13, C19}	{0.923 65, 0.961 92, 0.846 89, 0.977 34, 0.960 71, 0.891 76}	0.153 78
(7,1)	{C5, C10, C11, C12, C13, C19}	{0.916 51, 0.923 15, 0.895 04, 0.929 34, 0.977 13, 0.957 19}	0.168 15
(8,1)	{C5, C10, C11, C12, C19}	{0.998 45, 0.993 21, 0.975 71, 0.997 13, 0.995 18}	0.156 31
(9,1)
(10,1)	{C5, C10, C11, C12, C19}	{1.0, 0.978 95, 0.933 09, 0.992 34, 0.9985}	0.127 88
(11,1)	{C5, C10, C11, C12, C13, C19}	{0.835 32, 0.956 52, 0.860 71, 0.900 97, 0.9606, 0.955 54}	0.141 42
(12,1)	{C5, C10, C11, C12, C19}	{0.999 73, 0.953 97, 0.872 63, 0.984 32, 0.999 05}	0.116 61
(13,1)	{C5, C10, C11, C12, C19}	{0.999 71, 0.951 99, 0.8657, 0.983 32, 0.999 02}	0.1163
(14,1)	{C5, C10, C11, C12, C13, C19}	{0.887 69, 0.971 41, 0.819 81, 0.968 51, 0.9474, 0.891 37}	0.141 73
(15,1)	{C5, C10, C11, C12, C19}	{0.996 78, 0.998 78, 0.986 62, 0.940 73, 0.9591}	0.145 17
(16,1)	{C5, C10, C11, C12, C19}	{0.999 97, 0.974 99, 0.922 39, 0.991 02, 0.998 47}	0.124 38
(17,1)	{C5, C10, C11, C12, C19}	{0.999 34, 0.9901, 0.965 67, 0.996 06, 0.996 61}	0.146 38
(18,1)	{C5, C10, C11, C12, C19}	{0.999 95, 0.983 34, 0.945 44, 0.9938, 0.998 06}	0.133 21
(19,1)	{C5, C10, C11, C12, C19}	{0.996 54, 0.998 19, 0.983 28, 0.939 01, 0.961 39}	0.141 37
(20,1)	{C5, C10, C11, C12, C19}	{0.999 98, 0.981 85, 0.941 18, 0.9933, 0.998 23}	0.131 19
(21,1)	{C5, C10, C11, C12, C19}	{0.989 23, 0.999 74, 0.995 23, 0.820 26, 0.887 72}	0.139 51
(22,1)	{C5, C11, C12, C13, C19, C21, C22}	{0.866 39, 0.997 71, 0.962 68, 0.983 38, 0.985 24, 0.972 19, 0.990 93}	0.1276
(23,1)	{C5, C10, C11, C12, C19}	{0.997 65, 0.920 23, 0.820 14, 0.998 31, 0.993 23}	0.1157
(24,1)	{C5, C10, C11, C12, C13, C19}	{0.892 27, 0.970 47, 0.8232, 0.9696, 0.949 14, 0.8914}	0.143 06
(25,1)	{C5, C10, C11, C12, C19}	{0.999 72, 0.9529, 0.867 79, 0.983 62, 0.999 03}	0.116 38
(26,1)	{C5, C11, C12, C13, C19, C21, C22}	{0.839 05, 0.993 53, 0.971 09, 0.986 64, 0.980 05, 0.976 84, 0.997 95}	0.123 82
(27,1)	{C5, C10, C11, C12, C19}	{0.999 75, 0.957 95, 0.879 66, 0.985 32, 0.999 06}	0.117 08

TABLE VII. Target spins, one-tangles, and gate error for each case number for the $k = 2$ resonance in Fig. 8.

Case, resonance	Target spins	$\epsilon_{p q}^T/\epsilon_p^*$	Gate error
(1,2)	{C12, C13, C20, C21}	{0.829 37, 0.999 07, 0.914 08, 0.969 15}	0.130 08
(2,2)	{C12, C13, C20, C21}	{0.840 17, 0.995 43, 0.911 92, 0.964 35}	0.127 29
(3,2)	{C1, C5, C14}	{0.978 21, 0.996 98, 0.970 14}	0.132 08
(4,2)	{C10, C11, C12, C19}	{0.986 93, 0.983 02, 0.987 53, 0.860 79}	0.065 161
(5,2)	{C12, C13, C20, C21}	{0.808 45, 0.991 56, 0.934 99, 0.972 61}	0.106 42
(6,2)	{C3, C5, C18}	{0.998 34, 0.929 35, 0.960 76}	0.087 809
(7,2)	{C12, C13, C20, C21}	{0.826 92, 0.9933, 0.986 08, 0.848 37}	0.055 868
(8,2)	{C3, C15, C15}	{0.9983, 0.9294, 0.9608}	0.074
(9,2)
(10,2)	{C12, C13, C20, C21}	{0.808 33, 0.991 61, 0.935 01, 0.972 65}	0.106 42
(11,2)	{C12, C13, C20, C21}	{0.905 11, 0.921 14, 0.983 17, 0.816 08}	0.070 816
(12,2)	{C10, C11, C12, C19}	{0.981 09, 0.987 71, 0.9929, 0.867 59}	0.057 813
(13,2)	{C12, C13, C20, C21}	{0.836 75, 0.996 92, 0.912 67, 0.965 98}	0.128 14
(14,2)	{C12, C13, C20, C21}	{0.802 91, 0.997 63, 0.917 43, 0.977 61}	0.137 94
(15,2)	{C12, C13, C20, C21}	{0.847 17, 0.991 25, 0.910 16, 0.960 64}	0.125 67
(16,2)	{C12, C13, C20, C21}	{0.8637, 0.917 92, 0.800 65, 0.970 57}	0.079 901
(17,2)	{C12, C13, C20, C21}	{0.8985, 0.933 71, 0.984 48, 0.822 79}	0.066 377
(18,2)	{C3, C5, C18}	{0.868 36, 0.941 77, 0.976 11}	0.095 639
(19,2)	{C12, C13, C20, C21}	{0.856 12, 0.983 21, 0.907 38, 0.954 96}	0.123 89
(20,2)	{C12, C13, C20, C21}	{0.840 67, 0.995 18, 0.9118, 0.964 11}	0.127 17
(21,2)	{C10, C11, C12, C19}	{0.932 95, 0.999 59, 0.998 59, 0.878 79}	0.036 53
(22,2)	{C12, C13, C20, C21}	{0.848 77, 0.990 04, 0.909 71, 0.959 71}	0.125 32

(Table continued)

TABLE VII. (*Continued*)

Case, resonance	Target spins	$\epsilon_{p q}^T/\epsilon_p^*$	Gate error
(23,2)	{C12, C13, C20, C21}	{0.838 47, 0.989 04, 0.986 55, 0.847 17}	0.055 117
(24,2)	{C12, C13, C20, C21}	{0.802 17, 0.997 42, 0.917 49, 0.9778}	0.138 17
(25,2)	{C10, C11, C12, C19}	{0.9923, 0.976 29, 0.978 69, 0.849 76}	0.075 422
(26,2)	{C12, C13, C20, C21}	{0.810 29, 0.990 69, 0.934 67, 0.971 99}	0.106 38
(27,2)	{C10, C11, C12, C19}	{0.948 17, 0.998 22, 0.999 93, 0.8788}	0.039 691

TABLE VIII. Target spins, one-tangles, and gate error for each case number for the $k = 3$ resonance in Fig. 8.

Case, resonance	Target spins	$\epsilon_{p q}^T/\epsilon_p^*$	Gate error
(1,3)	{C1, C2, C5}	{0.998 02, 0.955 19, 0.985 51}	0.076 654
(2,3)	{C4, C5, C15}	{0.982 89, 0.988 11, 0.998 95}	0.090 689
(3,3)	{C1, C2, C5}	{0.999 73, 0.926 45, 0.982 35}	0.085 654
(4,3)	{C4, C5, C15}	{0.960 05, 0.992 48, 0.977 39}	0.091 492
(5,3)	{C5, C16, C17}	{0.971 77, 0.9997, 0.958 42}	0.045 708
(6,3)	{C3, C18}	{0.938 76, 0.882 74}	0.046 505
(7,3)	{C1, C2, C5}	{0.993 57, 0.969 03, 0.987 01}	0.071 505
(8,3)	{C5, C16, C17}	{0.971 21, 0.999 98, 0.957 96}	0.045 857
(9,3)	{C6, C9}	{0.851 18, 0.896 31}	0.065 242
(10,3)	{C12, C19}	{0.999 78, 0.999 96}	0.037 397
(11,3)	{C12, C19}	{0.999 99, 0.999 25}	0.038 34
(12,3)	{C10, C11, C12}	{0.825, 0.971 02, 0.999 84}	0.063 887
(13,3)	{C5, C16, C17}	{0.939 99, 0.963 79, 0.997 59}	0.137 09
(14,3)	{C4, C5, C15}	{0.983 31, 0.997 33, 0.955 22}	0.096 136
(15,3)	{C4, C5, C15}	{0.999 41, 0.995 71, 0.998 54}	0.067 369
(16,3)	{C4, C5, C15}	{0.999 94, 0.9966, 0.997 58}	0.067 963
(17,3)	{C4, C5, C15}	{0.973 91, 0.984 69, 0.993 69}	0.080 809
(18,3)	{C1, C2, C5}	{0.999 48, 0.922 96, 0.981 96}	0.086 644
(19,3)	{C10, C11, C12}	{0.862 42, 0.957 45, 0.985 41}	0.068 323
(20,3)	{C5, C16, C17}	{0.974 18, 0.976 14, 0.966 38}	0.047 334
(21,3)	{C4, C5, C15}	{0.986 99, 0.989 29, 0.946 84}	0.072 855
(22,3)	{C5, C16, C17}	{0.978 87, 0.995 43, 0.946 63}	0.065 835
(23,3)	{C4, C5, C15}	{0.999 94, 0.996 62, 0.997 56}	0.067 977
(24,3)	{C4, C5, C15}	{0.985 78, 0.997 81, 0.951 56}	0.096 777
(25,3)	{C4, C5, C15}	{0.998 99, 0.988 88, 0.9961}	0.082 447
(26,3)	{C5, C16, C17}	{0.972 62, 0.998 41, 0.959 37}	0.045 567
(27,3)	{C4, C5, C15}	{0.9882, 0.989 58, 0.999 68}	0.064 595

TABLE IX. Target spins, one-tangles, and gate error for each case number for the $k = 4$ and $k = 5$ resonance in Fig. 8.

Case, resonance	Target spins	$\epsilon_{p q}^T/\epsilon_p^*$	Gate error	Case, resonance	Target spins	$\epsilon_{p q}^T/\epsilon_p^*$	Gate error
(1,4)	{C4, C5, C15}	{0.997 81, 0.996 36, 0.998 31}	0.053 818	(1,5)	{C4, C5, C15}	{0.9144, 1, 0.986 98}	0.025 322
(2,4)	{C1, C5, C14}	{0.979 19, 0.997 46, 0.995 52}	0.074 751	(2,5)	{C4, C5, C15}	{0.999 03, 0.987 28, 0.996 31}	0.022 729
(3,4)	{C1, C5, C14}	{0.9942, 0.995 17, 0.982 06}	0.055 318	(3,5)	{C1, C5, C14}	{0.998 18, 0.870 03, 0.850 05}	0.056 428
(4,4)	{C4, C5, C15}	{0.970 17, 0.994 92, 0.983 28}	0.071 316	(4,5)	{C4, C5, C15}	{0.927 56, 0.999 42, 0.984 65}	0.025 334
(5,4)	{C4, C5, C15}	{0.997 34, 0.989 92, 0.999 43}	0.053 567	(5,5)	{C4, C5, C15}	{0.998 89, 0.994 63, 0.917 21}	0.022 455
(6,4)	{C6, C9}	{0.849 38, 0.897 01}	0.065 279	(6,5)
(7,4)	{C1, C5, C14}	{0.997 83, 0.998, 0.965 11}	0.034 986	(7,5)	{C4, C5, C15}	{0.997 73, 0.992 32, 0.9129}	0.022 384
(8,4)	{C4, C5, C15}	{0.955 84, 0.996 67, 0.976 78}	0.071 062	(8,5)	{C4, C5, C15}	{0.997 09, 0.989 72, 0.994 43}	0.022 413
(9,4)	{C12, C19}	{0.949 43, 0.9978}	0.055 554	(9,5)
(10,4)	{C12, C19}	{0.999 65, 0.998 88}	0.019 047	(10,5)	{C10, C12}	{0.997 49, 0.999 63}	0.087 708
(11,4)	{C12, C19}	{0.999 83, 0.998 06}	0.018 949	(11,5)	{C10, C12}	{0.974 77, 0.9974}	0.047 869

(Table continued)

TABLE IX. (Continued)

Case, resonance	Target spins	$\epsilon_{p q}^T/\epsilon_p^*$	Gate error	Case, resonance	Target spins	$\epsilon_{p q}^T/\epsilon_p^*$	Gate error
(12,4)	{C12, C19}	{0.995 61, 0.997 18}	0.039 132	(12,5)	{C10, C12}	{0.984 42, 0.995 69}	0.047 928
(13,4)	{C10, C12}	{0.999 16, 0.996 39}	0.015 197	(13,5)	{C20, C21}	{0.999 96, 0.989 58}	0.075 203
(14,4)	{C4, C5, C15}	{0.993 33, 0.989 22, 0.994 89}	0.071 773	(14,5)	{C4, C5, C15}	{0.999 84, 0.985 08, 0.997 59}	0.022 995
(15,4)	{C4, C5, C15}	{0.987 11, 0.998 92, 0.992 49}	0.054 07	(15,5)	{C4, C5, C15}	{0.985 48, 0.998 83, 0.995 86}	0.019 793
(16,4)	{C4, C5, C15}	{0.999 07, 0.991 56, 0.99999}	0.053 608	(16,5)	{C4, C5, C15}	{0.976 24, 0.997 43, 0.982 04}	0.021 121
(17,4)	{C4, C5, C15}	{0.957 75, 0.998 75, 0.999 76}	0.077 026	(17,5)	{C4, C5, C15}	{0.910 76, 0.999 95, 0.987 55}	0.025 321
(18,4)	{C2, C5}	{1, 0.906 04}	0.094 235	(18,5)
(19,4)	{C12, C19}	{0.995 72, 0.997 16}	0.039 168	(19,5)	{C10, C12}	{0.999 86, 0.999 62}	0.037 721
(20,4)	{C16, C17}	{0.999 94, 0.999 37}	0.076 236	(20,5)	{C20, C21}	{0.998 03, 0.997 65}	0.069 339
(21,4)	{C16, C17}	{0.9741, 0.998 81}	0.046 931	(21,5)	{C20, C21}	{1, 0.988 65}	0.041 343
(22,4)	{C10, C12}	{0.999 98, 0.999 75}	0.040 316	(22,5)	{C10, C12}	{0.995 92, 0.999 97}	0.083 296
(23,4)	{C4, C5, C15}	{0.9695, 0.995 02, 0.982 97}	0.071 304	(23,5)	{C4, C5, C15}	{0.996 12, 0.989 56, 0.908 37}	0.022 317
(24,4)	{C4, C5, C15}	{0.991 34, 0.990 04, 0.993 79}	0.071 728	(24,5)	{C4, C5, C15}	{0.999 28, 0.986 78, 0.996 63}	0.022 791
(25,4)	{C4, C5, C15}	{0.9693, 0.99901, 0.99898}	0.041347	(25,5)	{C4, C5, C15}	{0.96988, 0.99834, 0.97894}	0.020891
(26,4)	{C4, C5, C15}	{0.999 22, 0.991 76, 0.999 93}	0.053 613	(26,5)	{C4, C5, C15}	{0.997 46, 0.991 85, 0.912 08}	0.022 372
(27,4)	{C4, C5, C15}	{0.982 15, 0.999 49, 0.992 79}	0.075 682	(27,5)	{C4, C5, C15}	{0.996 87, 0.990 81, 0.910 36}	0.022 346

listed in Table X. The rotation angles and axes for the sequential and multispin gates in Fig. 9 are listed in Table XI.

5. QEC with CR_{xz} multispin gates

In this section, we provide the details of how we implement the three-qubit bit-flip code using the CR_{xz} gates. First, we explain the three-qubit bit-flip code that utilizes the sequential $\text{CR}_{\pm x}(\pi/2)$ gates. The circuit to implement the QEC code using the latter scheme is shown in Fig. 18(a); the CNOT gates used in the usual QEC code are expressed in terms of the $\text{CR}_{\pm x}(\pi/2)$ gates as well as initialization of the nuclei into the $|1\rangle$ state, while the Toffoli gate is decomposed into single-qubit gates and $\text{CR}_{\pm x}(\pi/2)$ gates. The $\text{CR}_{\pm x}(\pi/2)$ shown in Fig. 18 are given by

$$\text{CR}_{\pm x}(\pi/2) = \sigma_{00} \otimes R_x(\pi/2) + \sigma_{11} \otimes R_{-x}(\pi/2), \quad (\text{K3})$$

where we define $R_x(\phi) = e^{-i(\phi/2)\sigma_x}$. The half-white, half-black control implies that when the electron is in the $|0\rangle$ state, the nuclear spin still undergoes a rotation, but it differs from the one it undergoes when the electron is in the $|1\rangle$ state. The electron rotation angles θ_j have to satisfy particular relations to ensure recovery of the electron's state.

Let us start with the sequential protocol. If a bit flip happens on the electron, then the final (after the correction) three-qubit state has the form [in the basis $\{|000\rangle, |001\rangle, |010\rangle, |011\rangle, |100\rangle, |101\rangle, |110\rangle, |111\rangle\}$]

$$|\psi_f\rangle = \frac{1}{2} \begin{pmatrix} -\beta \cos(\frac{\Theta}{2}) + i\alpha \sin(\frac{\Theta}{2}) \\ -\beta \cos(\frac{\Theta}{2}) + i\alpha \sin(\frac{\Theta}{2}) \\ -\beta \cos(\frac{\Theta}{2}) + i\alpha \sin(\frac{\Theta}{2}) \\ -\beta \cos(\frac{\Theta}{2}) + i\alpha \sin(\frac{\Theta}{2}) \\ -\alpha \cos(\frac{\Theta}{2}) + i\beta \sin(\frac{\Theta}{2}) \\ -\alpha \cos(\frac{\Theta}{2}) + i\beta \sin(\frac{\Theta}{2}) \\ -\alpha \cos(\frac{\Theta}{2}) + i\beta \sin(\frac{\Theta}{2}) \\ -\alpha \cos(\frac{\Theta}{2}) + i\beta \sin(\frac{\Theta}{2}) \end{pmatrix}, \quad (\text{K4})$$

where we define $\Theta = \theta_1 - \theta_2 - \theta_3 + \theta_4$. Clearly, in order to recover the initial state of the electron, it has to hold that $\Theta = (2k + 1)\pi$. Under this condition, one can verify that the final state is $(\alpha|0\rangle + \beta|1\rangle)|x\rangle|x\rangle$, with $|x\rangle = (|0\rangle + |1\rangle)/\sqrt{2}$.

If no error occurs, then the final state is

$$|\psi_f\rangle = \frac{1}{2} \begin{pmatrix} \alpha \cos(\frac{\Theta}{2}) + i\beta \sin(\frac{\Theta}{2}) \\ -\alpha \cos(\frac{\Theta}{2}) - i\beta \sin(\frac{\Theta}{2}) \\ -\alpha \cos(\frac{\Theta}{2}) - i\beta \sin(\frac{\Theta}{2}) \\ \alpha \cos(\frac{\Theta}{2}) + i\beta \sin(\frac{\Theta}{2}) \\ \beta \cos(\frac{\Theta}{2}) + i\alpha \sin(\frac{\Theta}{2}) \\ -\beta \cos(\frac{\Theta}{2}) - i\alpha \sin(\frac{\Theta}{2}) \\ -\beta \cos(\frac{\Theta}{2}) - i\alpha \sin(\frac{\Theta}{2}) \\ \beta \cos(\frac{\Theta}{2}) + i\alpha \sin(\frac{\Theta}{2}) \end{pmatrix}, \quad (\text{K5})$$

TABLE X. Nuclear one-tangles when we aim to entangle only a C4 or C5 or C15 atom with the electron. The optimal parameters for C4 are $(N^*, k^*) = (82, 3)$, $1 - F = 0.1133$, and $T^* \approx 0.9337$ ms. There is no other optimal case for C4 within the time constraint of 1.5 ms and unwanted one-tangles below 0.2. The optimal parameters for C5 are $(N^*, k^*) = (6, 3)$, $T^* \approx 68.24$ μ s, and $1 - F = 0.1045$; there are other cases that satisfy the time constraint and tolerance of unwanted one-tangles of 0.14, but we select the fastest option. The optimal parameters for C15 are $(N^*, k^*) = (118, 3)$, $T^* \approx 1.3439$ ms, and $1 - F = 0.1421$; the tolerance for unwanted one-tangles for C15 is 0.31. For the time constraint of 1.5 ms, we find no other optimal case to address only C15.

C4					
C atoms	$\epsilon_{p q}/\epsilon_p^*$	C atoms	$\epsilon_{p q}/\epsilon_p^*$	C atoms	$\epsilon_{p q}/\epsilon_p^*$
C1	0.0498	C2	0.0968	C3	0.0001
C4	0.9993	C5	0.0645	C6	0.0002
C7	0.0062	C8	0.0062	C9	0.0001
C10	0.0005	C11	0.0044	C12	0.0565
C13	0.0198	C14	0.0490	C15	0.1767
C16	0.0289	C17	0.0002	C18	0.0546
C19	0.0065	C20	0.0031	C21	0.0098
C22	0.0007	C23	0.0005	C24	0
C25	0	C26	0	C27	0

C5					
C atoms	$\epsilon_{p q}/\epsilon_p^*$	C atoms	$\epsilon_{p q}/\epsilon_p^*$	C atoms	$\epsilon_{p q}/\epsilon_p^*$
C1	0.0925	C2	0.0967	C3	0.0173
C4	0.1130	C5	1	C6	0.0011
C7	0.0048	C8	0.0147	C9	0.0001
C10	0.0003	C11	0	C12	0.0132
C13	0.0148	C14	0.0191	C15	0.0551
C16	0.0193	C17	0.0108	C18	0.0541
C19	0.0096	C20	0.0162	C21	0.0300
C22	0.0005	C23	0.0013	C24	0
C25	0	C26	0	C27	0

C15					
C atoms	$\epsilon_{p q}/\epsilon_p^*$	C atoms	$\epsilon_{p q}/\epsilon_p^*$	C atoms	$\epsilon_{p q}/\epsilon_p^*$
C1	0.1296	C2	0.1054	C3	0.0135
C4	0.3086	C5	0.0030	C6	0.0030
C7	0.0031	C8	0.0115	C9	0.0003
C10	0.0014	C11	0.0011	C12	0.0143
C13	0.0378	C14	0.0036	C15	0.9999
C16	0.0201	C17	0.0149	C18	0.0901
C19	0.0132	C20	0.0072	C21	0.0115
C22	0.0014	C23	0.0012	C24	0
C25	0	C26	0	C27	0

where we define $\tilde{\Theta} = \theta_1 + \theta_2 - \theta_3 - \theta_4$. Clearly, in order to preserve the initial state of the electron, it has to hold that $\tilde{\Theta} = 2\kappa\pi$. In this case, the final state is $(\alpha|0\rangle + \beta|1\rangle)|\tilde{x}\rangle|\tilde{x}\rangle$, where $|\tilde{x}\rangle = (|0\rangle - |1\rangle)/\sqrt{2}$.

Based on the above observations, we find that we can satisfy both conditions for Θ and $\tilde{\Theta}$ if we choose the θ_j to satisfy

TABLE XI. Nuclear rotation axes and rotation angles for the multispin operation (case 23, $k = 3$) and the sequential gates we discuss in Sec. IV D.

	Multispin gate		
	C4	C5	C15
$n_{x,0}$	-0.7532	0.9468	0.6832
$n_{y,0}$	0	0	0
$n_{z,0}$	-0.6566	0.3219	0.7302
$n_{x,1}$	0.7754	-0.9844	-0.6996
$n_{y,1}$	0	0	0
$n_{z,1}$	-0.6314	0.1758	0.7145
$\phi/(\pi/2)$	1.5136	1.0028	1.9021

	Sequential gates		
	C4	C5	C15
$n_{x,0}$	-1	0.999 96	-1
$n_{y,0}$	0	0	0
$n_{z,0}$	0	0.009 05	0
$n_{x,1}$	0.999 52	-0.98996	0.999 77
$n_{y,1}$	0	0	0
$n_{z,1}$	0.031	-0.14314	0.021
$\phi/(\pi/2)$	0.982 82	1.0048	0.099 227

$$\theta_2 = \theta_1, \quad \theta_3 = \theta_1 - 3\pi/2, \quad \theta_4 = \theta_3 + \pi. \quad (\text{K6})$$

It is clear that in the sequential protocol if no error occurs on the electron's state, the $\text{CR}_{\pm x}(\pi/2)$ gates of the encoding add up with those of the decoding step to produce $\text{CR}_{\pm x}(\pi)$ gates which flip both nuclear spins into the $|00\rangle$ state, and, hence, the subsequent Toffoli gate is not activated. We should further mention that, in the case where a single bit flip happens on either the first or second nuclear spin, and we are interested in preserving the initial state of the electron, then the θ_j need to be constrained further. That is, we have two more conditions; namely, if the bit flip happens on the first nucleus, then the angles need to satisfy $\theta_1 + \theta_2 + \theta_3 + \theta_4 = 2\pi$, whereas if the bit flip happens on the second nucleus, the angles need to satisfy $\theta_1 - \theta_2 + \theta_3 - \theta_4 = 2\pi$. Combining these constraints with the θ_j constraints when a bit flip or no bit flip happens on the electron, we find that θ_j need to satisfy

$$\theta_1 = \theta_4 = -\pi/4 = -\theta_2 = -\theta_3. \quad (\text{K7})$$

Let us return to the CR_{xz} QEC protocol and consider first the case where no error happens on the electron. Now, the CR_{xz} gates of the encoding and decoding again add up, but, in general, the total gate is not equivalent to a bit-flip operation that brings the state $|11\rangle$ of the nuclei into the

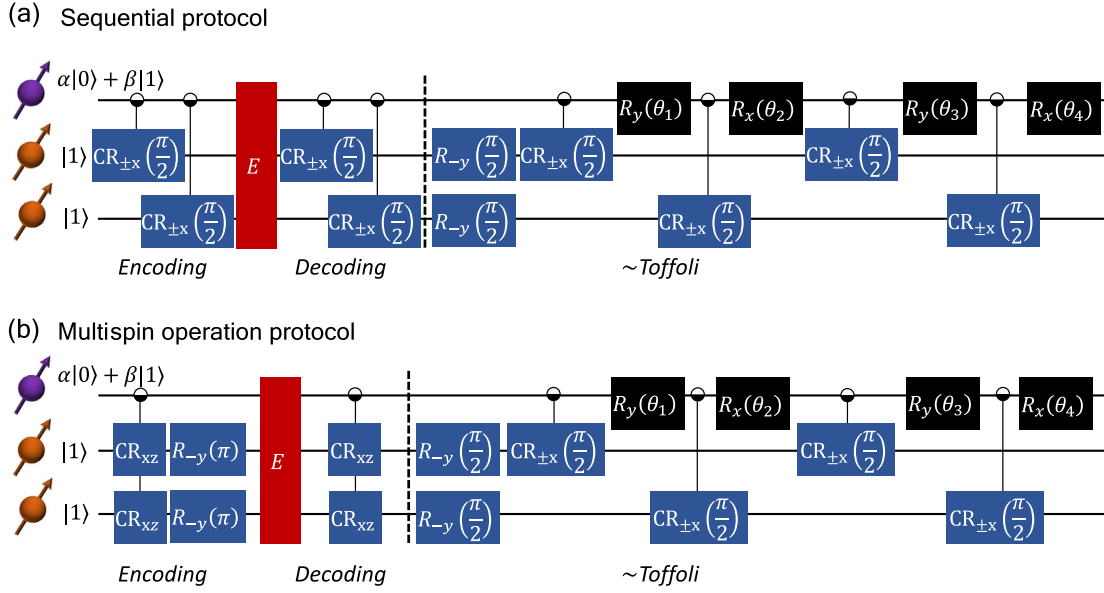


FIG. 18. Circuit diagrams to correct a bit flip on the electron for (a) the sequential approach that utilizes the $\text{CR}_x(\pi/2)$ gates and (b) the multispin operation protocol. E denotes the bit-flip error, which can happen either on the electron or on one of the nuclei. In (b), we further require the $R_{-y}(\pi)$ unconditional rotations on the nuclear spins for the encoding step. These rotations can be performed at either the encoding step after the CR_{xz} gate or the decoding step before the CR_{xz} gate. The half-white, half-black circles of the control of the $\text{CR}_{\pm x}(\pi/2)$ gates indicate that, depending on the electron's state, the nuclear spin rotates by $R_x(\pi/2)$ or $R_x(-\pi/2)$. For the CR_{xz} gates, the half-white, half-black notation means that, depending on the electron's state, the nuclear spin rotates by R_{n_0} or R_{n_1} .

$|00\rangle$ state. However, if we put $R_y(-\pi)$ gates on the nuclei at the encoding step and right after the CR_{xz} gate, we then have the total gate $\text{CR}_{xz}[\mathbb{1}_{2\times 2} \otimes R_y(-\pi) \otimes R_y(-\pi)]\text{CR}_{xz}$.

If we consider the case when the electron is in the $|0\rangle$ state and consider the part of the gate acting on the first nuclear spin, we find that the total gate is

$$\begin{aligned}
 R_{n_0}^{(0)} R_y(-\pi) R_{n_0}^{(0)} &= \left[\cos \frac{\phi}{2} - i \sin \frac{\phi}{2} (n_{x,0} \sigma_x + n_{z,0} \sigma_z) \right] [i\sigma_y] \left[\cos \frac{\phi}{2} - i \sin \frac{\phi}{2} (n_{x,0} \sigma_x + n_{z,0} \sigma_z) \right] \\
 &= \left[\cos \frac{\phi}{2} i\sigma_y + i \sin \frac{\phi}{2} (n_{x,0} \sigma_z - n_{z,0} \sigma_x) \right] \left[\cos \frac{\phi}{2} - i \sin \frac{\phi}{2} (n_{x,0} \sigma_x + n_{z,0} \sigma_z) \right] \\
 &= \cos^2 \frac{\phi}{2} i\sigma_y + \sin^2 \frac{\phi}{2} (n_{x,0} \sigma_z - n_{z,0} \sigma_x) (n_{x,0} \sigma_x + n_{z,0} \sigma_z) \\
 &= \cos^2 \frac{\phi}{2} i\sigma_y + \sin^2 \frac{\phi}{2} (n_{x,0}^2 + n_{z,0}^2) i\sigma_y = i\sigma_y,
 \end{aligned} \tag{K8}$$

where in the last line we use the fact that time-symmetric π sequences do not produce an n_y rotation component and, thus, $n_x^2 + n_z^2 = 1$. (Note that we consider here a π -pulse sequence that produces the same rotation angles irrespective of the electron's state, i.e., $\phi_0 = \phi_1 \equiv \phi$.) The same analysis follows for the second nuclear spin and for the case when the electron is in state $|1\rangle$, and, thus, $\text{CR}_{xz}[\mathbb{1}_{2\times 2} \otimes R_y(-\pi) \otimes R_y(-\pi)]\text{CR}_{xz}$ is equivalent to $i^2 \mathbb{1}_{2\times 2} \otimes \sigma_y \otimes \sigma_y$ if no error occurs on the electron. Thus, we see that the $\text{CR}_{xz}[\mathbb{1}_{2\times 2} \otimes R_y(-\pi) \otimes R_y(-\pi)]\text{CR}_{xz}$ gate leads to the desired bit-flip operation of the nuclei, deactivating the subsequent Toffoli gate. This is verified schematically in Figs. 19(a) and 19(b), where we show the Bloch sphere evolution of nuclear

spins C10 and C12 (that we considered in Sec. IV D), respectively, up to the decoding, assuming no error occurs on the electron.

Now, let us assume that a bit-flip error happens on the electron. At the encoding step, which includes the $R_y(-\pi)$ rotations, the encoded state becomes

$$\begin{aligned}
 |\psi_{\text{enc}}\rangle &= \alpha|0\rangle \otimes R_y(-\pi) R_{n_0}^{(1)} |1\rangle \otimes R_y(-\pi) R_{n_0}^{(2)} |1\rangle \\
 &\quad + \beta|1\rangle \otimes R_y(-\pi) R_{n_1}^{(1)} |1\rangle \otimes R_y(-\pi) R_{n_1}^{(2)} |1\rangle.
 \end{aligned} \tag{K9}$$

After the bit flip and the decoding step, the state becomes

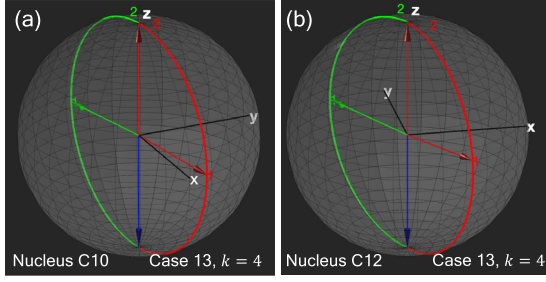


FIG. 19. Evolution of nuclear spins C10 (a) and C12 (b) up to the decoding, if no error occurs on the electron during the CR_{xz} QEC protocol. Initially, both nuclei are in the $|1\rangle$ state (blue arrow). If the electron starts in the $|0\rangle$ ($|1\rangle$) state, the nuclear spins follow the green (red) trajectory. The final state of each spin is indicated with the red arrow pointing to the North pole of the Bloch sphere (the final green and red arrows coincide).

$$|\psi_{\text{dec}}\rangle = \alpha|1\rangle \otimes R_{\mathbf{n}_1}^{(1)} R_y(-\pi) R_{\mathbf{n}_0}^{(1)} |1\rangle \otimes R_{\mathbf{n}_1}^{(2)} R_y(-\pi) R_{\mathbf{n}_0}^{(2)} |1\rangle \\ + \beta|0\rangle \otimes R_{\mathbf{n}_0}^{(1)} R_y(-\pi) R_{\mathbf{n}_1}^{(1)} |1\rangle \otimes R_{\mathbf{n}_0}^{(2)} R_y(-\pi) R_{\mathbf{n}_1}^{(2)} |1\rangle. \quad (\text{K10})$$

These four sets of gates approximately leave the nuclei at the state $|11\rangle$ such that we activate the Toffoli gate, recovering the electron's state with high probability. To see this, let us consider $R_{\mathbf{n}_0}^{(j)} R_y(-\pi) R_{\mathbf{n}_1}^{(j)}$, which reads

$$R_{\mathbf{n}_0}^{(j)} R_y(-\pi) R_{\mathbf{n}_1}^{(j)} = \hat{\mathbf{y}} \cdot (\mathbf{n}_1 \times \mathbf{n}_0)^{(j)} \sin^2 \frac{\phi}{2} \mathbb{1} \\ + i \sin \phi [(n_{x,0}^{(j)} - n_{x,1}^{(j)}) \sigma_z - (n_{z,0}^{(j)} - n_{z,1}^{(j)}) \sigma_x] \\ + i \sqrt{G_1^{(j)}} \sigma_y, \quad (\text{K11})$$

where $G_1^{(j)} = \cos^2(\phi^{(j)}/2) + \sin^2(\phi^{(j)}/2)(\mathbf{n}_0 \cdot \mathbf{n}_1)^{(j)}$. Since for the multispin gates we choose the number of iterations N such that $G_1^{(j)}$ is minimized for all j -nuclear spins (i.e., $G_1^{(j)} \approx 0$, $\forall j$), then the y component of the composite rotation vanishes. Furthermore, for the CR_{xz} gates and considering the CPMG sequence, it holds that $n_{x,0} \cdot n_{x,1} < 0$ and that $n_{z,0} \approx n_{z,1} + \delta$, where δ is small, as we show shortly (for brevity, we drop superscripts j which refer to the j th spin). Let us further consider the action of the CR_{xz} gate on a single nuclear spin (similar analysis holds for more nuclei). As we mention in Appendix A 1, the evolution of a nuclear spin over one unit of the CPMG sequence is defined by the Hamiltonians $H_j = \frac{1}{2}[(\omega_L + s_j A)Z + (s_j B)X]$, where the nuclear rotations over one unit of the sequence are $R_{\mathbf{n}_0} = e^{-iH_0 t/4} e^{-iH_1 t/2} e^{-iH_0 t/4}$ and $R_{\mathbf{n}_1} = e^{-iH_1 t/4} e^{-iH_0 t/2} e^{-iH_1 t/4}$. Letting $\cos \theta_j = (\omega_L + s_j A)/\omega_j$ [where $\omega_j = \sqrt{(\omega_L + s_j A)^2 + (s_j B)^2}$] and $\sin \theta_j = s_j B/\omega_j$, we find the $\text{SU}(2)$ decomposition of Eq. (K11), and focusing on the z components we find that it holds that

$$\sin \frac{\phi}{2} (n_{z,1} - n_{z,0}) = 2 \sin(\theta_0 - \theta_1) \left[\sin \theta_1 \sin \frac{t\omega_0}{4} \sin^2 \frac{t\omega_1}{8} \right. \\ \left. + \sin \theta_0 \sin \frac{t\omega_1}{4} \sin^2 \frac{t\omega_0}{8} \right]. \quad (\text{K12})$$

Note that $\sin(\theta_0 - \theta_1) = \omega_L B(s_1 - s_0)/(\omega_0 \omega_1)$ and that $\sin \theta_j = s_j B/\omega_j$, meaning that, for $\omega_L \gg A, B$, we have

$$\sin \frac{\phi}{2} (n_{z,1} - n_{z,0}) \approx 2 \frac{(s_1 - s_0)B}{\omega_L} \left[\frac{s_1 B}{\omega_L} \sin \frac{t\omega_0}{4} \sin^2 \frac{t\omega_1}{8} \right. \\ \left. + \frac{s_0 B}{\omega_L} \sin \frac{t\omega_1}{4} \sin^2 \frac{t\omega_0}{8} \right] \quad (\text{K13})$$

or

$$\sin \frac{\phi}{2} (n_{z,1} - n_{z,0}) \propto \left(\frac{B}{\omega_L} \right)^2. \quad (\text{K14})$$

TABLE XII. Optimal iterations (N^*) and resonances (k^*) to perform $\text{CR}_x(\pi/2)$ between the electron and C12 or C10. We provide a list of optimal cases for $T \leq 1.5$ ms for C12. For C10, we cannot satisfy the bound of unwanted one-tangles for this time constraint, so we further list cases for T up to 5 ms.

C12					
	Gate time (μs)	Gate error	N^*	k^*	$\phi/(\pi/2)$
#1	170.3095	0.1080	8	5	0.975 67
#2	208.156	0.0867	8	6	0.951 98
#3	276.7529	0.0732	9	7	1.0393
#4	319.33	0.0319	9	8	1.0027
#5	361.9076	0.0273	9	9	0.961 37
#6	449.4277	0.0238	10	10	1.0172
#7	1054.9725	0.2428	446	1	1.066
#8	1125.9347	0.0800	28	9	1.0091
#9	1303.3404	0.0549	29	10	1.05
#10	1457.092	0.0604	88	4	1.0578
C10					
	Gate time (μs)	Gate error	N^*	k^*	$\phi/(\pi/2)$
#1	645.0498	0.3839	39	4	1.0038
#2	850.6152	0.4150	40	5	1.0118
#3	985.2959	0.4208	417	1	0.987 72
#4	1039.6407	0.4292	40	6	0.989 76
#5	1290.0997	0.4821	42	7	1.0117
#6	1358.6214	0.4732	115	3	1.0016
#7	1524.0188	0.5455	43	8	1.0032
#8	1767.3893	0.4753	44	9	0.988 82
#9	2065.1046	0.5144	46	10	0.989 96
#10	2431.3417	0.3214	49	11	1.0034
#11	2530.5801	0.2248	119	5	0.989 91
#12	2825.9326	0.1953	52	12	1.006
#13	3144.9133	0.1058	121	6	1.006
#14	4075.8643	0.1124	345	3	0.995 06
#15	4453.9155	0.1326	65	15	1.0064
#16	4572.0565	0.1679	129	8	0.9904

Thus, in Eq. (K11), we have suppressed x component of rotation, meaning that each nucleus rotates approximately around the z axis irrespective of the electron's state. Since each nucleus is initialized in the $|1\rangle$ state, an R_z rotation only approximately leads to a global phase. The nonzero difference of the z -axis components is what makes our CR_{xz} QEC protocol probabilistic, since the disentanglement at the decoding step is imperfect, but it succeeds with high probability because the difference in the z components is, in general, small (the external B field is typically chosen such that $\omega_L \gg A, B$).

6. Parameters for three-qubit QEC with $\text{CR}_x(\pi/2)$

In Table XII, we provide a list of the optimal $\text{CR}_x(\pi/2)$ gates for nuclear spins C10 and C12 using the sequential entanglement scheme, we considered in Sec. IV D.

-
- [1] W. Kozłowski and S. Wehner, *Towards Large-Scale Quantum Networks*, in *Proceedings of the Sixth Annual ACM International Conference on Nanoscale Computing and Communication*, NANOCOM '19 (Association for Computing Machinery, New York, 2019).
- [2] H.-J. Briegel, W. Dür, J. I. Cirac, and P. Zoller, *Quantum Repeaters: The Role of Imperfect Local Operations in Quantum Communication*, *Phys. Rev. Lett.* **81**, 5932 (1998).
- [3] N. Lo Piparo, M. Razavi, and W. J. Munro, *Memory-Assisted Quantum Key Distribution with a Single Nitrogen-Vacancy Center*, *Phys. Rev. A* **96**, 052313 (2017).
- [4] M. Leifgen, T. Schröder, F. Gädeke, R. Riemann, V. Métilion, E. Neu, C. Hepp, C. Arend, C. Becher, K. Lauritsen, and O. Benson, *Evaluation of Nitrogen- and Silicon-Vacancy Defect Centres as Single Photon Sources in Quantum Key Distribution*, *New. J. Phys.* **16**, 023021 (2014).
- [5] R. Schwonnek, K. T. Goh, I. W. Primaatmaja, E. Y.-Z. Tan, R. Wolf, V. Scarani, and C. C.-W. Lim, *Device-Independent Quantum Key Distribution with Random Key Basis*, *Nat. Commun.* **12**, 2880 (2021).
- [6] S. Wengerowsky, S. K. Joshi, F. Steinlechner, H. Hübel, and R. Ursin, *An Entanglement-Based Wavelength-Multiplexed Quantum Communication Network*, *Nature (London)* **564**, 225 (2018).
- [7] S. Zaiser, T. Rendler, I. Jakobi, T. Wolf, S.-Y. Lee, S. Wagner, V. Bergholm, T. Schulte-Herbrüggen, P. Neumann, and J. Wrachtrup, *Enhancing Quantum Sensing Sensitivity by a Quantum Memory*, *Nat. Commun.* **7**, 12279 (2016).
- [8] A. Cooper, Won Kyu Calvin Sun, J.-C. Jaskula, and P. Cappellaro, *Environment-Assisted Quantum-Enhanced Sensing with Electronic Spins in Diamond*, *Phys. Rev. Appl.* **12**, 044047 (2019).
- [9] V. Vorobyov, S. Zaiser, N. Abt, J. Meinel, D. Dasari, P. Neumann, and J. Wrachtrup, *Quantum Fourier Transform for Nanoscale Quantum Sensing*, *npj Quantum Inf.* **7**, 124 (2021).
- [10] H. Bernien, B. Hensen, W. Pfaff, G. Koolstra, M. S. Blok, L. Robledo, T. H. Taminiau, M. Markham, D. J. Twitchen, L. Childress, and R. Hanson, *Heralded Entanglement between Solid-State Qubits Separated by Three Metres*, *Nature (London)* **497**, 86 (2013).
- [11] M. Pompili, S. L. N. Hermans, S. Baier, H. K. C. Beukers, P. C. Humphreys, R. N. Schouten, R. F. L. Vermeulen, M. J. Tiggelman, L. dos Santos Martins, B. Dirkse, S. Wehner, and R. Hanson, *Realization of a Multinode Quantum Network of Remote Solid-State Qubits*, *Science* **372**, 259 (2021).
- [12] N. Kalb, A. A. Reiserer, P. C. Humphreys, J. J. W. Bakermans, S. J. Kamerling, N. H. Nickerson, S. C. Benjamin, D. J. Twitchen, M. Markham, and R. Hanson, *Entanglement Distillation between Solid-State Quantum Network Nodes*, *Science* **356**, 928 (2017).
- [13] C. T. Nguyen, D. D. Sukachev, M. K. Bhaskar, B. Machielse, D. S. Levonian, E. N. Knall, P. Stroganov, R. Riedinger, H. Park, M. Lončar, and M. D. Lukin, *Quantum Network Nodes Based on Diamond Qubits with an Efficient Nanophotonic Interface*, *Phys. Rev. Lett.* **123**, 183602 (2019).
- [14] C. T. Nguyen, D. D. Sukachev, M. K. Bhaskar, B. Machielse, D. S. Levonian, E. N. Knall, P. Stroganov, C. Chia, M. J. Burek, R. Riedinger, H. Park, M. Lončar, and M. D. Lukin, *An Integrated Nanophotonic Quantum Register Based on Silicon-Vacancy Spins in Diamond*, *Phys. Rev. B* **100**, 165428 (2019).
- [15] R. Stockill, M. J. Stanley, L. Huthmacher, E. Clarke, M. Hugues, A. J. Miller, C. Matthiesen, C. Le Gall, and M. Atatüre, *Phase-Tuned Entangled State Generation between Distant Spin Qubits*, *Phys. Rev. Lett.* **119**, 010503 (2017).
- [16] T. Neuman, M. Eichenfield, M. E. Trusheim, L. Hackett, P. Narang, and D. Englund, *A Phononic Interface between a Superconducting Quantum Processor and Quantum Networked Spin Memories*, *npj Quantum Inf.* **7**, 121 (2021).
- [17] C. Monroe, R. Raussendorf, A. Ruthven, K. R. Brown, P. Maunz, L.-M. Duan, and J. Kim, *Large-Scale Modular Quantum-Computer Architecture with Atomic Memory and Photonic Interconnects*, *Phys. Rev. A* **89**, 022317 (2014).
- [18] D. Hucul, I. V. Inlek, G. Vittorini, C. Crocker, S. Debnath, S. M. Clark, and C. Monroe, *Modular Entanglement of Atomic Qubits Using Photons and Phonons*, *Nat. Phys.* **11**, 37 (2015).
- [19] T. H. Taminiau, J. J. T. Wagenaar, T. van der Sar, F. Jelezko, V. V. Dobrovitski, and R. Hanson, *Detection and Control of Individual Nuclear Spins Using a Weakly Coupled Electron Spin*, *Phys. Rev. Lett.* **109**, 137602 (2012).
- [20] P. C. Humphreys, N. Kalb, J. P. J. Morits, R. N. Schouten, R. F. L. Vermeulen, D. J. Twitchen, M. Markham, and R. Hanson, *Deterministic Delivery of Remote Entanglement on a Quantum Network*, *Nature (London)* **558**, 268 (2018).
- [21] T. H. Taminiau, J. Cramer, T. van der Sar, V. V. Dobrovitski, and R. Hanson, *Universal Control and Error Correction in Multi-qubit Spin Registers in Diamond*, *Nat. Nanotechnol.* **9**, 171 (2014).
- [22] J. Cramer, N. Kalb, M. A. Rol, B. Hensen, M. S. Blok, M. Markham, D. J. Twitchen, R. Hanson, and T. H. Taminiau, *Repeated Quantum Error Correction on a Continuously Encoded Qubit by Real-Time Feedback*, *Nat. Commun.* **7**, 11526 (2016).

- [23] M. H. Abobeih, Y. Wang, J. Randall, S. J. H. Loenen, C. E. Bradley, M. Markham, D. J. Twitchen, B. M. Terhal, and T. H. Taminiau, *Fault-Tolerant Operation of a Logical Qubit in a Diamond Quantum Processor*, *Nature (London)* **606**, 884 (2022).
- [24] F. Rozpedek, R. Yehia, K. Goodenough, M. Ruf, P. C. Humphreys, R. Hanson, S. Wehner, and D. Elkouss, *Near-Term Quantum-Repeater Experiments with Nitrogen-Vacancy Centers: Overcoming the Limitations of Direct Transmission*, *Phys. Rev. A* **99**, 052330 (2019).
- [25] C. E. Bradley, J. Randall, M. H. Abobeih, R. C. Berrevoets, M. J. Degen, M. A. Bakker, M. Markham, D. J. Twitchen, and T. H. Taminiau, *A Ten-Qubit Solid-State Spin Register with Quantum Memory up to One Minute*, *Phys. Rev. X* **9**, 031045 (2019).
- [26] H. Y. Carr and E. M. Purcell, *Effects of Diffusion on Free Precession in Nuclear Magnetic Resonance Experiments*, *Phys. Rev.* **94**, 630 (1954).
- [27] S. Meiboom and D. Gill, *Modified Spin-Echo Method for Measuring Nuclear Relaxation Times*, *Rev. Sci. Instrum.* **29**, 688 (1958).
- [28] G. de Lange, Z. H. Wang, D. Ristè, V. V. Dobrovitski, and R. Hanson, *Universal Dynamical Decoupling of a Single Solid-State Spin from a Spin Bath*, *Science* **330**, 60 (2010).
- [29] G. Terry, D. B. Baker, and M. S. Conradi, *New, Compensated Carr-Purcell Sequences Solid-State Spin from a Spin Bath*, *J. Magn. Reson.* **89**, 479 (1990).
- [30] G. S. Uhrig, *Exact Results on Dynamical Decoupling by π Pulses in Quantum Information Processes*, *New J. Phys.* **10**, 083024 (2008).
- [31] G. S. Uhrig, *Keeping a Quantum Bit Alive by Optimized π -Pulse Sequences*, *Phys. Rev. Lett.* **98**, 100504 (2007).
- [32] C. E. Bradley, *Order from Disorder: Control of Multi-Qubit Spin Registers in Diamond*, Ph.D. thesis, Delft University of Technology, 2021.
- [33] L. M. K. Vandersypen and I. L. Chuang, *NMR Techniques for Quantum Control and Computation*, *Rev. Mod. Phys.* **76**, 1037 (2005).
- [34] A. J. Freeman and R. B. Frankel, *Hyperfine Interactions* (Academic, New York, 1967).
- [35] W. Dong, F. A. Calderon-Vargas, and S. E. Economou, *Precise High-Fidelity Electron-Nuclear Spin Entangling Gates in NV Centers via Hybrid Dynamical Decoupling Sequences*, *New J. Phys.* **22**, 073059 (2020).
- [36] A. Bourassa, C. P. Anderson, K. C. Miao, M. Onizhuk, H. Ma, A. L. Crook, H. Abe, J. Ul-Hassan, T. Ohshima, N. T. Son, G. Galli, and D. D. Awschalom, *Entanglement and Control of Single Nuclear Spins in Isotopically Engineered Silicon Carbide*, *Nat. Mater.* **19**, 1319 (2020).
- [37] T. van der Sar, Z. H. Wang, M. S. Blok, T. H. T. H. Bernien, D. M. Toyli, D. A. Lidar, D. D. Awschalom, R. Hanson, and V. V. Dobrovitski, *Decoherence-Protected Quantum Gates for a Hybrid Solid-State Spin Register*, *Nature (London)* **484**, 82 (2012).
- [38] M. H. Abobeih, J. Cramer, M. A. Bakker, N. Kalb, M. Markham, D. J. Twitchen, and T. H. Taminiau, *One-Second Coherence for a Single Electron Spin Coupled to a Multi-qubit Nuclear-Spin Environment*, *Nat. Commun.* **9**, 2552 (2018).
- [39] Y. Makhlin, *Nonlocal Properties of Two-Qubit Gates and Mixed States, and the Optimization of Quantum Computations*, *Quantum Inf. Process.* **1**, 243 (2002).
- [40] P. Zanardi, C. Zalka, and L. Faoro, *Entangling Power of Quantum Evolutions*, *Phys. Rev. A* **62**, 030301(R) (2000).
- [41] S. Balakrishnan and R. Sankaranarayanan, *Entangling Power and Local Invariants of Two-Qubit Gates*, *Phys. Rev. A* **82**, 034301 (2010).
- [42] V. Coffman, J. Kundu, and W. K. Wootters, *Distributed Entanglement*, *Phys. Rev. A* **61**, 052306 (2000).
- [43] I. Bengtsson and K. Życzkowski, *Geometry of Quantum States: An Introduction to Quantum Entanglement* (Cambridge University Press, Cambridge, England, 2006).
- [44] T. Linowski, G. Rajchel-Mieldzioć, and K. Życzkowski, *Entangling Power of Multipartite Unitary Gates*, *J. Phys. A* **53**, 125303 (2020).
- [45] A. Jamiołkowski, *Linear Transformations which Preserve Trace and Positive Semidefiniteness of Operators*, *Rep. Math. Phys.* **3**, 275 (1972).
- [46] M.-D. Choi, *Completely Positive Linear Maps on Complex Matrices*, *Linear Algebra Appl.* **10**, 285 (1975).
- [47] F. Huber, O. Gühne, and J. Siewert, *Absolutely Maximally Entangled States of Seven Qubits Do Not Exist*, *Phys. Rev. Lett.* **118**, 200502 (2017).
- [48] D. Goyeneche, Z. Raissi, S. Di Martino, and K. Życzkowski, *Entanglement and Quantum Combinatorial Designs*, *Phys. Rev. A* **97**, 062326 (2018).
- [49] C. Hepp, T. Müller, V. Waselowski, J. N. Becker, B. Pingault, H. Sternschulte, D. Steinmüller-Nethl, A. Gali, J. R. Maze, M. Atatüre, and C. Becher, *Electronic Structure of the Silicon Vacancy Color Center in Diamond*, *Phys. Rev. Lett.* **112**, 036405 (2014).
- [50] A. E. Rugar, C. Dory, S. Aghaeimeibodi, H. Lu, S. Sun, S. D. Mishra, Z.-X. Shen, N. A. Melosh, and J. Vučković, *Narrow-Linewidth Tin-Vacancy Centers in a Diamond Waveguide*, *ACS Photonics* **7**, 2356 (2020).
- [51] A. E. Rugar, H. Lu, C. Dory, S. Sun, P. J. McQuade, Z.-X. Shen, N. A. Melosh, and J. Vučković, *Generation of Tin-Vacancy Centers in Diamond via Shallow Ion Implantation and Subsequent Diamond Overgrowth*, *Nano Lett.* **20**, 1614 (2020).
- [52] A. E. Rugar, S. Aghaeimeibodi, D. Riedel, C. Dory, H. Lu, P. J. McQuade, Z.-X. Shen, N. A. Melosh, and J. Vučković, *Quantum Photonic Interface for Tin-Vacancy Centers in Diamond*, *Phys. Rev. X* **11**, 031021 (2021).
- [53] J. R. Maze, A. Dréau, V. Waselowski, H. Duarte, J.-F. Roch, and V. Jacques, *Free Induction Decay of Single Spins in Diamond*, *New J. Phys.* **14**, 103041 (2012).
- [54] G.-Q. Liu, X.-Y. Pan, Z.-F. Jiang, N. Zhao, and R.-B. Liu, *Controllable Effects of Quantum Fluctuations on Spin Free-Induction Decay at Room Temperature*, *Sci. Rep.* **2**, 432 (2012).
- [55] K. Ghosh, H. Ma, M. Onizhuk, V. Gavini, and G. Galli, *Spin-Spin Interactions in Defects in Solids from Mixed All-Electron and Pseudopotential First-Principles Calculations*, *npj Comput. Mater.* **7**, 123 (2021).
- [56] P. Wang, B. Liu, and W. Yang, *Strongly Polarizing Weakly Coupled ^{13}C Nuclear Spins with Optically Pumped Nitrogen-Vacancy Center*, *Sci. Rep.* **5**, 15847 (2015).

- [57] A. Gali, M. Fyta, and E. Kaxiras, *Ab Initio Supercell Calculations on Nitrogen-Vacancy Center in Diamond: Electronic Structure and Hyperfine Tensors*, *Phys. Rev. B* **77**, 155206 (2008).
- [58] S. Felton, A. M. Edmonds, M. E. Newton, P. M. Martineau, D. Fisher, D. J. Twitchen, and J. M. Baker, *Hyperfine Interaction in the Ground State of the Negatively Charged Nitrogen Vacancy Center in Diamond*, *Phys. Rev. B* **79**, 075203 (2009).
- [59] J. M. Boss, K. Chang, J. Armijo, K. Cujia, T. Rosskopf, J. R. Maze, and C. L. Degen, *One- and Two-Dimensional Nuclear Magnetic Resonance Spectroscopy with a Diamond Quantum Sensor*, *Phys. Rev. Lett.* **116**, 197601 (2016).
- [60] B. Smeltzer, L. Childress, and A. Gali, ^{13}C *Hyperfine Interactions in the Nitrogen-Vacancy Centre in Diamond*, *New J. Phys.* **13**, 025021 (2011).
- [61] J. Zopes, K. S. Cujia, K. Sasaki, J. M. Boss, K. M. Itoh, and C. L. Degen, *Three-Dimensional Localization Spectroscopy of Individual Nuclear Spins with Sub-angstrom Resolution*, *Nat. Commun.* **9**, 4678 (2018).
- [62] R. Nagy, M. Niethammer, M. Widmann, Y.-C. Chen, P. Udvarhelyi, C. Bonato, J. U. Hassan, R. Karhu, I. G. Ivanov, N. T. Son, J. R. Maze, T. Ohshima, O. O. Soykal, A. Gali, S.-Y. Lee, F. Kaiser, and J. Wrachtrup, *High-Fidelity Spin and Optical Control of Single Silicon-Vacancy Centres in Silicon Carbide*, *Nat. Commun.* **10**, 1954 (2019).
- [63] M. A. Nielsen and I. L. Chuang, *Quantum Computation and Quantum Information*, 10th Anniversary edition (Cambridge University Press, Cambridge, England, 2010).
- [64] M. H. Abobeih, J. Randall, C. E. Bradley, H. P. Bartling, M. A. Bakker, M. J. Degen, M. Markham, D. J. Twitchen, and T. H. Taminiau, *Atomic-Scale Imaging of a 27-Nuclear-Spin Cluster Using a Quantum Sensor*, *Nature (London)* **576**, 411 (2019).
- [65] J. Cramer, *Quantum Error Correction with Spins in Diamond*, Ph.D. thesis, Delft University of Technology, 2016.
- [66] L. H. Pedersen, N. M. Møller, and K. Mølmer, *Fidelity of Quantum Operations*, *Phys. Lett. A* **367**, 47 (2007).
- [67] J. J. Gray, *Olinde Rodrigues' Paper of 1840 on Transformation Groups*, *Arch. Hist. Exact Sci.* **21**, 375 (1980).
- [68] S. G. Carter, O. O. Soykal, P. Dev, S. E. Economou, and E. R. Glaser, *Spin Coherence and Echo Modulation of the Silicon Vacancy in 4h – SiC at Room Temperature*, *Phys. Rev. B* **92**, 161202(R) (2015).